

1 MEASUREMENT OF ELECTROWEAK PRODUCTION OF  
2 SAME-SIGN W BOSON PAIRS WITH ATLAS (WORKING  
3 TITLE)

4 William Kennedy DiClemente

8                   Presented to the Faculties of The University of Pennsylvania  
9       in Partial Fulfillment of the Requirements for the Degree of Doctor of Philosophy  
10                   2019 Last compiled: February 3, 2019

11  
12 I. Joseph Kroll, Professor, Physics  
13 Supervisor of Dissertation

14  
15 Joshua Klein, Professor, Physics  
16 Graduate Group Chairperson

23 MEASUREMENT OF ELECTROWEAK PRODUCTION OF SAME-SIGN W BOSON PAIRS  
24 WITH ATLAS (WORKING TITLE)

25 COPYRIGHT  
26 2019  
27 William Kennedy DiClemente

28 All rights reserved.

---

## Acknowledgements

---

<sup>30</sup> I'd like to thanks the Ghosts of Penn Students Past for providing me with such an amazing thesis  
<sup>31</sup> template.

32

## ABSTRACT

33 MEASUREMENT OF ELECTROWEAK PRODUCTION OF SAME-SIGN W BOSON PAIRS  
34 WITH ATLAS (WORKING TITLE)

35

William Kennedy DiClemente

36

J. Kroll

37

This is the abstract text.

---

# Contents

---

39	<b>Acknowledgements</b>	iii
40	<b>Abstract</b>	iv
41	<b>Contents</b>	v
42	<b>List of Tables</b>	ix
43	<b>List of Figures</b>	xii
44	<b>Preface</b>	xviii
45	<b>Preface</b>	xviii
46	<b>1 Introduction</b>	1
47	<b>2 Theoretical Framework</b>	2
48	2.1 Introduction to the Standard Model . . . . .	2
49	2.2 Electroweak symmetry breaking and the Higgs boson . . . . .	4
50	2.3 Diboson physics . . . . .	7
51	<b>3 LHC and the ATLAS Detector</b>	9
52	3.1 The Large Hadron Collider . . . . .	9
53	3.2 The ATLAS Detector . . . . .	9
54	3.2.1 The Inner Detector . . . . .	9
55	3.2.1.1 Pixel Detector . . . . .	9

56	3.2.1.2	Semiconductor Tracker . . . . .	9
57	3.2.1.3	Transition Radiation Tracker . . . . .	9
58	3.2.2	The Calorimeters . . . . .	10
59	3.2.2.1	Liquid Argon Calorimeters . . . . .	10
60	3.2.2.2	Tile Calorimeters . . . . .	10
61	3.2.3	The Muon Spectrometer . . . . .	10
62	3.2.4	Particle reconstruction . . . . .	11
63	3.2.4.1	Track reconstruction . . . . .	11
64	3.2.4.2	Muon reconstruction . . . . .	11
65	3.2.4.3	Electron reconstruction . . . . .	11
66	3.2.4.4	Jet reconstruction . . . . .	11
67	<b>4 Alignment of the ATLAS Inner Detector</b>		<b>12</b>
68	4.1	The alignment method . . . . .	13
69	4.1.1	Alignment levels . . . . .	16
70	4.1.2	Alignment coordinate systems . . . . .	17
71	4.2	Early 2015 alignment of the ATLAS detector . . . . .	18
72	4.2.1	June alignment procedure . . . . .	20
73	4.2.2	Alignment results . . . . .	21
74	4.2.2.1	Residual distributions from collisions . . . . .	22
75	4.2.2.2	Track parameter resolution from cosmic rays . . . . .	24
76	4.2.3	Error scaling . . . . .	25
77	4.3	Level 2 alignment of the TRT . . . . .	28
78	4.4	Momentum bias from sagitta deformations . . . . .	29
79	4.4.1	Sagitta bias monitoring with electron $E/p$ . . . . .	31
80	4.4.1.1	Measuring $\langle E/p \rangle$ . . . . .	32
81	4.4.1.2	Results in 13 TeV data . . . . .	33
82	<b>5 Measurement of same-sign <math>WW</math> production at <math>\sqrt{s} = 13</math> TeV with ATLAS</b>		<b>37</b>
83	5.0.2	Theoretical overview of vector boson scattering . . . . .	37
84	5.0.3	Same-sign $W^\pm W^\pm$ scattering . . . . .	39
85	5.0.4	Overview of backgrounds . . . . .	41
86	5.1	Data and Monte Carlo samples . . . . .	43

87	5.1.1	Monte Carlo samples . . . . .	43
88	5.2	Object and event selection . . . . .	44
89	5.2.1	Object selection . . . . .	44
90	5.2.1.1	Muon candidate selection . . . . .	45
91	5.2.1.2	Electron candidate selection . . . . .	47
92	5.2.1.3	Jet candidate selection . . . . .	47
93	5.2.1.4	Treatment of overlapping objects . . . . .	47
94	5.2.2	Signal event selection . . . . .	49
95	5.3	Background estimations . . . . .	51
96	5.3.1	Estimation of the $WZ$ background . . . . .	51
97	5.3.2	Estimation of the $V\gamma$ background . . . . .	52
98	5.3.3	Estimation of backgrounds from charge misidentification . . . . .	54
99	5.3.3.1	Validation of the charge misidentification estimate . . . . .	57
100	5.3.4	Estimation of non-prompt backgrounds with the fake factor method . . . . .	57
101	5.3.4.1	Overview of the default fake factor method . . . . .	58
102	5.3.4.2	The fake factor with $p_T^{\text{cone}}$ . . . . .	59
103	5.3.4.3	Application of the fake factor . . . . .	61
104	5.3.4.4	Systematic uncertainties . . . . .	65
105	5.3.4.5	Results of the fake factor . . . . .	66
106	5.3.4.6	Validation of the fake factor . . . . .	69
107	5.3.5	Reduction of $WZ$ background using custom overlap removal . . . . .	70
108	5.4	Cross section measurement . . . . .	74
109	5.4.1	Maximum likelihood fit . . . . .	75
110	5.4.2	Definition of the fiducial volume . . . . .	76
111	5.4.3	Cross section extraction . . . . .	78
112	5.5	Summary of uncertainties . . . . .	79
113	5.5.1	Experimental uncertainties . . . . .	79
114	5.5.2	Theoretical uncertainties . . . . .	81
115	5.5.2.1	Uncertainties from EWK-QCD interference . . . . .	81
116	5.6	Results . . . . .	82
117	<b>6</b>	<b>Prospects for same-sign <math>WW</math> at the High Luminosity LHC</b>	<b>86</b>
118	6.0.1	Analysis Overview . . . . .	87

119	6.1	Theoretical motivation . . . . .	87
120	6.1.1	Experimental sensitivity to longitudinal polarization . . . . .	88
121	6.2	Monte Carlo samples . . . . .	89
122	6.3	Background estimations . . . . .	90
123	6.3.1	Truth-based isolation . . . . .	90
124	6.4	Object and event selection . . . . .	91
125	6.4.1	Object selection . . . . .	91
126	6.4.2	Event selection . . . . .	92
127	6.5	Selection optimization . . . . .	93
128	6.5.1	Random grid search algorithm . . . . .	93
129	6.5.2	Inputs to the optimization . . . . .	95
130	6.5.3	Results of the optimization . . . . .	96
131	6.6	Results . . . . .	97
132	6.6.1	Event yields . . . . .	97
133	6.6.2	Uncertainties . . . . .	100
134	6.6.3	Cross section measurement . . . . .	101
135	6.6.4	Longitudinal scattering significance . . . . .	101
136	<b>7</b>	<b>Conclusion</b>	<b>105</b>
137	<b>A</b>	<b>Additional material on <math>W^\pm W^\pm jj</math> prospects at the HL-LHC</b>	<b>106</b>
138	A.1	Truth isolation . . . . .	106
139	A.2	Plots of other optimization variables . . . . .	107
140	<b>B</b>	<b>Additional material on <math>W^\pm W^\pm jj</math> measurement at <math>\sqrt{s} = 13\text{TeV}</math></b>	<b>109</b>
141	B.1	Impact of experimental uncertainty on MC background estimations . . . . .	109
142	B.2	Additional signal region plots . . . . .	111
143	<b>Bibliography</b>		<b>112</b>

---

## List of Tables

---

145	4.1	The four alignment levels for each of the detector subsystems. The total number of alignable structures and degrees of freedom (DoF) to be aligned are given for each level.	18
147	4.2	Summary of the highest level of alignment applied to each ID subsystem when deriving the June alignment. . . . .	21
149	4.3	Estimated value of the error scaling term $b$ for each subdetector component with the June alignment. . . . .	28
151	5.1	Predicted cross sections for EQK and QCD production of diboson processes relevant to VBS at $\sqrt{s} = 8\text{TeV}$ using the <b>SHERPA</b> MC generator. Loose generator level cuts are applied on lepton $p_T > 5\text{ GeV}$ , dilepton invariant mass $m_{ll} > 4\text{ GeV}$ , and at least two jets with $m_{jj} > 10\text{ GeV}$ . . . . .	40
155	5.2	Summary of MC samples used in the analysis. . . . .	45
156	5.3	Muon selection criteria. All muons are required to pass the preselection (top), and then either the signal (middle) or loose (bottom) criteria is applied to the preselected electrons. . . . .	46
158	5.4	Electron selection criteria. All electrons are required to pass the preselection (top), and then either the signal (middle) or loose (bottom) criteria is applied to the preselected electrons. . . . .	48
161	5.5	Jet selection criteria. All jets are required to pass the above selection in order to be used in the analysis. . . . .	48
163	5.6	Summary of the overlap removal procedure used in the analysis. If the criteria in the “check” column is met, in the “result” column, the object on the left of the arrow is removed in favor of the object on the right. . . . .	49
166	5.7	Summary of trigger requirements for electrons and muons for $\sqrt{s} = 13\text{TeV}$ data collected in 2015 and 2016. At least one of the triggers must be satisfied. . . . .	50
168	5.8	The signal event selection. . . . .	51
169	5.9	Event yields in the $WZ$ control region before normalization. All lepton flavor channels are combined. . . . .	52
171	5.10	Selection criteria for the $V\gamma$ control region. . . . .	53
172	5.11	Event yields in the $V\gamma$ control region. The $V\gamma$ scale factor of 1.77 is calculated by scaling up the $Z\gamma$ and $Z+\text{jets}$ backgrounds to account for the difference between the data and predicted total background. . . . .	54
175	5.12	Selection criteria for the same-sign inclusive validation region. . . . .	57

---

176	5.13	Event selection for the dijet region used for calculating the fake factor. The selected lepton can pass either the nominal (signal) or loose selections. In the case of the nominal leptons, the $p_T > 27$ GeV requirement is replaced with $p_T > 15$ GeV. . . . .	63
177			
178	5.14	Values of the fake factor in each $p_T$ bin and for each individual systematic source. . . . .	68
179			
180	5.15	Estimated yields for the fake lepton background. The estimated yield is shown in the first column together with the statistical uncertainty followed by the systematic uncertainties from variations of the the fake factors within their statistical (stat.) and systematic (syst.) uncertainties. The labels $f_e$ and $f_\mu$ indicate the fake factors for electrons and muons, respectively. . . . .	69
181			
182	5.16	Selection criteria for the same-sign top fakes validation region. . . . .	69
183			
184	5.17	Custom OR definition. Leptons must pass this selection in order to be counted for the trilepton veto. . . . .	73
185			
186	5.18	Definition of the fiducial volume. . . . .	77
187			
188	5.19	Impact of various systematic effects on the fiducial cross section measurement. The impact of a given source of uncertainty is computed by performing the fit with the corresponding nuisance parameter varied up or down by one standard deviation from its nominal value. . . . .	79
189			
190	5.20	List of sources of experimental uncertainties on the reconstruction of physics objects. . . . .	80
191			
192	5.21	Impact of experimental uncertainties for the $W^\pm W^\pm jj$ EWK processes in all channels. . . . .	80
193			
194	5.22	Impact of experimental uncertainties for the $WZ$ process in all channels. . . . .	81
195			
196	5.23	The set of generator level cuts used for generating the interference samples with <code>MadGraph</code> . . . . .	82
197			
198	5.24	Cross sections for each different $W^\pm W^\pm jj$ production mode (inclusive, EWK only, QCD only, and interference only) generated using <code>MadGraph</code> . The cross sections are calculated using a minimal set of generator level cuts from events where the $W$ decays to a muon. . . . .	82
199			
200	5.25	Table of the data and prediction event yields in the signal region before the fit. Numbers are shown for the six lepton flavor and charge channels and for all channels combined. Here the $WZ$ background yields are normalized to the data in the $WZ$ control region. The background estimations from the fake factor are included in the “Non-prompt” category, and backgrounds from $V\gamma$ production and electron charge misidentification are combined in the “ $e/\gamma$ conversions” category. Finally, $ZZ$ , $VVV$ , and $t\bar{t}V$ backgrounds are combined in the “Other prompt” category. . . . .	83
201			
202			
203			
204			
205			
206			
207	5.26	Table of the data and prediction event yields in the signal region after the fit. Numbers are shown for the six lepton flavor and charge channels and for all channels combined. The background estimations from the fake factor are included in the “Non-prompt” category, and backgrounds from $V\gamma$ production and electron charge misidentification are combined in the “ $e/\gamma$ conversions” category. Finally, $ZZ$ , $VVV$ , and $t\bar{t}V$ backgrounds are combined in the “Other prompt” category. . . . .	83
208			
209			
210			
211			
212			
213	6.1	Summary of MC samples used in the analysis. . . . .	90
214	6.2	Truth-based isolation requirements for electrons and muons. . . . .	91
215	6.3	Summary of the signal event selection. . . . .	93
216	6.4	Updates to the $W^\pm W^\pm jj$ event selection criteria after optimization. Cuts not listed remain unchanged from the default selection in Table 6.3. . . . .	96
217			
218	6.5	Signal and background event yields using the default event selection for an integrated luminosity of $\mathcal{L} = 3000 \text{ fb}^{-1}$ . Events containing a fake or charge-flipped electron are removed from their respective sources and combined into a single entry each. . . . .	98
219			
220			
221	6.6	Signal and background event yields using the optimized event selection for an integrated luminosity of $\mathcal{L} = 3000 \text{ fb}^{-1}$ . Events containing a fake or charge-flipped electron are removed from their respective sources and combined into a single entry each. . . . .	99
222			
223			

224	6.7 Summary of estimated experimental and rate uncertainties. . . . .	100
225	A.1 Event yields prior to applying any form of truth-based isolation criteria. . . . .	106
226	A.2 Event yields after applying a test version of the truth-based isolation. . . . .	107
227	B.1 Impact of experimental uncertainties for the $W^\pm W^\pm jj$ QCD processes in all channels. .	109
228	B.2 Impact of experimental uncertainties for triboson process in all channels. . . . .	110
229	B.3 Impact of experimental uncertainties for $t\bar{t}V$ processes in all channels. . . . .	110
230	B.4 Impact of experimental uncertainties for the $W\gamma$ process in all channels. . . . .	110
231	B.5 Impact of experimental uncertainties for the $Z\gamma$ process in all channels. . . . .	110
232	B.6 Impact of experimental uncertainties for the $ZZ$ process in all channels. . . . .	111

---

## List of Figures

---

234    2.1	An illustration of the potential term $V(\phi)$ in the cases where $\mu^2 > 0$ (left) and $\mu^2 < 0$ (right). The right-hand plot shows the Higgs potential, or ‘‘Mexican hat potential’’, with the minimum at $ \phi  = \sqrt{-\frac{\mu^2}{\lambda}}$ rather than at $ \phi  = 0$ as in the left-hand plot. . . . .	5
237    2.2	Vector boson fusion involving triple gauge couplings (left) and vector boson scattering involving a quartic gauge coupling (right). . . . .	7
239    2.3	Diboson diagrams involving the $s$ -channel (left) and $t$ -channel (right) exchanges of a Higgs boson. . . . .	8
241    3.1	General cut-away view of the ATLAS detector. . . . .	10
242    4.1	Graphical representation of the effect of a misaligned detector element. The reconstructed particle track (dashed arrow) differs from the actual trajectory of the particle (solid arrow) due to the shift in one of the detector elements. The cyan lines represent the track-to-hit residuals. . . . .	13
246    4.2	Graphical representation of the ID alignment chain. . . . .	16
247    4.3	A schematic representation of the Inner Detector in the longitudinal plane with the global coordinate system overlaid on top. The Pixel detector and IBL are shown in blue, the SCT in green, and the TRT in red. The local coordinates for each subdetector module are inset on the right. . . . .	19
251    4.4	The $d_0$ distributions with respect to the reconstructed primary vertex using the $\sqrt{s} = 13\text{TeV}$ collision data sample reconstructed using the June (black) and March (green) alignments. The data is compared to a MC simulation using a perfect detector geometry (red). The distributions are normalized to the same number of entries. . . . .	22
255    4.5	Local $x$ (left) and local $y$ (right) residual distributions of the IBL planar sensors using the $\sqrt{s} = 13\text{TeV}$ collision data sample reconstructed using the June (black) and March (green) alignments. The data is compared to a MC simulation using a perfect detector geometry (red). The distributions are normalized to the same number of entries. . . . .	23
259    4.6	The mean of the local $x$ (left) and local $y$ (right) residual distributions as a function of the global $z$ position of each IBL module using the $\sqrt{s} = 13\text{TeV}$ collision data sample reconstructed using the June (black) and March (green) alignments. The data is compared to a MC simulation using a perfect detector geometry (red). . . . .	24

263	4.7	Local $x$ (top) and local $y$ (bottom) residual distributions for the Pixel barrel (excluding the IBL, left) and end-caps (right) using the $\sqrt{s} = 13\text{TeV}$ collision data sample reconstructed using the June (black) and March (green) alignments. The data is compared to a MC simulation using a perfect detector geometry (red). The distributions are normalized to the same number of entries. . . . .	25
268	4.8	Local $x$ residual distributions for the SCT barrel (left) and end-caps (right) using the $\sqrt{s} = 13\text{TeV}$ collision data sample reconstructed using the June (black) and March (green) alignments. The data is compared to a MC simulation using a perfect detector geometry (red). The distributions are normalized to the same number of entries. . . . .	26
272	4.9	Residual distributions for the TRT barrel (left) and end-caps (right) using the $\sqrt{s} = 13\text{TeV}$ collision data sample reconstructed using the June (black) and March (green) alignments. The data is compared to a MC simulation using a perfect detector geometry (red). The distributions are normalized to the same number of entries. . . . .	26
276	4.10	Representation of splitting a single cosmic ray track passing through the entire detector (left) into two separate tracks (right). . . . .	27
278	4.11	Distribution of the difference in the impact parameter $\Delta d_0$ (left) and charge over transverse momentum $\Delta q/p_T$ (right) between the two cosmic ray split tracks. The June (black) and March (green) alignments are compared. The distributions are normalized to the same number of entries. . . . .	27
282	4.12	Pull distributions in local $x$ (left) and $y$ (right) for the IBL using the $\sqrt{s} = 13\text{TeV}$ collision data sample after applying the error scaling. . . . .	28
284	4.13	Residual means by straw layer in two TRT $\phi$ -sectors affected by a tilt misalignment. The tilts in each of the three modules are clearly visible in the red points representing the reconstructed data prior to alignment. After four iterations of L2 alignment, the residual means in the gray points are flat. . . . .	29
288	4.14	Two dimensional map of residuals in the first layer of the TRT barrel vs $z$ and $\phi$ . Each bin represents the mean of a Gaussian fit to the TRT residuals in that bin. The map on the left is after the L3 (wire-by-wire) alignment of the TRT performed in 2010, and the map on the right is after the L2 alignment at the end of 2015. The $z$ -axis for both plots use the same scale. . . . .	30
293	4.15	Representation of a curl distortion in the detector. The image shows a cutaway in the transverse plane. The deformation is represented by the red arrows, and the impact on the reconstructed positive (blue) and negative (green) tracks are shown. The dashed lines represent the true particle trajectories, and the solid lines represent the reconstructed trajectories. . . . .	31
298	4.16	Geometric definition of the sagitta $s$ in relation to the length of the chord $l$ and the radius $r$ of a circular arc. . . . .	31
300	4.17	$E/p$ distributions of electrons and positrons in two different $\eta$ - $\phi$ bins of the detector. The left hand plot is taken from a region with no momentum bias where $\langle E/p \rangle^+ = \langle E/p \rangle^-$ , while the right hand plot shows an 8% disagreement in $\langle E/p \rangle$ between electrons and positrons. . . . .	33
304	4.18	Sagitta bias in the $\sqrt{s} = 13\text{TeV}$ data collected by ATLAS in 2016 as a function of $\eta$ and $\phi$ for the prompt (left) and reprocessed (right) alignments using the $E/p$ method. . . . .	34
306	4.19	Sagitta bias in the $\sqrt{s} = 13\text{TeV}$ data collected by ATLAS in 2016 projected along $\eta$ for the prompt (gray) and reprocessed (blue) alignments using the $E/p$ method. . . . .	35
308	4.20	Sagitta bias in the $\sqrt{s} = 13\text{TeV}$ data collected by ATLAS in 2017 as a function of $\eta$ and $\phi$ in reconstructed electrons (left) and after two iterations of momentum corrections (right) from the $E/p$ method. . . . .	35

311	4.21 Sagitta bias in the $\sqrt{s} = 13\text{TeV}$ data collected by ATLAS in 2017 projected along $\eta$ in reconstructed electrons (gray) and after one (red) and two (blue) iterations of momentum corrections from the $E/p$ method. . . . .	36
314	5.1 Cross sections in nanobarns for five different scattering processes of longitudinally polarized vector bosons as a function of center of mass energy $\sqrt{s}$ . Without a SM Higgs boson (left), the cross sections grow unbounded with $\sqrt{s}$ ; however with a 120 GeV Higgs boson (right), the cross sections no longer diverge. . . . .	38
318	5.2 Tree-level Feynman diagrams for VBS EWK $VVjj$ production including triple gauge couplings involving $W$ and/or $Z$ bosons (top left and top middle), quartic gauge coupling (top right), or the exchange of a Higgs boson ( $s$ -channel bottom left and $t$ -channel bottom right). The labels are quarks ( $q$ ), fermions ( $f$ ), and gauge bosons ( $V = W, Z$ ). . . . .	39
322	5.3 Tree-level Feynman diagrams for non-VBS EWK $VVjj$ production. The labels are quarks ( $q$ ), fermions ( $f$ ), and gauge bosons ( $V = W, Z$ ). . . . .	39
324	5.4 Tree-level Feynman diagrams for QCD $VVjj$ production. The labels are quarks ( $q$ ), fermions ( $f$ ), and gauge bosons ( $V = W, Z$ ). . . . .	40
326	5.5 Feynman diagrams for VBS EWK production of $W^\pm W^\pm jj$ events. The leftmost diagram contains a quartic gauge coupling vertex, and the rightmost diagram contains an exchange of a Higgs boson. . . . .	41
329	5.6 $W^\pm W^\pm jj$ VBS event topology containing two leptons (1 and 2) with the same electric charge, two neutrinos, and two forward tagging jets (3 and 4) with large rapidity separation $\Delta y$ . . . . .	41
332	5.7 Generator level comparisons at $\sqrt{s} = 8\text{TeV}$ of dijet invariant mass ( $m_{jj}$ , left) and dijet rapidity ( $\Delta y_{jj}$ , right) in EWK (red) and QCD (blue) $W^\pm W^\pm jj$ events. Both data sets have been normalized to the same area. . . . .	42
335	5.8 ATLAS event display of a $pp \rightarrow W^+W^+ \rightarrow \mu^+\nu_\mu\mu^+\nu_\mu jj$ event. The muons are represented by the red lines travelling from the ID through the MS, and the forward jets are represented by the blue cones with yellow energy deposits in the calorimeters. The direction of the $E_T^{\text{miss}}$ in the transverse plane is indicated by the gray dashed line in the inset image. . . . .	42
340	5.9 Leading lepton $p_T$ (left) and $\eta$ (right) distributions in the $WZ$ control region before normalization. All lepton channels are combined. . . . .	53
342	5.10 Trilepton invariant mass $m_{lll}$ distribution in the $WZ$ control region before normalization. All lepton channels are combined. . . . .	53
344	5.11 Charge misidentification rates for electrons as a function of $ \eta $ and $p_T$ . Rates are calculated from $Z \rightarrow e^+e^-$ MC after applying scale factors to approximate the charge mis-ID rates in data. . . . .	55
347	5.12 Dilepton invariant mass distribution $m_{ll}$ for the $ee$ channel in the same-sign inclusive VR. . . . .	57
348	5.13 $p_T$ distributions for the leading (left) and subleading (right) electron for the $ee$ channel in the same-sign inclusive VR. In these plots, the cut requiring $m_{ee}$ to fall within the $Z$ mass window has been inverted in order to test the modelling away from the $Z$ peak. . . . .	58
351	5.14 $\Delta p_T$ distributions for nominal (blue) and loose (red) muons in simulated $t\bar{t}$ events. Each muon has been matched to a truth-level jet. Both distributions are normalized to unit area. . . . .	60
354	5.15 $\Delta p_T$ distributions for muons (top) and electrons (bottom) in simulated $t\bar{t}$ events. Each lepton has been matched to a truth-level jet, and that truth jet has had its $p_T$ corrected to include all truth muons within a cone of $\Delta R < 0.4$ . The nominal leptons are in black. $\Delta p_T$ is calculated for the loose leptons using $p_T$ (red) and $p_T + p_T^{\text{cone}}$ (blue). . . . .	62
358	5.16 Distributions of $p_T^{\text{cone}}/p_T$ for nominal (black) and loose (red) muons in simulated $t\bar{t}$ events. . . . .	63

359	5.17	The measured fake factor as a function of muon $p_T + p_T^{\text{cone}}$ . The error bars represent the statistical uncertainty only. . . . .	64
360			
361	5.18	The measured fake factor as a function of electron $p_T + p_T^{\text{cone}}$ in the central ( $ \eta  < 1.37$ , blue) and forward ( $ \eta  > 1.37$ , red) regions of the detector. The error bars represent the statistical uncertainty only. . . . .	64
362			
363			
364	5.19	Graphical representation of the fake factor application using $p_T + p_T^{\text{cone}}$ . The value of $p_T + p_T^{\text{cone}}$ for the loose lepton is used to “look up” the fake factor weight which is then applied to the event. The loose lepton’s $p_T$ becomes $p_T + p_T^{\text{cone}}$ for the purpose of the fake background estimation. . . . .	65
365			
366			
367			
368	5.20	Systematic variations in the fake factor as a function of muon $p_T + p_T^{\text{cone}}$ . The individual fake factors obtained for each systematic variation are displayed with their statistical uncertainties. . . . .	66
369			
370			
371	5.21	Systematic variations in the fake factor as a function of electron $p_T + p_T^{\text{cone}}$ in the central ( $ \eta  < 1.37$ , top) and forward ( $ \eta  > 1.37$ , bottom) regions of the detector. The individual fake factors obtained for each systematic variation are displayed with their statistical uncertainties. . . . .	67
372			
373			
374			
375	5.22	Distributions of the subleading lepton $p_T$ in the same-sign top fakes VR for $\mu^\pm\mu^\pm$ events (top right), $e^\pm e^\pm$ events (top left), $\mu^\pm e^\pm$ events (bottom left), and all events combined (bottom right). All errors are statistical only. . . . .	70
376			
377			
378	5.23	Pseudorapidity ( $\eta$ ) distributions of truth muons (top) and electrons (bottom) for Sherpa $W^\pm W^\pm jj$ and $WZ$ MC samples. The blue vertical lines represent the allowed $\eta$ range for each lepton flavor. The numbers correspond to the number of raw MC events that fall within and outside of the allowed $\eta$ range for each MC sample. . . . .	71
379			
380			
381			
382	5.24	Distributions of $p_{T,\text{ratio}}(\mu, j)$ for EWK and QCD $W^\pm W^\pm jj$ signal (black) and $WZ$ background (teal) for truth-matched third muons in events that pass the trilepton veto. Both distributions are normalized to unit area. The associated efficiency curves are on the right where efficiency is defined as the percentage of total events that would pass a cut on $p_{T,\text{ratio}}(\mu, j)$ at a given value on the $x$ -axis. . . . .	72
383			
384			
385			
386			
387	5.25	Distributions of $\Delta R(\mu, j)$ for EWK and QCD $W^\pm W^\pm jj$ signal (black) and $WZ$ background (teal) for truth-matched third muons in events that pass the trilepton veto. Both distributions are normalized to unit area. The associated efficiency curves are on the right where efficiency is defined as the percentage of total events that would pass a cut on $\Delta R(\mu, j)$ at a given value on the $x$ -axis. . . . .	72
388			
389			
390			
391			
392	5.26	Distributions of $p_{T,\text{ratio}}(e, j)$ for EWK and QCD $W^\pm W^\pm jj$ signal (black) and $WZ$ background (teal) for truth-matched third electrons in events that pass the trilepton veto. Both distributions are normalized to unit area. The associated efficiency curves are on the right where efficiency is defined as the percentage of total events that would pass a cut on $p_{T,\text{ratio}}(e, j)$ at a given value on the $x$ -axis. . . . .	73
393			
394			
395			
396			
397	5.27	Two-dimensional plots of $p_{T,\text{ratio}}(\mu, j)$ vs $\Delta R(\mu, j)$ for truth-matched third muons in events that pass the trilepton veto for EWK and QCD $W^\pm W^\pm jj$ signal (left) and $WZ$ background (right). The blue overlay indicates the area in which the third leptons will pass the custom OR and result in the event failing the trilepton veto. . . . .	74
398			
399			
400			
401	5.28	Visual representation of the different kinematic regions relevant to the cross section measurement. The acceptance factor $\mathcal{A}$ converts from the truth level total phase space to the truth level fiducial region, and the efficiency correction $\mathcal{C}$ translates the fiducial region in to the reconstruction level signal region. . . . .	77
402			
403			
404			

405	5.29	The dijet invariant mass $m_{jj}$ distributions for data and predicted signal and background in the signal region after the fit. The shaded band represents the statistical and systematic uncertainties added in quadrature. Note that the bins have been scaled such that they represent the number of events per 100 GeV in $m_{jj}$ . The background estimations from the fake factor are included in the “Non-prompt” category, and backgrounds from $V\gamma$ production and electron charge misidentification are combined in the “ $e/\gamma$ conversions” category. Finally, $ZZ$ , $VVV$ , and $t\bar{t}V$ backgrounds are combined in the “Other prompt” category. . . . .	84
413	5.30	The event yields for data and predicted signal and background in the $WZ$ and low- $m_{jj}$ control regions after the fit. The shaded band represents the statistical and systematic uncertainties added in quadrature. The background estimations from the fake factor are included in the “Non-prompt” category, and backgrounds from $V\gamma$ production and electron charge misidentification are combined in the “ $e/\gamma$ conversions” category. Finally, $ZZ$ , $VVV$ , and $t\bar{t}V$ backgrounds are combined in the “Other prompt” category. . . . .	84
419	5.31	Comparison of the measured $W^\pm W^\pm jj$ EWK fiducial cross section with theoretical calculations from <b>SHERPA v2.2.2</b> and <b>POWHEG-BOX v2</b> . The light orange band represents the total experimental uncertainty on the measured value, and the dark orange hashed band is the statistical uncertainty. For the simulations, the light blue band represents the total theoretical uncertainty, and the dark blue hashed band are the scale uncertainties. The theory predictions do not include the interference between the EWK and QCD production. . . . .	85
426	6.1	Comparison of the leading (left) and subleading (right) lepton $p_T$ distributions for purely longitudinal (LL, black) and mixed polarization (LT+TT, cyan) $W^\pm W^\pm jj$ events. . . . .	88
428	6.2	Comparison of the azimuthal dijet separation ( $ \Delta\phi_{jj} $ ) for purely longitudinal (LL, black) and mixed polarization (LT+TT, cyan) $W^\pm W^\pm jj$ events. . . . .	89
430	6.3	A visual representation of a two-dimensional rectangular grid (left) and a random grid (right) in variables $x$ and $y$ . The signal events are the black circles, and the red squares are the background events. Each intersection of gray dashed lines represents a cut point to be evaluated by the optimization. . . . .	94
434	6.4	Leading (top) and subleading (bottom) jet $p_T$ distributions. The default and optimized cuts are represented by the red and green dashed lines, respectively. The $W^\pm W^\pm jj$ EWK signal (black points) is normalized to the same area as the sum of the backgrounds (colored histogram). . . . .	97
438	6.5	Lepton-jet centrality distribution. The default and optimized cuts are represented by the red and green dashed lines, respectively. The $W^\pm W^\pm jj$ EWK signal (black points) is normalized to the same area as the sum of the backgrounds (colored histogram). . . . .	98
441	6.6	$p_T$ distributions for the leading jet using the default (left) and optimized (right) event selections for all channels combined. . . . .	99
443	6.7	$p_T$ distributions for the subleading jet using the default (left) and optimized (right) event selections for all channels combined. . . . .	99
445	6.8	$p_T$ distributions for lepton-jet centrality $\zeta$ using the default (left) and optimized (right) event selections for all channels combined. . . . .	100
447	6.9	Projections of the statistical (black), theoretical (blue), systematic (yellow), and total (red) uncertainties on the measured cross section as a function of integrated luminosity using the optimized event selection. . . . .	102
450	6.10	Dijet azimuthal separation ( $ \Delta\phi_{jj} $ ) for the low $m_{jj}$ region ( $520 < m_{jj} < 1100$ GeV, top) and the high $m_{jj}$ region ( $m_{jj} > 1100$ GeV, bottom). The purely longitudinal (LL, gray) is plotted separately from the mixed and transverse (LT+TT, cyan) polarizations. . . . .	103

453	6.11 Projections of the expected longitudinal scattering significance as a function of integrated luminosity when considering all sources of uncertainties (black) or only statistical uncertainties (red). . . . .	104
456	A.1 Leading lepton $p_T$ distribution. The default and optimized cuts are represented by the red and green dashed lines, respectively. The $W^\pm W^\pm jj$ EWK signal (black points) is normalized to the same area as the sum of the backgrounds (colored histogram). . . . .	107
459	A.2 Dilepton invariant mass distribution. The default and optimized cuts are represented by the red and green dashed lines, respectively. The $W^\pm W^\pm jj$ EWK signal (black points) is normalized to the same area as the sum of the backgrounds (colored histogram). . . . .	108
462	A.3 Dijet invariant mass distribution. The default and optimized cuts are represented by the red and green dashed lines, respectively. The $W^\pm W^\pm jj$ EWK signal (black points) is normalized to the same area as the sum of the backgrounds (colored histogram). . . . .	108
464		

---

## Preface

---

466 This thesis presents the major highlights of my work with the ATLAS experiment as a graduate  
467 student at the University of Pennsylvania from Fall of 2013 until early Spring of 2019.

468 The first step of working on the experiment is to complete a *qualification task* in order to be  
469 included on the author list of ATLAS publications. These tasks are an opportunity to contribute  
470 to the experiment as a whole, such as maintaining detector hardware or monitoring physics perfor-  
471 mance. For my qualification task, I worked with the Inner Detector Alignment group which works  
472 to make sure we have accurate knowledge of the locations of each and every sensor in the detector.  
473 My qualification task involved investigating a possible momentum bias in the Monte Carlo (MC)  
474 simulated data. The MC is supposed to be reconstructed with a perfect detector geometry which  
475 should in principle be free of any momentum biases. Ultimately I determined that the size of the  
476 biases were small enough to be negligible compared to what is seen in the real data, and that they  
477 could be corrected for if necessary.

478 My work with the alignment group would continue for the duration of my time here at Penn. In  
479 early 2015, at the start of the LHC’s second data-taking run (Run 2), I worked assisted in validating  
480 the first set of alignment constants using  $\sqrt{s} = 8$  TeV proton-proton collision data. At this point  
481 I took over the responsibility of alignment of the TRT subdetector. The TRT was aligned to high  
482 accuracy in Run 1, and over the course of my time working on alignment, the TRT never required  
483 a straw-by-straw alignment; however it did require a module-level alignment at the end of 2015.  
484 My final responsibility in the alignment group was monitoring momentum biases using the energy-  
485 momentum ratio ( $E/p$ ) of electrons. For the large data reprocessing, the  $E/p$  method served as a  
486 cross check to a similar method using  $Z$  boson events for monitoring and aligning out momentum  
487 biases in the detector. The results from both methods were also used in the uncertainties for the  
488 tracking measurements.

489 On the analysis side, I had previous experience in Standard Model (SM) electroweak physics  
490 from my time as an undergraduate at Duke University, and it remained a point of interest for  
491 me in graduate school. As such, I was happy to work with fellow Penn students on the cross  
492 section measurement of SM  $WZ$  diboson production with the early  $\sqrt{s} = 13$  TeV ATLAS data.  
493 My contribution to the analysis was primarily on the software side, as I maintained and updated  
494 the analysis framework. While the  $WZ$  measurement is not covered by this thesis, it provided me  
495 with invaluable analysis experience in electroweak physics, as well as a detailed understanding of a  
496 major background to many diboson processes. The results for this analysis can be found published  
497 in Physics Letters B in 2016 [1].

498 The final two analyses I worked on involve the scattering of same-sign  $W$  bosons, and they make  
499 up the majority of this thesis. The first analysis is a measurement of the  $W^\pm W^\pm jj$  cross section  
500 at  $\sqrt{s} = 13$  TeV. This measurement along with that of the CMS collaboration represent the first  
501 observation of the  $W^\pm W^\pm jj$  scattering process. My primary contribution to the analysis is in the  
502 estimation of the fake lepton background, where we implemented a brand new version of the fake  
503 factor method using particle isolation variables. I also did a preliminary study of the interference  
504 between electroweak and strong production of  $W^\pm W^\pm jj$  events, assisted in the production of private  
505 data samples for use with the analysis framework, and used my familiarity with the  $WZ$  process  
506 to optimize the rejection of the background. Ultimately the majority of the  $WZ$  rejection was not  
507 included in the final result; however, it is still covered in the thesis in the hopes that it will be useful  
508 for similar analyses in the future. The formal publication for this measurement will likely be coming  
509 out within the next few months.

510 The second  $W^\pm W^\pm jj$  analysis is a study on the prospects for a measurement of the process at the  
511 upgraded High-Luminosity LHC, scheduled to begin operation in 2026. Here my main contribution  
512 was an optimization of the event selection using a Random Grid Search algorithm. Through the  
513 optimization we expect to take advantage of the higher center of mass energy and greater volume of  
514 data and tighten certain selection cuts to increase the strength of the  $W^\pm W^\pm jj$  signal. In addition, I  
515 once again maintained and updated the analysis framework and produced the group's data samples,  
516 and I also developed a truth-based particle isolation criteria in order to reduce contributions from  
517 backgrounds involving the top quark. The results of this prospects study will be published as a part  
518 of the annual Yellow Report for the High-Luminosity LHC.

Will K. DiClemente  
Philadelphia, February 2019

520

## CHAPTER 1

---

521

# Introduction

---

522 The Standard Model (SM)<sup>1</sup> has been remarkably successful...

---

<sup>1</sup>Here's a footnote.

## CHAPTER 2

---

# Theoretical Framework

---

525 This chapter outlines the theoretical groundwork for the rest of the thesis. An overview of the Stan-  
 526 dard Model of particle physics (SM) is given in Section 2.1, followed by the electroweak symmetry  
 527 breaking mechanism involving the Higgs boson in Section 2.2. Finally, Section 2.3 will go into some  
 528 detail on the interests of diboson physics specifically.

529 **2.1 Introduction to the Standard Model**

530 The Standard Model of particle physics serves as a mathematical description of the fundamental  
 531 particles of the universe and their interactions. It has been developed over the course of the past  
 532 century, incorporating both predictions from theory and results from experiments. All in all, the SM  
 533 has proven remarkably successful in accurately describing particle interactions seen in experiments.

534 The SM is a quantum field theory (QFT) [2, 3] in which the fundamental particles are represented  
 535 as excited states of their corresponding fields. The spin- $\frac{1}{2}$  fermionic fields give rise to the quarks  
 536 and leptons comprising ordinary matter, the spin-1 fields correspond to the electroweak bosons and  
 537 the gluon which mediate the electroweak and strong forces, respectively, and finally the scalar Higgs  
 538 field is responsible for electroweak symmetry breaking. The excitations and interactions of the fields  
 539 are governed by the SM Lagrangian, which is invariant under local transformations of the group  
 540  $SU(3) \times SU(2) \times U(1)$ . **TODO: need more detail/refinement here**

541 The first quantum field theory to be developed is quantum electrodynamics (QED) [4], which  
 542 describes the electromagnetic interaction. The theory predicts the existence of a  $U(1)$  gauge field  
 543 that interacts with the electrically charged fermions. This field corresponds to the photon. A key  
 544 aspect of QED is that it is perturbative. The coupling constant  $\alpha = e^2/4\pi$  is small, where  $e$  is

545 electrical charge of the field, allowing for the use of perturbation theory in calculations. In this case,  
 546 calculations can be written as a power series in  $\alpha$ , where successive higher order terms contribute  
 547 less to the final result. **TODO: renormalizability here?**

548 The strong interaction—the theory of quarks and gluons—has also been described using QFT  
 549 as quantum chromodynamics (QCD). The symmetry group for QCD is  $SU(3)$ , and its eight gen-  
 550 erators correspond to the eight differently charged, massless gluons [5]. Unlike in QED, which has  
 551 positive and negative charges, the strong force has three “colors”. Color charge combined with the  
 552 non-Abelian nature of  $SU(3)$ , which allows the gluons to interact with each other, result in the  
 553 most well-known property of QCD: color confinement. In order to increase the separation between  
 554 two color-charged quarks, the amount of energy required increases until it becomes energetically  
 555 favorable to pair-produce a new quark-antiquark pair, which then bind to the original quarks. The  
 556 end result of this is that only color-neutral objects exist in isolation. What this means for the strong  
 557 coupling constant  $\alpha_s$  is that its value at the low energies where confinement occurs is large, on  
 558 the order of  $\alpha_s \sim 1$ . The consequence of this is that perturbation theory cannot be used to accu-  
 559 rately approximate interactions. While this appears at first to be a critical problem for predictions,  
 560 fortunately it turns out that  $\alpha_s$  “runs”, or decreases in magnitude at higher energy [6, 7]. This so-  
 561 called “asymptotic freedom” allows QCD to be calculated perturbatively [8] at energies accessible  
 562 by collider experiments including the LHC.

563 The last gauge field corresponds to the weak interaction. Ultimately, the weak  $SU(2)$  and the  
 564 electromagnetic  $U(1)$  mix to form the  $SU(2) \times U(1)$  *electroweak* (EWK) interaction [9, 10]. A  
 565 more detailed description of the mixing will be discussed in conjunction with electroweak symmetry  
 566 breaking (EWSB) in Section 2.2; however, a summary of the resulting EWK interaction is presented  
 567 here, at the risk of some repeated information to follow. There are three weak isospin bosons arising  
 568 from the  $SU(2)$  group ( $W_\mu^1$ ,  $W_\mu^2$ , and  $W_\mu^3$ ) and one weak hypercharge boson from the  $U(1)$  group  
 569 ( $B_\mu$ ). The  $W_3$  and  $B$  bosons mix according to the weak mixing angle  $\theta_W$  to form the  $Z$  boson and  
 570 the photon according to:

$$\begin{pmatrix} \gamma \\ Z \end{pmatrix} = \begin{pmatrix} \cos \theta_W & \sin \theta_W \\ -\sin \theta_W & \cos \theta_W \end{pmatrix} \begin{pmatrix} B_\mu \\ W_\mu^3 \end{pmatrix} \quad (2.1)$$

571 The value of  $\theta_W$  is not predicted by the SM; it is one example of an experimental input to the  
 572 theory, measured to be  $\sin^2 \theta_W = 0.23153 \pm 0.00016$  [11]. The charged  $W^\pm$  bosons are a mixture of  
 573 the remaining  $W_\mu^1$  and  $W_\mu^2$  bosons:

$$W^\pm = \frac{1}{\sqrt{2}}(W_\mu^1 \mp iW_\mu^2) \quad (2.2)$$

574 Unlike the photon (and the gluon of QCD), the  $W^\pm$  and  $Z$  bosons are massive. This means that  
 575 even though SU(2) is non-Abelian, the range of interaction is short and confinement does not occur.  
 576 Lastly, the EWK interaction is chiral, only coupling to the left-handed component of the fermion  
 577 fields

578 One final field remains within the SM: the scalar Higgs field. It was originally proposed in the  
 579 1960's to explain the masses of the  $W^\pm$  and  $Z$  bosons [12, 13, 14] and is the mechanism for the  
 580 EWSB process. The particle associated with the field is a massive scalar boson, which was at last  
 581 discovered by ATLAS and CMS in 2012 [15, 16] with a mass of 125 GeV.

## 582 2.2 Electroweak symmetry breaking and the Higgs boson

583 The results of electroweak mixing and the implications of the Higgs field have been introduced  
 584 in the previous section. If the EWK theory were an unbroken symmetry, the associated  $W^\pm$  and  
 585  $Z$  bosons would be massless; however, when observed experimentally, they were found to be quite  
 586 heavy [17, 18], at around 80 GeV and 91 GeV, respectively [19]. Here, a more detailed explanation  
 587 of the Higgs mechanism and how it “spontaneously breaks” the EWK symmetry, resulting in the  
 588 three massive bosons ( $W^\pm$  and  $Z$ ) and one massless boson (photon), is presented.

589 To see how the Higgs mechanism results in the massive vector bosons and a massless photon,  
 590 consider the following. Beginning with a complex scalar doublet  $\phi$  defined as:

$$\phi = \begin{pmatrix} \phi^+ \\ \phi^0 \end{pmatrix} = \sqrt{\frac{1}{2}} \begin{pmatrix} \phi_1 + i\phi_2 \\ \phi_3 + i\phi_4 \end{pmatrix} \quad (2.3)$$

591 a Lagrangian  $\mathcal{L}$  can be written:

$$\mathcal{L} = (\mathcal{D}_\mu \phi)^\dagger (\mathcal{D}^\mu \phi) - \mu^2 \phi^\dagger \phi - \lambda(\phi^\dagger \phi)^2 \quad (2.4)$$

592 where  $\lambda > 0$  and  $\mathcal{D}_\mu$  is the covariant derivative.  $\mathcal{D}_\mu$  is defined such that  $\mathcal{L}$  is invariant under a local  
 593 SU(2)  $\times$  U(1) gauge transformation:

$$\mathcal{D}_\mu \phi = \left( \partial_\mu + \frac{ig}{2} \tau_a W_\mu^a + \frac{ig'}{2} B_\mu \right) \phi \quad (2.5)$$

594 where  $W_\mu^a$  ( $a = 1, 2, 3$ ) are the SU(2) fields with generators  $\tau_a$  and coupling constant  $g$ , and  $B_\mu$  is  
 595 the U(1) field with coupling constant  $g'$ .

596 Isolating the potential term:

$$V(\phi) = \mu^2 \phi^\dagger \phi + \lambda(\phi^\dagger \phi)^2 \quad (2.6)$$

597 a choice must be made on the sign of  $\mu^2$ , and the case of interest is for  $\mu^2 < 0$ . This results in  
 598 the famous “mexican hat potential” shown in Figure 2.1, which is minimized along the collection of  
 599 points:

$$\phi^\dagger \phi = \frac{1}{2} (\phi_1^2 + \phi_2^2 + \phi_3^2 + \phi_4^2) = -\frac{\mu^2}{2\lambda} \quad (2.7)$$

600 This means that the minimum of the potential is not at  $\phi = 0$  (as it would be in the case where  
 601  $\mu^2 > 0$ ), but rather at a value:

$$v \equiv \sqrt{-\frac{\mu^2}{\lambda}} \quad (2.8)$$

602 With no loss of generality due to the SU(2) symmetry,  $\phi_1 = \phi_2 = \phi_4 = 0$  can be set in Equation 2.7  
 603 leaving  $\phi_3^2 = v^2$ . Finally, the *vacuum expectation value* (VEV) of the field can be written as:

$$\langle \phi \rangle = \sqrt{\frac{1}{2}} \begin{pmatrix} 0 \\ v \end{pmatrix} \quad (2.9)$$

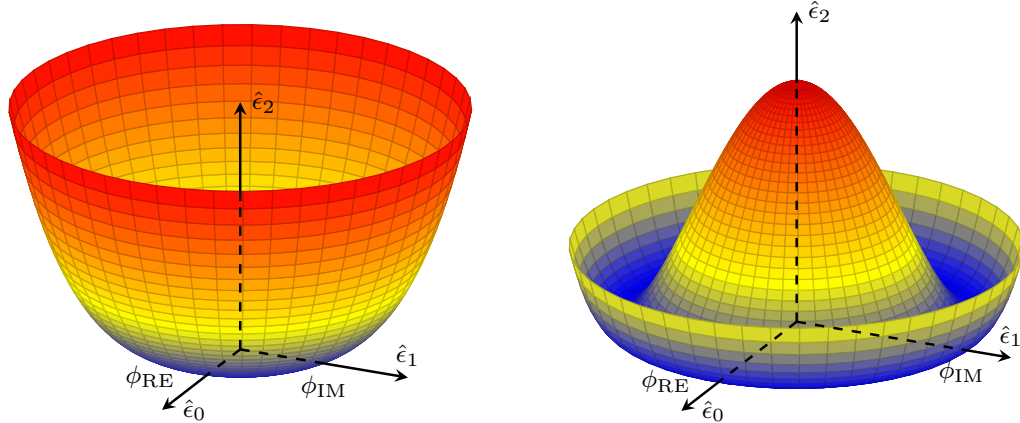


Figure 2.1: An illustration of the potential term  $V(\phi)$  in the cases where  $\mu^2 > 0$  (left) and  $\mu^2 < 0$  (right). The right-hand plot shows the Higgs potential, or “Mexican hat potential”, with the minimum at  $|\phi| = \sqrt{-\frac{\mu^2}{\lambda}}$  rather than at  $|\phi| = 0$  as in the left-hand plot.

604 The VEV can be substituted back into the original Lagrangian in Equation 2.4, and, following  
 605 quite a bit of math, a collection of mass terms can be identified:

$$\mathcal{L} \subset \mathcal{L}_M \equiv \frac{1}{8} v^2 g^2 \left[ (W_\mu^1)^2 + (W_\mu^2)^2 \right] + \frac{1}{8} v^2 \left[ g^2 (W_\mu^3)^2 - 2gg' W_\mu^3 B^\mu + g'^2 (B_\mu)^2 \right] \quad (2.10)$$

606 Focusing on the first term for the moment, substituting in Equation 2.2 for the physical  $W^\pm$  bosons,  
 607 the mass term can be seen clearly:

$$M_W^2 W^+ W^- = \left(\frac{1}{2}vg\right)^2 W^+ W^- \quad (2.11)$$

608

$$M_W = \frac{1}{2}vg \quad (2.12)$$

609 With a bit of clever forward-thinking, the second term of Equation 2.10 can be rewritten as:

$$\frac{1}{8}v^2 \left[ gW_\mu^3 - g'B_\mu \right]^2 + 0 \left[ g'W_\mu^3 - gB_\mu \right]^2 = \frac{1}{2}M_Z^2 Z_\mu^2 + \frac{1}{2}M_A^2 A_\mu^2 \quad (2.13)$$

610 where  $Z_\mu^2$  and  $A_\mu^2$  represent the physical  $Z$  boson and photon, respectively, and are defined as:

$$Z_\mu = \frac{gW_\mu^3 - g'B_\mu}{\sqrt{g^2 + g'^2}} \quad (2.14)$$

611

$$A_\mu = \frac{g'W_\mu^3 - gB_\mu}{\sqrt{g^2 + g'^2}} \quad (2.15)$$

612 From this, it can be seen that the photon is massless, and the mass of the  $Z$  boson is identified as:

$$M_Z = \frac{1}{2}v\sqrt{g^2 + g'^2} \quad (2.16)$$

613 Lastly, the Higgs field can couple directly to the fermions. Taking the electron as an example,  
 614 an additonal Lagrangian term can be written:

$$\mathcal{L}_e = -G_e [\bar{e}_L \phi e_R + \bar{e}_R \phi^\dagger e_L] \quad (2.17)$$

615 where  $e_L$  and  $e_R$  are the left-handed doublet and right-handed singlet, respectively, and  $\phi$  is as in  
 616 Equation 2.3. The symmetry can be spontaneously broken by a perturbation about the VEV:

$$\phi = \sqrt{\frac{1}{2}} \begin{pmatrix} 0 \\ v + h(x) \end{pmatrix} \quad (2.18)$$

617 which, when substituted into  $\mathcal{L}_e$  gives:

$$\begin{aligned} \mathcal{L}_e &= -\frac{G_e}{\sqrt{2}}v(\bar{e}_L e_R + \bar{e}_R e_L) - \frac{G_e}{\sqrt{2}}(\bar{e}_L e_R + \bar{e}_R e_L)h \\ &= -m_e \bar{e}e - \frac{m_e}{v} \bar{e}eh \end{aligned} \quad (2.19)$$

618 for electron mass  $m_e = \frac{G_e v}{\sqrt{2}}$ . From the second term, it can be seen that the strength of the Higgs  
 619 coupling to the electron is proportional to the mass of the electron. The rest of the fermion couplings  
 620 follow from this example.

621 What is accomplished here is quite remarkable. The weak and electromagnetic interactions have  
 622 been unified into a single  $SU(2) \times U(1)$  interaction, and the physical bosons observed in nature arise  
 623 as mixtures of the four gauge fields. Additionally, the non-zero VEV of the Higgs field results in  
 624 masses for the  $W^\pm$  and  $Z$  bosons while the photon remains massless. Additionally, it is shown that  
 625 the Higgs couples to fermions in proportion to their mass. From experimental measurements, the  
 626 value of the VEV has been determined to be  $v \approx 246$  GeV [19]. However, it should be noted that the  
 627 theory does not predict the mass of the Higgs boson or of the fermions; these must all be determined  
 628 from experiment.

### 629 2.3 Diboson physics

630 Processes involving two final state gauge bosons are of particular interest for testing the predictive  
 631 power of the SM. Due to the non-Abelian nature of the EWK interaction, the corresponding gauge  
 632 bosons are allowed to self-interact. This results in triple and quartic couplings of gauge bosons  
 633 (TGCs and QGCs, respectively). The SM allowed TGCs are the  $WW\gamma$  and  $WWZ$  vertices, and  
 634 the QGCs predicted by the model include  $WWZ\gamma$ ,  $WW\gamma\gamma$ ,  $WWZZ$ , and  $WWWW$ . These ver-  
 635 tices are accessible via a number of production modes at hadron colliders, including vector boson  
 636 fusion and scattering (VBF and VBS, as in Figure 2.2). The LHC in particular has provided the  
 637 first opportunity to observe some of these vertices, such as the  $WW\gamma\gamma$  QGC via the  $W\gamma\gamma$  final  
 638 state [20], or the  $WWWW$  QGC via same-sign  $W^\pm W^\pm$  production [21]. Precise measurements of  
 639 these processes can be compared to the theoretical predictions, and deviations can point to deficien-  
 640 cies in the prediction, such as needing an additional order in  $\alpha_s$  in the calculation, or even hints at  
 641 new physics, like anomalous gauge couplings<sup>2</sup> [22].

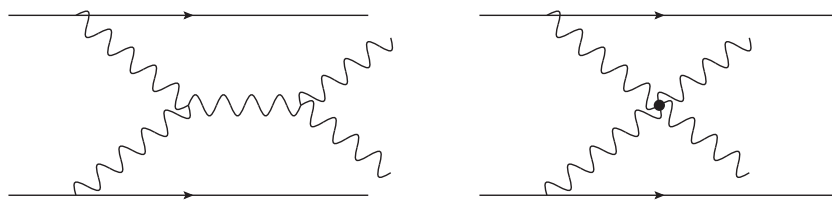


Figure 2.2: Vector boson fusion involving triple gauge couplings (left) and vector boson scattering involving a quartic gauge coupling (right).

642 Diboson interactions also make up one of the most sensitive tests of EWSB. Aside from the

---

<sup>2</sup>In the SM, the TGCs and QGCs are fixed by the electromagnetic coupling constant  $\alpha$  and the electroweak mixing angle  $\theta_W$ . In many Beyond the Standard Model scenarios, these couplings are modified by additional contributions.

643 top quark, the EWK bosons have the strongest coupling to the Higgs mechanism, as there are  
644 several production diagrams involving the exchange of a Higgs boson, including those in Figure 2.3.  
645 In this instance, VBS processes are particularly important as the Higgs unitarizes the scattering  
646 amplitude [23] (this particular aspect will be explored in more detail in the context of same-sign  
647  $W^\pm W^\pm$  scattering in Section 5.0.2). Since the Higgs boson has only recently been discovered, it has  
648 not yet been extensively tested, and there could still be deviations in the EWSB mechanism that  
649 may manifest in the VBF and VBS measurements [24].

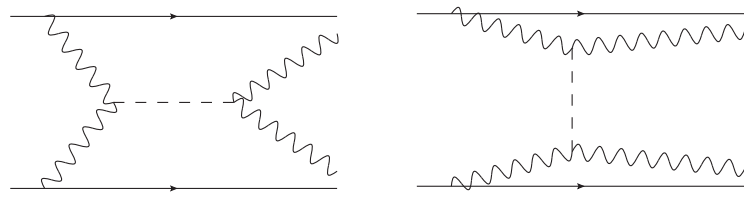


Figure 2.3: Diboson diagrams involving the  $s$ -channel (left) and  $t$ -channel (right) exchanges of a Higgs boson.

650

## CHAPTER 3

---

651

# LHC and the ATLAS Detector

---

652 **3.1 The Large Hadron Collider**

653 The Large Hadron Collider (LHC) [25] is...

654 **3.2 The ATLAS Detector**

655 ATLAS is a general-purpose particle detector...

656 **3.2.1 The Inner Detector**

657 The Inner Detector serves the primary purpose of measuring the trajectories of charged particles...

658 **3.2.1.1 Pixel Detector**

659 The Pixel detector consists of four cylindrical barrel layers and three disk-shaped endcap layers...

660 **3.2.1.2 Semiconductor Tracker**

661 The Semiconductor Tracker uses the same basic technology as the Pixels, but the fundamental unit  
662 of silicon is a larger “strip”...

663 **3.2.1.3 Transition Radiation Tracker**

664 The Transition Radiation Tracker is the outermost component of the ID...

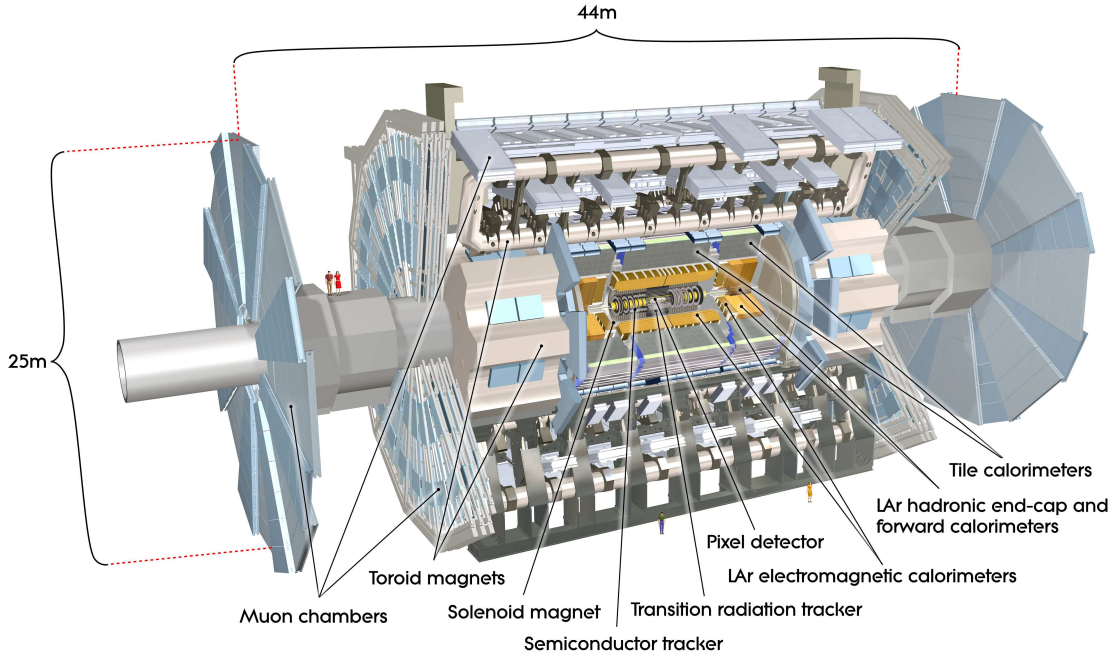


Figure 3.1: General cut-away view of the ATLAS detector [26].

### 665 3.2.2 The Calorimeters

666 ATLAS includes two types of calorimeter system for measuring electromagnetic and hadronic showers.  
 667 These are the Liquid Argon (LAr) calorimeters and the Tile calorimeters. Together, these cover  
 668 the region with  $|\eta| < 4.9\dots$

#### 669 3.2.2.1 Liquid Argon Calorimeters

670 The Liquid Argon system consists of...

#### 671 3.2.2.2 Tile Calorimeters

672 The Tile calorimeter provides coverage for hadronic showers...

### 673 3.2.3 The Muon Spectrometer

674 Muon spectrometer stuff.

675    **3.2.4 Particle reconstruction**

676    Particle reconstruction algorithms

677    **3.2.4.1 Track reconstruction**

678    **3.2.4.2 Muon reconstruction**

679    **3.2.4.3 Electron reconstruction**

680    **3.2.4.4 Jet reconstruction**

## CHAPTER 4

# Alignment of the ATLAS Inner Detector

683 When a charged particle passes through the ATLAS ID, it leaves hits in the sensors along its path.  
684 In order to accurately measure the track of the particle, it is necessary to know where these hits  
685 occurred as precisely as possible, which in turn requires knowledge of the physical location of the  
686 element that registered the hit. If one of these elements is *misaligned*, or displaced relative to its  
687 position in the known detector geometry, the assumed location of the corresponding hit will not  
688 match its actual location, resulting in an incorrect track fit. These misalignments can occur for  
689 any number of reasons, including but not limited to elements shifting during maintenance periods  
690 or cycles in ATLAS’s magnetic field, or small movements during normal detector operations. The  
691 effect of a misaligned detector element on the track reconstruction is shown in Figure 4.1.

692 In order to correct the misalignments, the ID alignment procedure is applied to accurately  
693 determine the physical position and orientation of each detector element. The baseline accuracy of  
694 the alignment is required to be such that the track parameter resolutions are not degraded by more  
695 than 20% with respect to those derived from a perfect detector geometry<sup>3</sup>. This corresponds to a  
696 precision of better than  $10\mu\text{m}$  in the positioning of the elements of the silicon detectors [27].

697 This chapter outlines the ID alignment procedure, the alignment of the detector during the 2015  
698 data taking period, and the steps taken to measure momentum biases in the alignment.

<sup>3</sup>The so-called *perfect geometry* refers to the description of the ATLAS detector in which every sensor precisely matches its design specifications. The perfect geometry contains no misalignments, and the position of each sensor is known exactly.

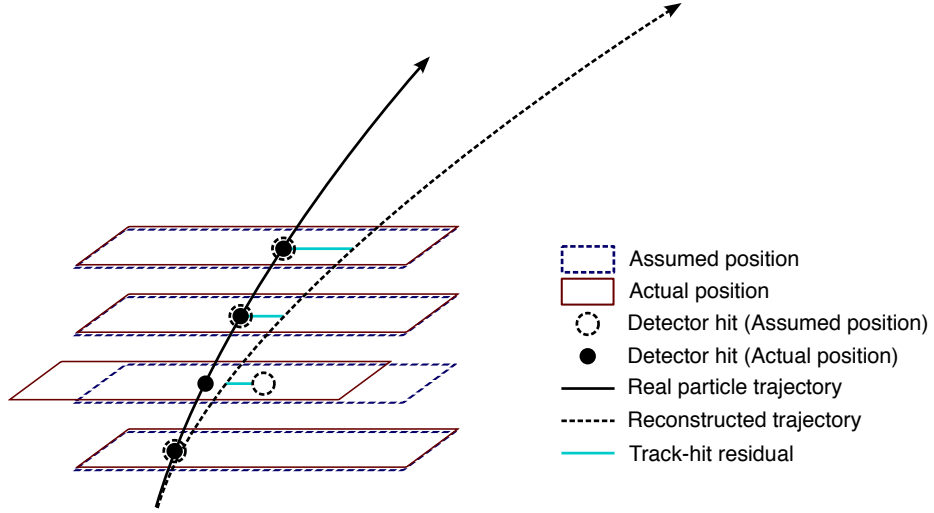


Figure 4.1: Graphical representation of the effect of a misaligned detector element. The reconstructed particle track (dashed arrow) differs from the actual trajectory of the particle (solid arrow) due to the shift in one of the detector elements. The cyan lines represent the track-to-hit residuals.

#### 699 4.1 The alignment method

700 The alignment procedure uses track-based algorithm that updates the locations of detector elements  
 701 in order to minimize the set of track-hit *residuals*. These residuals are defined as the distance between  
 702 the fitted track position in a given detector element to the position of the hit recorded by the same  
 703 element, and are shown by the cyan lines in Figure 4.1. Tracks in ATLAS are parameterized as  
 704 five-dimensional vectors [28]:

$$\vec{\tau} = (d_0, z_0, \phi_0, \theta, q/p) \quad (4.1)$$

705 where  $d_0$  and  $z_0$  are the transverse and longitudinal impact parameters with respect to the origin,  
 706 respectively,  $\phi_0$  is the azimuthal angle of the track at the point of closest approach to the origin,  $\theta$   
 707 is the polar angle, and  $q/p$  is the charge of the track divided by its momentum. The residual for the  
 708  $i^{\text{th}}$  hit of a given track can then be written in terms of the track parameters  $\vec{\tau}$  and a set of alignment  
 709 parameters  $\vec{a}$  that describe the hit location [29]:

$$r_i(\vec{\tau}, \vec{a}) = (\vec{m}_i - \vec{e}_i(\vec{\tau}, \vec{a})) \cdot \hat{k} \quad (4.2)$$

710 where  $\vec{e}_i$  is the intersection point of the extrapolated track with the sensor,  $\vec{m}_i$  is the position of the  
 711 associated hit within the sensor, and  $\hat{k}$  is the unit vector defining the direction of the measurement  
 712 within the sensor.  $\vec{r}$  is then the vector of residuals for the given track.

713 A  $\chi^2$  function can be built from the residuals of all collected tracks:

$$\chi^2 = \sum_{\text{tracks}} \vec{r}^T V^{-1} \vec{r} \quad (4.3)$$

714 where  $V$  is the covariance matrix of the hit measurements. The  $\chi^2$  function is then minimized with  
 715 respect to the alignment parameters  $\vec{a}$ , which contain all degrees of freedom being aligned. The  
 716 minimization condition with respect to  $\vec{a}$  is:

$$\frac{d\chi^2}{d\vec{a}} = 0 \rightarrow 2 \sum_{\text{tracks}} \left( \frac{d\vec{r}}{d\vec{a}} \right)^T V^{-1} \vec{r} = 0 \quad (4.4)$$

717 This equation can be difficult to solve exactly, so the residual is rewritten as a first order Taylor  
 718 expansion:

$$\vec{r} = \vec{r}_0 + \frac{d\vec{r}}{d\vec{a}} \delta\vec{a} \quad (4.5)$$

719 where  $\vec{r}_0$  is dependent on an initial set of track and alignment parameters  $\vec{r}_0$  and  $\vec{a}_0$ , respectively;  
 720 the track parameter dependence has also been folded into the total derivative  $\frac{d\vec{r}}{d\vec{a}}$ . Equation 4.5 can  
 721 then be inserted into the minimization condition from Equation 4.4 to give:

$$\left[ \sum_{\text{tracks}} \left( \frac{d\vec{r}}{d\vec{a}} \right)^T V^{-1} \left( \frac{d\vec{r}}{d\vec{a}} \right) \right] \delta\vec{a} + \sum_{\text{tracks}} \left( \frac{d\vec{r}}{d\vec{a}} \right)^T V^{-1} \vec{r}_0 = 0 \quad (4.6)$$

722 From this equation, the alignment matrix  $\mathcal{M}_a$  and alignment vector  $\vec{\nu}_a$  can be defined:

$$\mathcal{M}_a = \sum_{\text{tracks}} \left( \frac{d\vec{r}}{d\vec{a}} \right)^T V^{-1} \left( \frac{d\vec{r}}{d\vec{a}} \right) \quad (4.7)$$

723

$$\vec{\nu}_a = \sum_{\text{tracks}} \left( \frac{d\vec{r}}{d\vec{a}} \right)^T V^{-1} \vec{r}_0 \quad (4.8)$$

724 Finally, the alignment corrections  $\delta\vec{a}$  can be solved for by inverting the alignment matrix:

$$\delta\vec{a} = -\mathcal{M}_a^{-1} \vec{\nu}_a \quad (4.9)$$

725 which is a linear system of equations with a number of equations equal to the number of alignment  
 726 degrees of freedom [30].

727 Inverting the matrix and solving this system of equations is referred to as *Global  $\chi^2$*  align-  
 728 ment [29]. This can be useful, as  $\mathcal{M}_a$  contains all the correlations between the alignable structures.  
 729 However, inverting the matrix becomes difficult when the number of degrees of freedom becomes  
 730 large, and as the number of alignable structures increases, so too does the size of the matrix  $\mathcal{M}_a$ .  
 731 Eventually inverting the matrix becomes too computationally intensive to be practical.

This problem is solved by the *Local*  $\chi^2$  algorithm [31]. In this case, the alignment matrix is constructed to be block-diagonal, allowing for it to be inverted even for large numbers of degrees of freedom. This is achieved by replacing the full derivative in Equation 4.6 with the partial derivative  $\frac{\partial \vec{r}}{\partial \vec{a}}$ . The new alignment matrix  $\mathcal{M}'_a$  and alignment vector  $\vec{\nu}'_a$  become:

$$\mathcal{M}_a = \sum_{\text{tracks}} \left( \frac{\partial \vec{r}}{\partial \vec{a}} \right)^T V^{-1} \left( \frac{\partial \vec{r}}{\partial \vec{a}} \right) \quad (4.10)$$

$$\vec{\nu}_a = \sum_{\text{tracks}} \left( \frac{\partial \vec{r}}{\partial \vec{a}} \right)^T V^{-1} \vec{r}_0 \quad (4.11)$$

Inverting  $\mathcal{M}'_a$  is considerably faster and less intensive even for large numbers of degrees of freedom; however, the correlations between the alignable structures is lost.

Due to the Taylor expansion used in Equation 4.6, several iterations of the alignment algorithm may be necessary to converge on a final set of alignment constants. The Local  $\chi^2$  alignment typically requires more iterations due to the loss of the correlation information [32]. In practice, the ATLAS reconstruction is run over a set of events, and the resulting tracks are fed to the alignment algorithm. The residuals are calculated, the alignment matrix is built and inverted, and a new set of alignment constants is obtained. The convergence of the alignment can be checked by:

1. Measure the  $\Delta\chi^2$  with the previous iteration. If it is near zero, then the  $\chi^2$  is approaching its minimum.

2. Looking at the residual distributions for different alignable structures. A well aligned detector will have a mean residual of zero with a width approximating the intrinsic resolution of the detector.

If the above checks are satisfied, the process is finished and the final alignment constants are read out; if not, another iteration is performed. A visual representation of the alignment chain is shown in Figure 4.2.

Since a  $\chi^2$  minimization is used to align the detector, if there is a systematic misalignments in the detector that does not adversely affect the  $\chi^2$ , the algorithm will be insensitive to it. These misalignments are referred to as *weak modes*, and special care is taken to remove them [33]. One potential impact of weak modes is a bias in the track momentum of reconstructed particles. This particular effect is the subject of Section 4.4.

In practice, the detector is aligned both in “real-time” as data is collected, and during dedicated offline alignment campaigns. The real-time alignment is run in ATLAS’s so-called *calibration loop*,

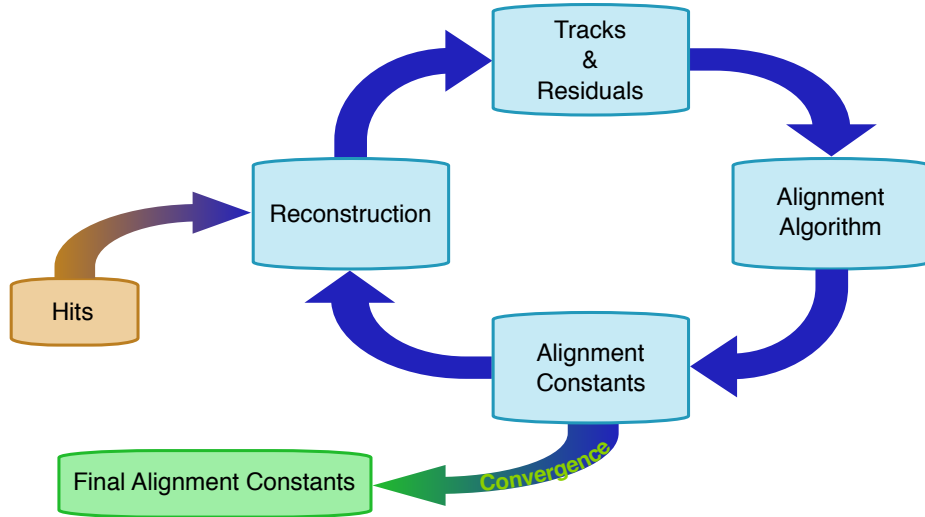


Figure 4.2: Graphical representation of the ID alignment chain.

which comprises the first stage in the preparation of data for physics analysis. The calibration loop requires the alignment as well as various other detector calibrations to be available within 48 hours for initial data processing. A fast, coarse-grained alignment<sup>4</sup> is run on a subset of the available data containing full tracking information, and the results are propagated to the reconstruction of that particular run [34]. Due to the time constraints of the calibration loop, a full sensor-by-sensor alignment is not possible.

The more thorough and finely tuned alignments are reserved for the dedicated alignment campaigns. These generally occur early in data taking campaigns, typically once a sufficient amount of data is collected after a detector shutdown, in order to obtain a good baseline alignment for use in the remainder of the data collection period. Once data taking is complete, another campaign determines an improved set of alignment constants (divided into several “blocks” to account for time-dependent misalignments), and the full data is reprocessed using the newly derived detector geometry. The initial offline alignment of the ATLAS detector at the beginning of Run 2 in 2015 is the subject of Section 4.2.

#### 4.1.1 Alignment levels

The alignment of the detector is performed at several levels of increasing granularity. This adds flexibility in being able to align only as finely as needed, and it also allows for global, detector-level

<sup>4</sup>The calibration loop runs up to a Level 2 alignment in the silicon detectors, which involves treating each layer of sensors as a single object, defined in greater detail in Table 4.1.

777 misalignments to be corrected first before dealing with finer adjustments.

- 778     ● Level 1 (L1) alignment involves moving entire subdetector components as a single unit, such  
779       as the entire Pixel detector, or the SCT barrel. These often have the largest misalignments,  
780       but they are easily corrected and do not require large volumes of data to do so.
- 781     ● Level 2 (L2) alignment treats individual layers in the silicon detectors (modules in the TRT)  
782       and end cap disks as individual alignable objects.
- 783     ● Level 2.7 (L27) alignment was introduced with the addition of the IBL to the ID in Run 2. It  
784       involves the stave-by-stave alignment of the IBL and Pixel barrel<sup>5</sup>.
- 785     ● Level 3 (L3) alignment treats each sensor in the silicon detectors and each straw in the TRT  
786       as an individual alignable object. It is the finest grained alignment available but also the most  
787       computationally intensive due to the large number of degrees of freedom. The large number  
788       of individual detector sensors being aligned also requires the largest amount of statistics.

789 The different alignment levels are listed in more detail in Table 4.1, including the number of alignable  
790 structures and associated degrees of freedom for each detector component.

791 The implementation of the alignment algorithm in the software is flexible enough to allow each  
792 subsystem to be aligned individually at a specified level. Each alignable structure has six degrees of  
793 freedom: 3 translations ( $T_x, T_y, T_z$ ) and 3 rotations ( $R_x, R_y, R_z$ )<sup>6</sup>; however individual degrees of  
794 freedom may be turned on and off as required. In a typical alignment job, L1 and L2 contain few  
795 enough degrees of freedom that the Global  $\chi^2$  algorithm can be used, but L3 alignments (which can  
796 contain over 36,000 degrees of freedom in the silicon detectors alone) require the Local  $\chi^2$  algorithm.

#### 797 4.1.2 Alignment coordinate systems

798 The global coordinate system ( $x, y, z$ ) used by the ID alignment matches that of the ATLAS detector  
799 in general. The positions and orientations of individual detector modules of the ID are defined by  
800 a right-handed local coordinate system ( $x', y', z'$ ) where the origin is defined as the geometrical  
801 center of the module. The  $x'$ -axis for each silicon module is defined to point along the most sensitive  
802 direction of the module, the  $y'$ -axis is oriented along the long side of the module, and the  $z'$ -axis is

---

<sup>5</sup>For the purposes of this Chapter, the term “Pixel” will refer to the original three layers of the Pixel detector, and the IBL will be referenced separately.

<sup>6</sup>The TRT is an exception, as the subdetector does not have any resolution along the length of the straw. Therefore, for the barrel,  $T_z$  is omitted. Similarly for the straws themselves, only two parameters are defined: translation with respect to the radial direction ( $T_\phi$ ) and rotation with respect to the radial axis ( $R_r$  for the barrel and  $R_z$  for the end-caps) [35].

Level	Description of alignable structure	Structures	DoF
1	IBL detector	1	6
	Whole Pixel detector	1	6
	SCT barrel and 2 end-caps	3	18
	TRT barrel and 2 end-caps ( $T_z$ fixed)	3	17
Total:		8	47
2	IBL detector	1	6
	Pixel barrel layers	3	18
	Pixel end-cap disks	$2 \times 3$	36
	SCT barrel layers	4	24
	SCT end-cap disks	$2 \times 9$	108
	TRT barrel 32 modules ( $T_z$ fixed)	$3 \times 32$	480
	TRT end-cap wheels	$2 \times 40$	480
Total:		208	792
2.7	IBL staves	14	84
	Pixel barrel staves	$22+38+52$	672
	Pixel end-cap disks	$2 \times 3$	18
	Total:		132
3	IBL modules	280	1,680
	Pixel modules	1,744	10,464
	SCT modules	4,088	24,528
	TRT barrel wires ( $T_\phi, R_r$ only)	105,088	210,176
	TRT end-cap wires ( $T_\phi, R_Z$ only)	245,760	491,520
	Total silicon sensors:		6,112
	Total TRT wires:		350,848
Total:		36,672	701,696

Table 4.1: The four alignment levels for each of the detector subsystems. The total number of alignable structures and degrees of freedom (DoF) to be aligned are given for each level.

803 orthogonal to the  $(x', y')$  plane. For the TRT straws, the  $x'$ -axis is perpendicular to both the wire  
 804 and the radial direction, defined from the origin of the global frame to the straw center, the  $y'$ -axis  
 805 points along the straw, and once again the  $z'$ -axis is orthogonal to the  $(x', y')$  plane. A depiction of  
 806 the global and local coordinate systems for the ID is shown in Figure 4.3.

807 When considering the alignment degrees of freedom listed earlier in Section 4.1.1, grouped collec-  
 808 tions of modules, layers, or entire subdetectors use the global coordinate system; individual modules  
 809 use their respective local coordinate systems. The translations  $T_i$  are with respect to the origin of  
 810 the given reference frame, and the rotations  $R_i$  are taken about the Cartesian axes.

## 811 4.2 Early 2015 alignment of the ATLAS detector

812 At the end of Run 1, the LHC was shut down for upgrades and maintenance. During this time,  
 813 a number of upgrades were performed on the ATLAS detector, including the installation of a new

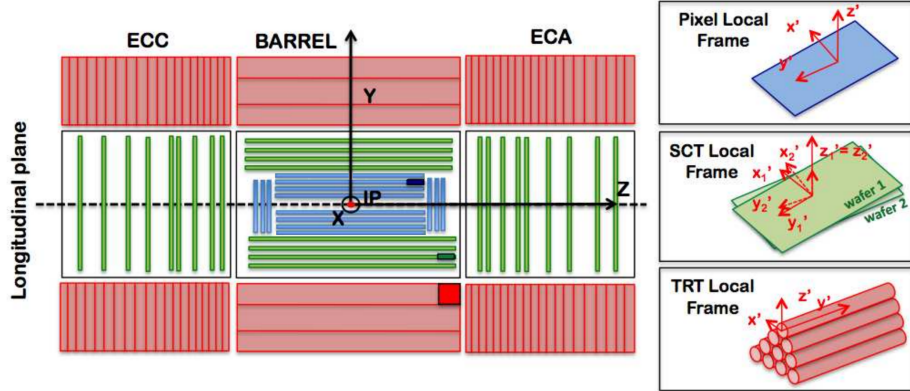


Figure 4.3: A schematic representation of the Inner Detector in the longitudinal plane with the global coordinate system overlaid on top. The Pixel detector and IBL are shown in blue, the SCT in green, and the TRT in red. The local coordinates for each subdetector module are inset on the right. Image taken from [36].

814 innermost layer of the Pixel detector, the Insertable B-Layer (IBL) [37]. TODO: This will certainly  
 815 be defined in the detector description, so maybe the citation and abbreviation are not needed These  
 816 changes to the ID required some detector components to be removed temporarily, and many elements  
 817 shifted relative to each other over the course of the maintenance process. In order to correct for these  
 818 large detector movements prior to  $\sqrt{s} = 13$  TeV collision data taking, an alignment was performed  
 819 using cosmic ray data collected in early 2015 [36]. This alignment was able to correct for the majority  
 820 of the large detector-wide misalignments as well as determine the global position of the IBL at the  
 821 micron level.

822 In June of 2015, shortly after the data taking period began, the first track-based alignment  
 823 of the refurbished ID was performed using  $\mathcal{L} = 7.9 \text{ pb}^{-1}$  of  $\sqrt{s} = 13$  TeV  $pp$  collision data [38].  
 824 Starting from the initial geometry determined by the cosmic ray alignment, referred to hereafter  
 825 as the *March alignment*, an improved set of alignment constants, called the *June alignment*, was  
 826 derived from a data set of approximately 1.4 million selected tracks. For comparison, a MC sample  
 827 containing approximately 2.7 million tracks was constructed from dijet events simulated using a  
 828 perfect detector geometry; the MC events are reweighted to match the  $\eta$  and  $p_T$  distributions found  
 829 in the data. Additional validation of the alignment results uses a set of cosmic ray data collected  
 830 by the detector during the LHC collisions.

---

**831 4.2.1 June alignment procedure**

832 The data set used as the input for the alignment contains a subset of physics events used for prompt  
 833 reconstruction recorded at a rate of 10 Hz. To ensure that only high quality tracks are used for the  
 834 alignment, each track is required to have transverse momentum  $p_T > 3$  GeV, contain at least one  
 835 hit in the Pixel detector, at least seven hits in the combined silicon detectors, and at least 25 hits  
 836 in the TRT.

837 A full L3 alignment of the IBL was included in the March alignment; however, a realignment  
 838 was necessary. Since the cosmic rays pass through the detector top-down, the staves on the sides of  
 839 the IBL could not be aligned as precisely as those on the top and bottom due to lower statistics.  
 840 Additionally, the IBL was operating at a temperature of  $-20^\circ\text{C}$  during the cosmic data taking  
 841 and at  $-10^\circ\text{C}$  for collision data taking. This proved to be significant, as it was observed that  
 842 the IBL staves experience a temperature-dependent, parabolic bowing in the local  $x'$ -direction of  
 843 approximately  $-10\mu\text{m/K}$  [39]. As a result, a full L3 alignment of the IBL was essential in order to  
 844 correct for the bowing. Due to it being a brand new element of the detector as well as its importance  
 845 in vertexing and  $b$  jet tagging, aligning the IBL sensors with a high degree of precision was of great  
 846 importance.

847 The June alignment was performed in two stages, with the first pass focusing on relative move-  
 848 ments of the big structures and correcting for the bowing of the IBL. The March alignment corrected  
 849 for these larger movements as well; however, it was observed during Run 1 that these sort of mis-  
 850 alignments are introduced by changing conditions in the detector [33], such as in the cooling system  
 851 or magnet power cycling, which may have occurred between the early cosmic data taking and the  
 852 first  $\sqrt{s} = 13$  TeV collisions. The silicon detectors were aligned at several different levels and the  
 853 IBL was aligned at the module level; the TRT detector was kept fixed to act as a global reference  
 854 frame. The full alignment chain for the first pass consisted of the following steps:

- 855 1. The IBL, Pixel, and SCT detectors were aligned at L1. The SCT barrel was not aligned in  
 856  $T_z$  in order to constrain global displacements along the  $z$ -axis, as the TRT is not sensitive to  
 857 that degree of freedom.
- 858 2. The IBL, and Pixel barrel and end-caps, and SCT barrel were aligned at L2. The SCT end-caps  
 859 were aligned at L1.
- 860 3. The IBL and pixel barrel were aligned at L27, using all six degrees of freedom. The Pixel  
 861 end-cap disks were only aligned in the plane ( $T_x$ ,  $T_y$ , and  $R_z$ ). The SCT was treated the same

862 as in the previous step.

863 4. The IBL was aligned at L3 using all six degrees of freedom for each module.

864 The primary goal for the second pass was to remove a bias in the transverse impact parameter  
 865  $d_0$  present in the March alignment. The resolution of  $d_0$  was also poorer than expected. In order  
 866 to correct for this, an additional constraint was passed to the alignment by adding an impact  
 867 parameter with respect to the beam spot as a pseudo-measurement [40]. When the alignment  
 868 algorithm minimizes the  $\chi^2$ , it will take care of the impact parameter minimization as well. Only  
 869 the IBL and Pixel detectors were aligned in this step. The stages of the second pass are listed below,  
 870 and the beam spot constraint was used in each:

871 1. The IBL and Pixel detectors were aligned at L2 with the SCT fixed.

872 2. The IBL was aligned at L27

873 3. The IBL and Pixel barrel and end-caps were aligned at L3.

874 The set of alignment constants obtained at the end of the second pass represents the June alignment.

875 The highest level of alignment over the course of the two passes for each subdetector is listed in  
 876 Table 4.2.

Detector		Highest level of alignment
IBL		L3
Pixel	Barrel	L3
	End-caps	L3 ( $T_x$ , $T_y$ , and $R_z$ only)
SCT	Barrel	L2 (except $T_z$ )
	End-caps	L1
TRT		None

Table 4.2: Summary of the highest level of alignment applied to each ID subsystem when deriving the June alignment.

### 877 4.2.2 Alignment results

878 The primary measure of alignment quality is assessed by looking at the track-hit residual distributions.  
 879 If the detector is well aligned, the residuals will be Gaussian-distributed with a mean  
 880 of zero and a width approximating the detector's resolution. The residual distributions are con-  
 881 structed from the same selection of tracks that were used to perform the alignment, and are the  
 882 focus of Section 4.2.2.1. A second check on the alignment involves observables sensitive to the track

parameter resolution. In this case, cosmic rays are used, making use of a “split track” technique that takes advantage of the top-to-bottom cosmic ray trajectory (compared to the center-out trajectory of collision tracks). This method and the corresponding tests of the alignment are detailed in Section 4.2.2.2

Additionally, the effect of the beam spot constrained alignment on the impact parameter  $d_0$  needs to be checked. The  $d_0$  distributions for both the March and June alignments are compared to the MC simulation using a perfect geometry in Figure 4.4. In the March alignment, there is a bias of 18  $\mu\text{m}$  in the mean of the distribution and the width is nearly twice that of the perfect geometry. After the second pass of the June alignment, the mean has shifted to 1  $\mu\text{m}$  and the distribution has narrowed considerably. From this, it appears that the constrained alignment successfully removed the  $d_0$  bias.

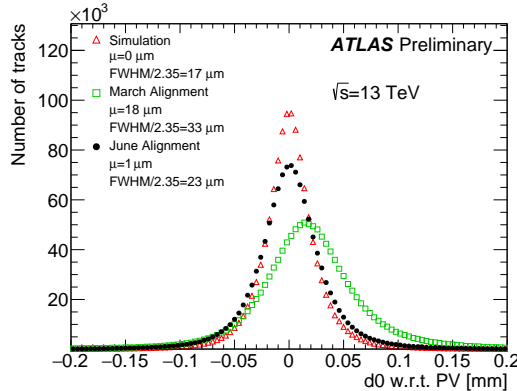


Figure 4.4: The  $d_0$  distributions with respect to the reconstructed primary vertex using the  $\sqrt{s} = 13$  TeV collision data sample reconstructed using the June (black) and March (green) alignments. The data is compared to a MC simulation using a perfect detector geometry (red). The distributions are normalized to the same number of entries.

#### 4.2.2.1 Residual distributions from collisions

As mentioned previously, the primary focus of the June alignment campaign was on the IBL and the Pixel detectors. The detectors are the closest to the beam line and have the finest resolutions of the ID subdetectors. The residual distributions in local  $x$  and  $y$  of the IBL planar sensors<sup>7</sup> are shown in Figure 4.5. These and subsequent figures in this section compare the June and March alignments to the perfectly-aligned MC simulation. Noticeable improvement in the distribution widths can be

<sup>7</sup>The IBL contains 12 planar sensors in the center of a stave, with four 3D sensors on either end. Only the planar sensors are shown here due to low statistics in the 3D sensors as well as poor MC modeling of these sensors.

seen in both the local  $x$ - and  $y$ -directions, nearly matching the simulation in local  $x$ , which is the most sensitive direction.

Due to the temperature-dependent bowing of the IBL, it is also interesting to look at the means of the residual distributions for each ring of IBL sensors along the beam line, as shown in Figure 4.6. A deformation is clearly visible in the March alignment in both measurement directions, and the shape in the local  $x$ -direction is consistent with an average stave bowing due to the different operating temperature of the IBL during the March alignment and the 13 TeV collisions. This feature was nearly eliminated in both directions through the L3 alignment of the IBL sensors.

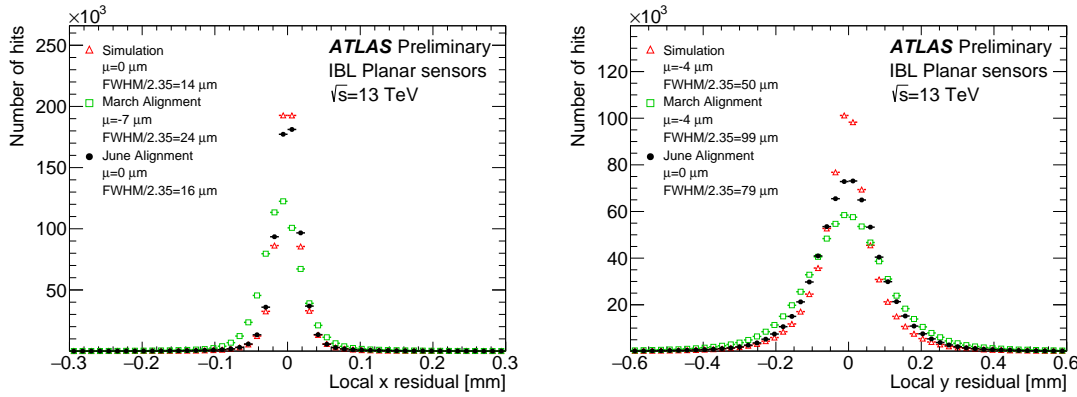


Figure 4.5: Local  $x$  (left) and local  $y$  (right) residual distributions of the IBL planar sensors using the  $\sqrt{s} = 13$  TeV collision data sample reconstructed using the June (black) and March (green) alignments. The data is compared to a MC simulation using a perfect detector geometry (red). The distributions are normalized to the same number of entries.

The local  $x$  and  $y$  residual distributions for the Pixel detector barrel and end-caps are shown in Figure 4.7. Even though the IBL is not included in the plots of the barrel, some of the noticeable improvement in the more sensitive local  $x$  direction is an effect of the improved IBL alignment. Similarly, the relatively broad local  $y$  residual distribution in the barrel likely indicates that further refinement of the IBL alignment was needed along that direction. Even so, the June alignment outperforms the March alignment and rivals the simulation in most of the plots.

Similar distributions for the SCT and TRT barrel and end-caps are shown in Figures 4.8 and 4.9, respectively. Much like with the Pixel residuals, there is a reduction in the width of the TRT residuals between the March and June alignments due to the alignment of the other subdetectors improving the quality of the track fit. Even though neither subdetector was aligned at module-level, the residuals indicate that the previous L3 alignment performed in Run 1 has not degraded

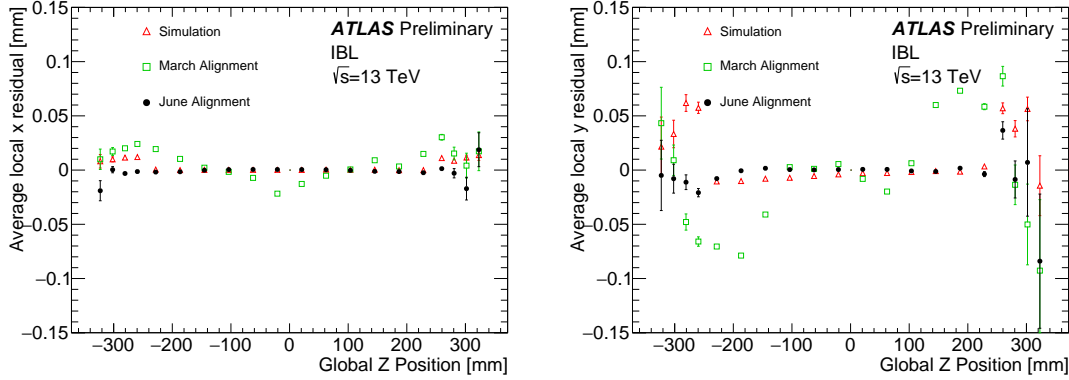


Figure 4.6: The mean of the local  $x$  (left) and local  $y$  (right) residual distributions as a function of the global  $z$  position of each IBL module using the  $\sqrt{s} = 13$  TeV collision data sample reconstructed using the June (black) and March (green) alignments. The data is compared to a MC simulation using a perfect detector geometry (red).

significantly during the upgrade and maintenance period.

#### 4.2.2.2 Track parameter resolution from cosmic rays

Cosmic ray data is very useful as an independent check on the alignment in the barrel of the detector. While tracks from  $pp$  collisions originate within the detector and travel outwards, a cosmic ray that passes through the center of the detector leaves a track in both halves of the detector. If the cosmic ray is split in half, as in Figure 4.10, then it can be treated as two separate tracks each with nearly identical track parameters (some differences arise due to energy loss as the particle passes through the detector). The distribution of the difference in a given track parameter  $\Delta\tau$  is approximately Gaussian with a variance  $\sigma^2(\Delta\tau)$ . Since both tracks come from the same particle, each track individually has a variance equal to  $\sigma^2(\Delta\tau)/2$ . The resolution of the track parameter is then given by the root mean square of the distribution divided by  $\sqrt{2}$ .

Cosmic rays whose split tracks each had transverse momentum  $p_T > 2$  GeV and at least one, eight, and 25 hits in the barrels of the Pixel, SCT, and TRT detectors, respectively, were selected to measure a collection of track parameters. Figure 4.11 shows the difference in the impact parameter  $\Delta d_0$  and the charge divided by the transverse momentum  $\Delta q/p_T$  of the selected split-track cosmic rays for both the March and June alignments. Both distributions show a reduction in width in the June alignment, corresponding to an improvement in the resolution of each track parameter. The  $\Delta d_0$  plot shows a significant improvement in the June alignment, further validating the removal of

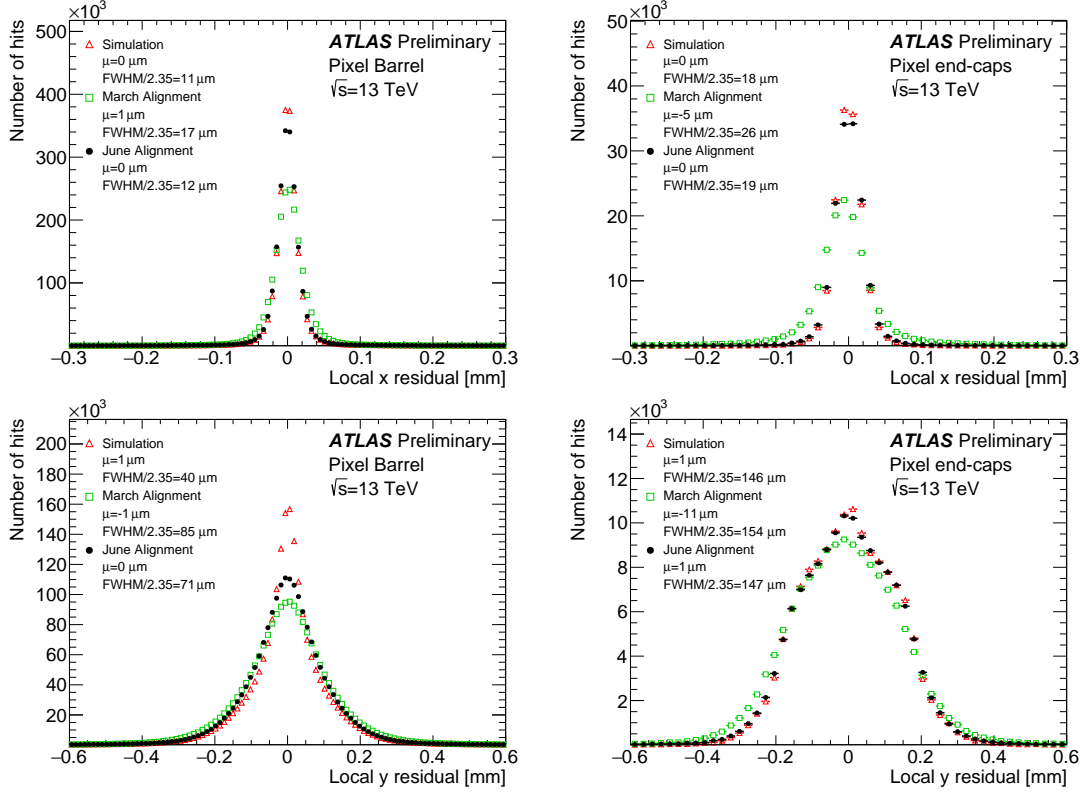


Figure 4.7: Local  $x$  (top) and local  $y$  (bottom) residual distributions for the Pixel barrel (excluding the IBL, left) and end-caps (right) using the  $\sqrt{s} = 13$  TeV collision data sample reconstructed using the June (black) and March (green) alignments. The data is compared to a MC simulation using a perfect detector geometry (red). The distributions are normalized to the same number of entries.

937 the bias in the impact parameter.

### 938 4.2.3 Error scaling

939 The final step in preparing the new set of June alignment constants deals with the adjustment of  
 940 the hit errors, or *error scaling*. Knowledge of the exact position of a hit measurement on a track  
 941 is limited by the accuracy with which the sensors' positions are known. Let  $\sigma$  represent the hit  
 942 uncertainty used in track fitting, and  $\sigma_0$  be the detector's intrinsic uncertainty. If  $\sigma = \sigma_0$ , the pull  
 943 of the track-hit residual distributions should form a Gaussian distribution centered at zero with a  
 944 standard deviation  $\sigma = 1$  [30]. In the case of residual misalignment, the pull distributions' standard  
 945 deviations will stray from unity. The hit uncertainty can be written as:

$$\sigma = a \cdot \sigma_0 \oplus b \quad (4.12)$$

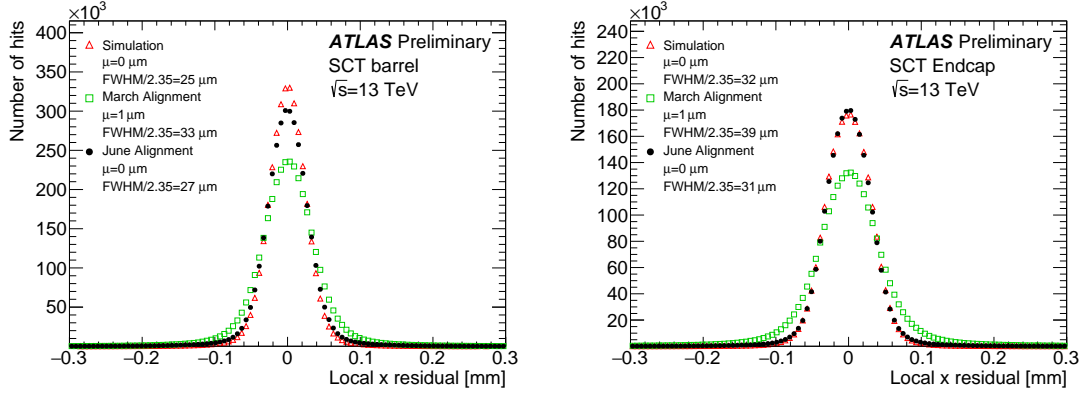


Figure 4.8: Local  $x$  residual distributions for the SCT barrel (left) and end-caps (right) using the  $\sqrt{s} = 13 \text{ TeV}$  collision data sample reconstructed using the June (black) and March (green) alignments. The data is compared to a MC simulation using a perfect detector geometry (red). The distributions are normalized to the same number of entries.

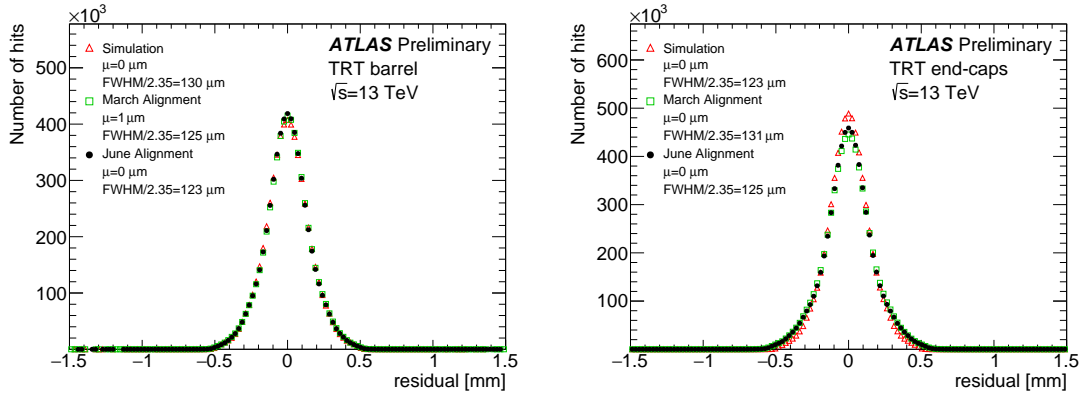


Figure 4.9: Residual distributions for the TRT barrel (left) and end-caps (right) using the  $\sqrt{s} = 13 \text{ TeV}$  collision data sample reconstructed using the June (black) and March (green) alignments. The data is compared to a MC simulation using a perfect detector geometry (red). The distributions are normalized to the same number of entries.

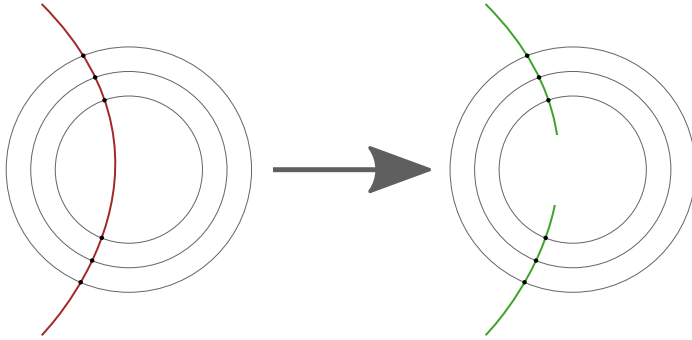


Figure 4.10: Representation of splitting a single cosmic ray track passing through the entire detector (left) into two separate tracks (right).

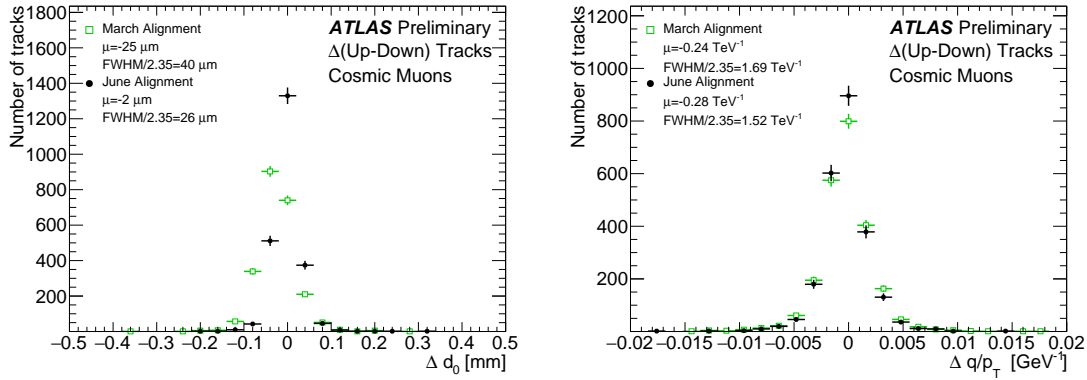


Figure 4.11: Distribution of the difference in the impact parameter  $\Delta d_0$  (left) and charge over transverse momentum  $\Delta q/p_T$  (right) between the two cosmic ray split tracks. The June (black) and March (green) alignments are compared. The distributions are normalized to the same number of entries.

where  $a$  is a scaling factor, and  $b$  is a constant term which can be interpreted as a measure of any remaining misalignment of the detector elements. In this alignment campaign, the value of  $a$  is fixed at  $a = 1$  and  $b$  is evaluated from the residual pull distributions for each subdetector in its sensitive directions.

Once the value of  $b$  is determined, pull distributions derived from the new value of  $\sigma$  should have unit width. The error scaling values for each subdetector are listed in Table 4.3, and the pull distributions for the IBL after error scaling are shown in Figure 4.12.

Detector	Coordinate	$b(\mu\text{m})$
IBL	$x$	6.4
	$y$	43.6
Pixel	$x$	5.2
	$y$	28.6
Pixel	$x$	7.5
	$y$	0
SCT	$x$	10.8
	$x$	8.6
TRT	$r\phi$	0
	$r\phi$	0

Table 4.3: Estimated value of the error scaling term  $b$  for each subdetector component with the June alignment.

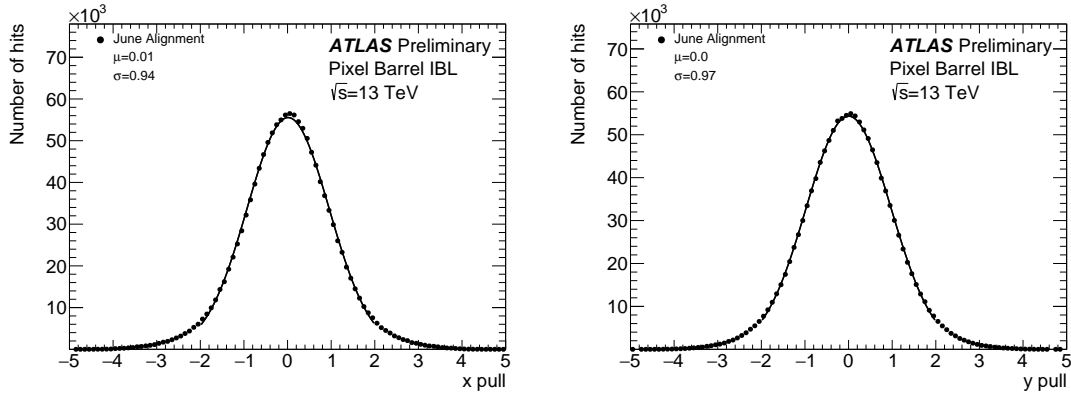


Figure 4.12: Pull distributions in local  $x$  (left) and  $y$  (right) for the IBL using the  $\sqrt{s} = 13 \text{ TeV}$  collision data sample after applying the error scaling.

### 953 4.3 Level 2 alignment of the TRT

954 During validation of the final end-of-year reprocessing of the 2015 data, a misalignment was found in  
 955 the barrel of the TRT detector, as several modules (triangular clusters of straws) showed rotations in  
 956 the local  $y$  coordinate. The then-best available constants included a full L3 alignment of the silicon  
 957 detectors and a separate L2 alignment of the TRT. However, not all degrees of freedom were enabled  
 958 when the TRT was aligned. To correct for these tilts, an additional four iterations of L2 alignment  
 959 TRT was performed on the TRT enabling all available degrees of freedom ( $T_x$ ,  $T_y$ ,  $R_x$ ,  $R_y$ , and  $R_z$   
 960 in the barrel, and  $T_x$ ,  $T_y$ , and  $R_z$  for the endcaps). Plots of the residual means from barrel  $\phi$  sectors  
 961 containing modules affected by the tilt misalignment are shown in Figure 4.13 before and after the  
 962 L2 alignment.

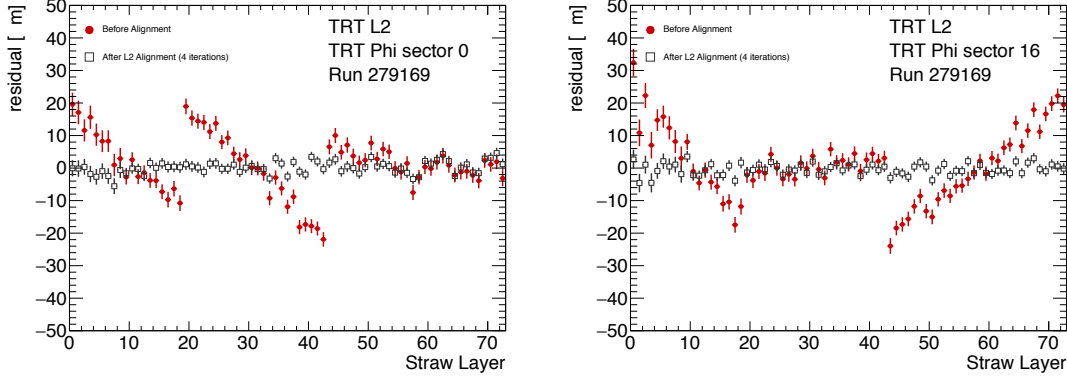


Figure 4.13: Residual means by straw layer in two TRT  $\phi$ -sectors affected by a tilt misalignment. The tilts in each of the three modules are clearly visible in the red points representing the reconstructed data prior to alignment. After four iterations of L2 alignment, the residual means in the gray points are flat.

Following the L2 alignment, some additional time was taken to determine if a full wire-by-wire L3 alignment of the TRT was necessary. The TRT was last aligned at L3 during Run 1, but initial alignment campaigns in Run 2 did not show signs of misalignment, as can be seen from the residual distributions in Figure 4.9. In order to assess the alignment more carefully, two dimensional residual maps in  $\phi$  and  $z$  were constructed for each layer in the TRT barrel and endcaps using the current alignment. These maps were compared to a similar set using the L3 alignment from 2010, from which it was determined that the straw-level alignment indeed hadn't degraded and a new L3 alignment was not needed. The maps for the first layer of the TRT barrel are shown in Figure 4.14 for both sets of alignment constants.

#### 4.4 Momentum bias from sagitta deformations

A variety of weak mode deformations can exist in the detector even after alignment. As mentioned previously, these weak modes consist of misalignments which don't affect the  $\chi^2$  of the residuals and thus are not handled by the basic alignment algorithm. In the presence of a weak mode, the description of the detector geometry can still provide efficient and high quality track fits, but there may also be systematic biases in one or more track parameters. Several weak modes, their impacts on the reconstruction, and the steps taken to eliminate them are detailed in [33, 41]. This section focuses specifically on sagitta distortions that result in a bias in the reconstructed track momentum.

These *sagitta* distortions consist of detector movements orthogonal to the trajectory of the outgo-

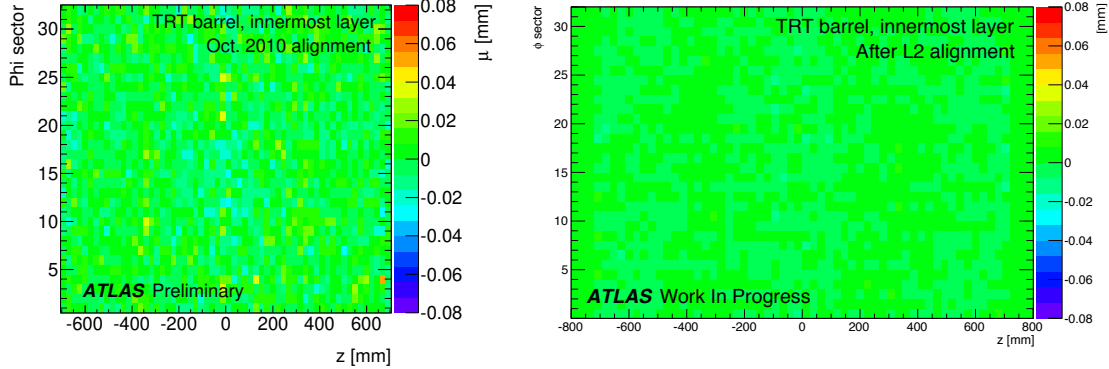


Figure 4.14: Two dimensional map of residuals in the first layer of the TRT barrel vs  $z$  and  $\phi$ . Each bin represents the mean of a Gaussian fit to the TRT residuals in that bin. The map on the left is after the L3 (wire-by-wire) alignment of the TRT performed in 2010, and the map on the right is after the L2 alignment at the end of 2015. The  $z$ -axis for both plots use the same scale. Left figure taken from [30].

981 ing particle. The effect on the reconstructed track curvature is different for positively and negatively  
 982 charged particles, resulting in a charge-antisymmetric bias. This effect is illustrated in the curl  
 983 deformation shown in Figure 4.15.

984 In the plane transverse to ATLAS’s magnetic field, outgoing particle tracks form circular arcs.  
 985 The sagitta is defined as the distance from the center of this arc to the center of its base, as shown in  
 986 Figure 4.16, and it represents the “amount of bending” in the track. In the case where the sagitta  $s$   
 987 is considerably smaller than the detector radius  $R_0$ , which is a valid assumption when working with  
 988 high momentum tracks, the transverse momentum of a particle of charge  $q$  can be written as [42]:

$$p_T \propto qB \frac{R_0^2}{8s} \quad (4.13)$$

989 where  $B$  is the strength of the detector’s magnetic field. If a sagitta bias is present, the track’s  
 990 transverse momentum shifts by [41]:

$$q/p_T \rightarrow q/p_T + \delta_s \quad \text{or} \quad p_T \rightarrow p_T \cdot (1 + qp_T \delta_s)^{-1} \quad (4.14)$$

991 where  $\delta_s$  is a universal bias parameter that uniquely defines the deformation. Finally, since the  
 992 reconstructed polar angle does not change under a sagitta deformation, the longitudinal component  
 993 of the momentum scales along with the transverse component, and an equivalent equation can be  
 994 written for the total momentum:

$$p \rightarrow p \cdot (1 + qp_T \delta_s)^{-1} \quad (4.15)$$

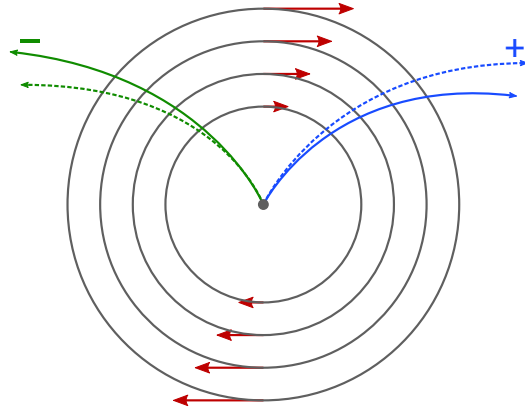


Figure 4.15: Representation of a curl distortion in the detector. The image shows a cutaway in the transverse plane. The deformation is represented by the red arrows, and the impact on the reconstructed positive (blue) and negative (green) tracks are shown. The dashed lines represent the true particle trajectories, and the solid lines represent the reconstructed trajectories.

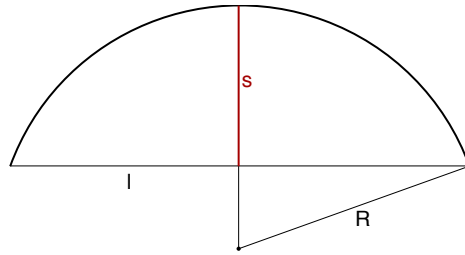


Figure 4.16: Geometric definition of the sagitta  $s$  in relation to the length of the chord  $l$  and the radius  $r$  of a circular arc.

#### 995 4.4.1 Sagitta bias monitoring with electron $E/p$

996 Since a sagitta bias results in changes in the momentum of particles' tracks as measured by the ID,  
 997 they can be identified using independent measurements from other systems in the detector. One  
 998 such method involves using the energy-momentum ratio of electrons ( $E/p$ ). Since the electron's  
 999 energy is measured in ATLAS's calorimeter systems, it is not sensitive to any sagitta bias that may  
 1000 exist in the ID and the corresponding track momentum. Under the assumption that the calorimeter  
 1001 response is independent of the charge of incoming particles, a charge-dependent momentum bias in  
 1002 the ID will manifest as a difference in the  $E/p$  ratio for electrons and positrons.

1003 In the presence of a sagitta bias, the momentum will change according to Equation 4.15 and the  
 1004 average measured  $\langle E/p \rangle$  can be written as:

$$\langle E/p \rangle^\pm \rightarrow \langle E/p \rangle^\pm \pm \langle E_T \rangle \delta_s \quad (4.16)$$

1005 where the approximation  $p_T \approx E_T$  is used. Assuming that  $\langle E/p \rangle^+ = \langle E/p \rangle^-$  in the absense of a  
 1006 bias, the sagitta bias parameter can be written as:

$$\delta_s = \frac{\langle E/p \rangle^+ - \langle E/p \rangle^-}{2\langle E_T \rangle} \quad (4.17)$$

1007 If the kinematic selections for electrons and positrons are identical, the energy scale of the calorimeter  
 1008 will not factor into the  $\langle E/p \rangle$  difference; however, it will affect  $\langle E_T \rangle$  which would scale the measured  
 1009  $\delta_s$ . This is expected to be a small effect, as the energy scale for electrons has been measured at  
 1010  $\sqrt{s} = 13$  TeV with uncertainties on the per-mil level across the entire detector [43].

#### 1011 4.4.1.1 Measuring $\langle E/p \rangle$

1012 The  $E/p$  ratio is measured using electrons and positrons from  $Z \rightarrow e^\pm e^\mp$  events in order to obtain  
 1013 a high purity sample of electron candidates. They are required to pass a basic selection criteria to  
 1014 ensure they are well measured by both the ID and the calorimeters:

- 1015 •  $E_T > 25$  GeV
- 1016 •  $|\eta| < 2.47$ , excluding the calorimeter’s barrel-to-endcap transition region in  $1.37 < |\eta| < 1.52$
- 1017 • Pass MediumLH identification working point detailed in Section 3.2.4.3
- 1018 • Pass a selection of quality cuts, including a requirement that the electron be identified using  
 1019 cluster information in the calorimeter
- 1020 • The associated track must have at least one hit in the IBL, three in the Pixel detector, and  
 1021 five in the SCT detector.

1022 Events with exactly two opposite-charge electrons passing this selection with a dielectron invariant  
 1023 mass within 30 GeV of the  $Z$  boson mass are then used for the  $E/p$  calculation.

1024 Since the size of the sagitta bias  $\delta_s$  is not expected to be constant across the entire detector,  
 1025 a two-dimensional rectangular grid binned in detector  $\eta$  and  $\phi$  is constructed. From the selected  
 1026 events, separate distributions of  $E/p$  are made for electrons and positrons lying in each bin. Each  
 1027 distribution is fit with Crystal Ball function<sup>8</sup>, and the peak of the distribution is taken as the value  
 1028 of  $\langle E/p \rangle$ . If there is no bias on the track momentum in the bin, the peaks for electrons and positrons  
 1029 should match. Example  $E/p$  distributions including the Crystal Ball fits are shown in Figure 4.17.

---

<sup>8</sup>The Crystal Ball function is a probability density function consisting of a Gaussian core and a power-law tail.

1030 It is important to emphasize that deviations from one in the *ratio* of  $\langle E/p \rangle$  for electrons and  
 1031 positrons indicates that a momentum bias may be present. The value of  $\langle E/p \rangle$  itself is not expected  
 1032 to equal one exactly, as the track momentum on average tends to be slightly lower than the energy  
 1033 measurement in the calorimeter. This is due to the fact that if the electron were to radiate a photon,  
 1034 its momentum would change slightly, while it is likely that both the electron and the emitted photon  
 1035 would leave energy deposits near each other in the calorimeter and be reconstructed into the same  
 1036 object.

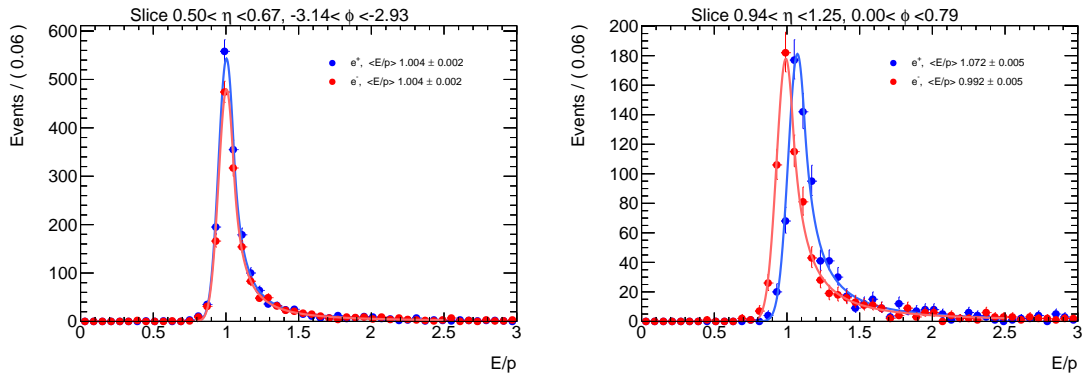


Figure 4.17:  $E/p$  distributions of electrons and positrons in two different  $\eta\text{-}\phi$  bins of the detector. The left hand plot is taken from a region with no momentum bias where  $\langle E/p \rangle^+ = \langle E/p \rangle^-$ , while the right hand plot shows an 8% disagreement in  $\langle E/p \rangle$  between electrons and positrons.

1037 Once the  $\langle E/p \rangle^\pm$  distributions in each  $\eta\text{-}\phi$  bin have been extracted from the fits, a two dimensional map of  $\delta_s$  can be constructed using Equation 4.17. The map gives an overview of sagitta  
 1038 biases that may be present in the detector, and can be used by the alignment algorithm to reduce  
 1039 the bias in the next iteration. In this case, the tracks fed to the alignment have their momenta  
 1040 corrected according to [41]:

$$q/p_{\text{corr}} = q/p_{\text{reco}}(1 - qp_T\delta_s) \quad (4.18)$$

1042 where  $p_{\text{reco}}$  is the reconstructed momentum of the track. The corrected momentum is then con-  
 1043 strained in the alignment.

#### 1044 4.4.1.2 Results in 13 TeV data

1045 The  $E/p$  method has been used to monitor sagitta biases in the detector several times over the  
 1046 course of Run 2. During this time, it has primarily served as an independent cross-check to a  
 1047 second method using  $Z \rightarrow \mu^\pm \mu^\mp$  events [41]. The  $Z \rightarrow \mu^\pm \mu^\mp$  method identifies individual track  
 1048 momentum biases through shifts in the reconstructed  $Z$  mass, which leaves it relatively insensitive

1049 to global sagitta biases. For this reason, the sagitta bias maps produced using this technique are  
 1050 normalized to those from the  $E/p$  method before being used to constrain the alignment.

1051 The results of two implementations of the  $E/p$  method are presented here.

- 1052 1. The first follows the end-of-year reprocessing of the entire ATLAS 2016 data set at  $\sqrt{s} =$   
 1053 13 TeV. Two sets of alignment constants are compared: the *prompt* alignment, which was  
 1054 derived shortly after each run was recorded, and the *reprocessed* alignment. The maps of the  
 1055 sagitta bias comparing the two alignments calculated using the  $E/p$  method are shown in  
 1056 Figure 4.18, and the comparison of the  $\eta$  projection of each map is shown in Figure 4.19.
- 1057 2. The second uses the 2017 data after reprocessing, and compares the effects of multiple it-  
 1058 erations of the method. In each iteration, the momenta of the electrons and positrons are  
 1059 corrected based on Equation 4.15 using the value of  $\delta_s$  computed in the previous iteration,  
 1060 and a new sagitta bias map is calculated. If the method is indeed characterizing the sagitta  
 1061 biases correctly, the corrections should converge quickly. The initial sagitta bias map is com-  
 1062 pared to the map after two such iterations in Figure 4.20, and the sagitta bias projected along  
 1063  $\eta$  for each iteration is shown in Figure 4.21. Indeed, after just two iterations,  $\delta_s$  is consistent  
 1064 with zero in nearly all bins.

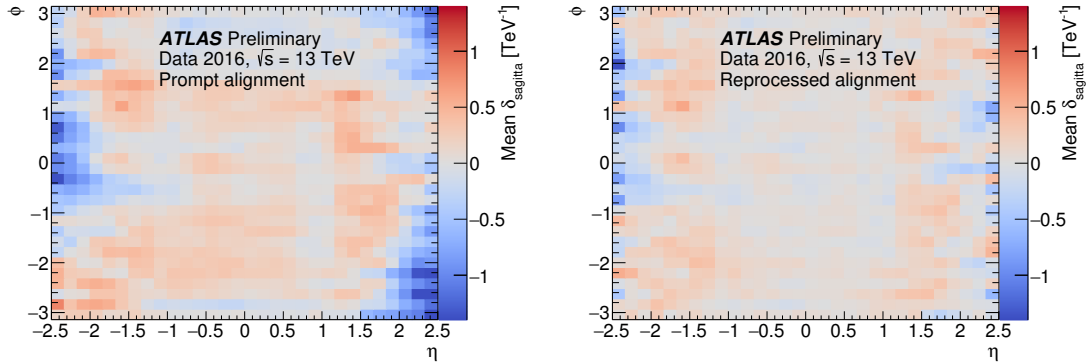


Figure 4.18: Sagitta bias in the  $\sqrt{s} = 13$  TeV data collected by ATLAS in 2016 as a function of  $\eta$  and  $\phi$  for the prompt (left) and reprocessed (right) alignments using the  $E/p$  method.

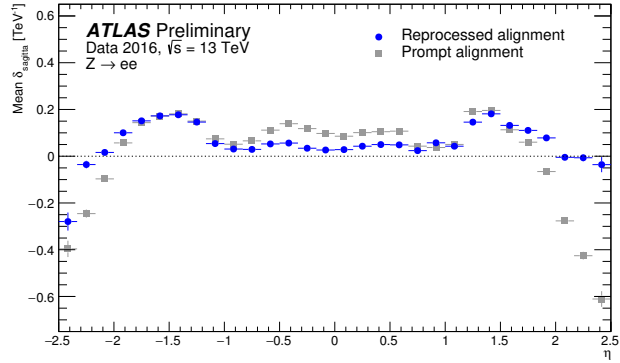


Figure 4.19: Sagitta bias in the  $\sqrt{s} = 13 \text{ TeV}$  data collected by ATLAS in 2016 projected along  $\eta$  for the prompt (gray) and reprocessed (blue) alignments using the  $E/p$  method.

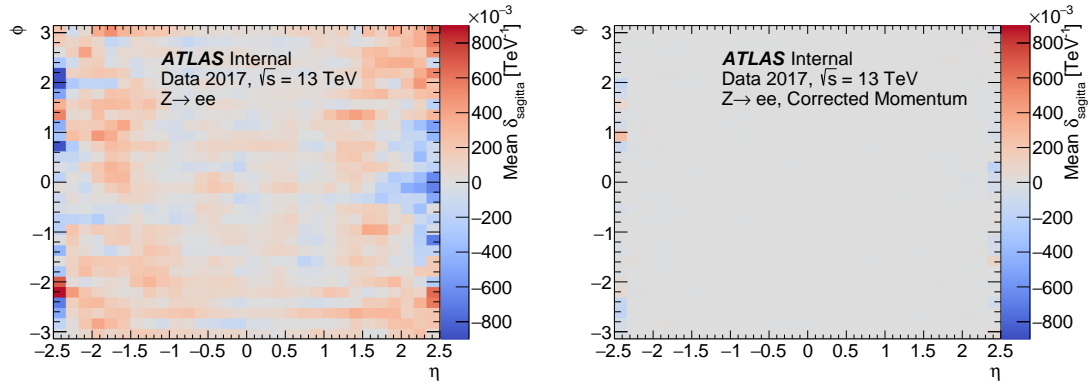


Figure 4.20: Sagitta bias in the  $\sqrt{s} = 13 \text{ TeV}$  data collected by ATLAS in 2017 as a function of  $\eta$  and  $\phi$  in reconstructed electrons (left) and after two iterations of momentum corrections (right) from the  $E/p$  method.

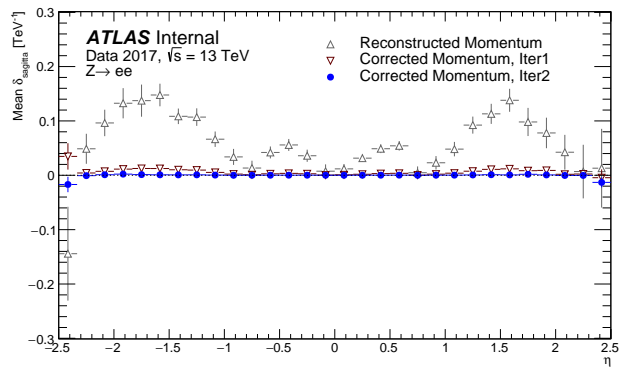


Figure 4.21: Sagitta bias in the  $\sqrt{s} = 13$  TeV data collected by ATLAS in 2017 projected along  $\eta$  in reconstructed electrons (gray) and after one (red) and two (blue) iterations of momentum corrections from the  $E/p$  method.

1065

## CHAPTER 5

1066

# Measurement of same-sign $WW$ 1067 production at $\sqrt{s} = 13$ TeV with ATLAS

---

1068 Production of same-sign  $W$  boson pairs is a particularly interesting SM process. When produced  
1069 via vector boson scattering (VBS),  $W^\pm W^\pm jj$  is particularly sensitive to the electroweak symmetry  
1070 breaking (EWSB) mechanism as well as potential “beyond the Standard Model” (BSM) physics.  
1071  $W^\pm W^\pm jj$  events can be produced via electroweak-mediated (EWK) diagrams, of which VBS is a  
1072 subset, or QCD-mediated diagrams. The biggest advantage of same-sign  $W^\pm W^\pm jj$  lies in its ratio  
1073 of electroweak (EWK) to QCD production cross sections. Despite the opposite-sign  $W^\pm W^\mp$  having  
1074 a considerably larger total cross section, its EWK-mediated diagrams are considerably smaller than  
1075 its QCD-mediated diagrams, while for same-sign  $W^\pm W^\pm$  the ratio is approximately one to one.  
1076 This makes  $W^\pm W^\pm jj$  one of the best channels for studying VBS at the LHC.

1077 The first evidence of electroweak (EWK)  $W^\pm W^\pm jj$  production was seen by the ATLAS and  
1078 CMS experiments at  $\sqrt{s} = 8$  TeV with excesses of  $3.6\sigma$  [21] and  $2.0\sigma$  [44] over backgrounds, respec-  
1079 tively. More recently, ATLAS and CMS have both observed the EWK process at  $\sqrt{s} = 13$  TeV  
1080 with significances of  $6.9\sigma$  [45] and  $5.5\sigma$  [46], respectively. The analysis presented in this chap-  
1081 ter is based off of the ATLAS  $\sqrt{s} = 13$  TeV observation and cross section measurement of EWK  
1082  $W^\pm W^\pm jj$  production [45, 47].

1083

### 5.0.2 Theoretical overview of vector boson scattering

1084 VBS processes are very important to understand due to their sensitivity to the EWSB mechanism.  
1085 The scattering amplitude of longitudinally polarized vector bosons grows with center-of-mass energy  
1086 and ultimately violates unitarity above  $\sqrt{s} = 1$  TeV in the absence of a light SM Higgs boson [48, 49].

1087 However, once the Higgs is introduced, the divergences cancel and the cross section no longer grows  
 1088 unbounded, as can be seen in Figure 5.1, which consists of plots from [50].

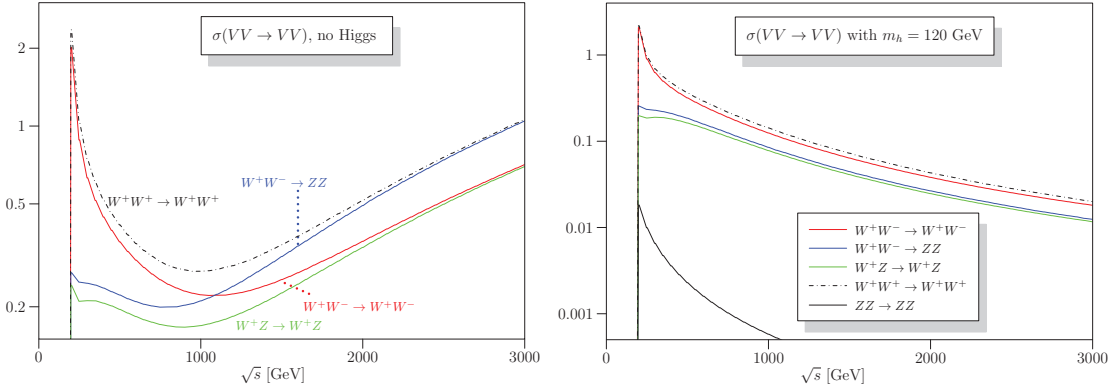


Figure 5.1: Cross sections in nanobarns for five different scattering processes of longitudinally polarized vector bosons as a function of center of mass energy  $\sqrt{s}$ . Without a SM Higgs boson (left), the cross sections grow unbounded with  $\sqrt{s}$ ; however with a 120 GeV Higgs boson (right), the cross sections no longer diverge. Plots taken from [50].

1089 With the discovery of the Higgs boson in 2012 [15, 16], the EWSB mechanism can now be directly  
 1090 studied. Due to the exchange of a Higgs in the  $s$ - and  $t$ -channel VBS diagrams ( $W^\pm W^\pm jj$  itself only  
 1091 contains the  $t$ -channel diagram), VBS processes are directly sensitive to properties of the Higgs. For  
 1092 example, the high-mass tail in the  $VV$  scattering system allows an approximation of the effective  
 1093 coupling strength of the Higgs to vector bosons that is independent of any assumptions on the Higgs  
 1094 width [51]. Additionally, the center of mass energy dependence of the  $VV$  scattering can reveal  
 1095 whether the Higgs boson unitarizes the longitudinal scattering amplitude fully or only partially [52].

1096 VBS events are characterized by two quarks from the colliding protons each radiating a massive  
 1097 vector boson which then scatter and decay in the detector. The incoming quarks carry a large  
 1098 amount of momentum and only deflect a small amount upon radiating the vector boson; as a result,  
 1099 they often travel very close to the beam line. Ignoring the decay products of the bosons, these VBS  
 1100 events result in a final state of two vector bosons ( $V$ ) and two jets ( $j$ ) at high pseudorapidities  
 1101 (called *forward jets*) from the outgoing quarks. The shorthand  $VVjj$  is used to represent this final  
 1102 state.

1103  $VVjj$  events can be produced via two different physical processes. The first involves purely  
 1104 electroweak interactions in the tree-level diagrams, with  $\mathcal{O}(\alpha_{EWK}) = 6$  and will be referred to as  
 1105 *EWK production*. This can be further broken down into VBS and non-VBS production. In the  
 1106 VBS EWK production, the scattering occurs via triple or quartic gauge couplings, as well as the

1107  $s$ - or  $t$ -channel exchange of a Higgs boson. The non-VBS EWK production contains the same final  
 1108 state of two vector bosons and two outgoing quarks, but the bosons do not scatter. Due to gauge  
 1109 invariance, it is not possible to separate the VBS from the non-VBS productions [53]; therefore,  
 1110 both are included in the signal generation and are indistinguishable from one another. The second  
 1111 process involves a mix of the EWK and strong interactions, of order  $\mathcal{O}(\alpha_s) = 2 \otimes \mathcal{O}(\alpha_{\text{EWK}}) = 4$  and  
 1112 will be referred to as *QCD production*. The tree-level Feynman diagrams for VBS EWK, non-VBS  
 1113 EWK, and QCD  $VVjj$  production are found in Figures 5.2, 5.3, and 5.4, respectively.

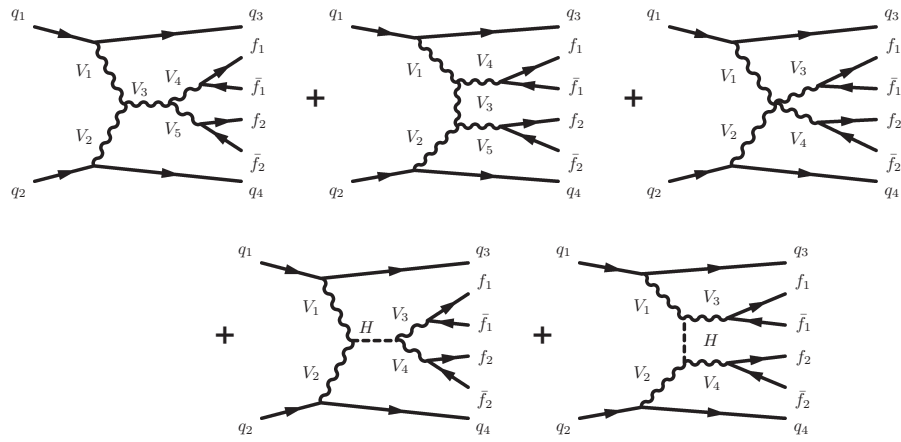


Figure 5.2: Tree-level Feynman diagrams for VBS EWK  $VVjj$  production including triple gauge couplings involving  $W$  and/or  $Z$  bosons (top left and top middle), quartic gauge coupling (top right), or the exchange of a Higgs boson ( $s$ -channel bottom left and  $t$ -channel bottom right). The labels are quarks ( $q$ ), fermions ( $f$ ), and gauge bosons ( $V = W, Z$ ).

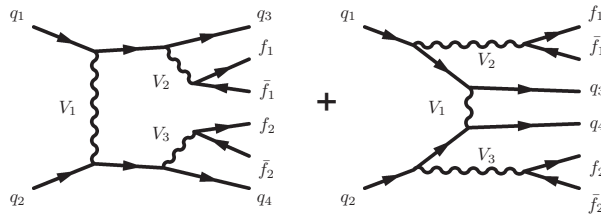


Figure 5.3: Tree-level Feynman diagrams for non-VBS EWK  $VVjj$  production. The labels are quarks ( $q$ ), fermions ( $f$ ), and gauge bosons ( $V = W, Z$ ).

### 1114 5.0.3 Same-sign $W^\pm W^\pm$ scattering

1115 Same-sign  $W^\pm W^\pm jj$  scattering is considered to be one of the best channels for studying VBS at the  
 1116 LHC [51]. This is due primarily to the ratio of the EWK to the QCD production, which matters

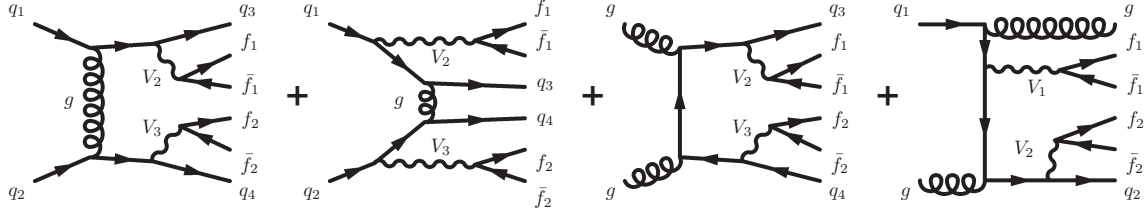


Figure 5.4: Tree-level Feynman diagrams for QCD  $VVjj$  production. The labels are quarks ( $q$ ), fermions ( $f$ ), and gauge bosons ( $V = W, Z$ ).

a great deal due to the VBS events being a subset of the total EWK production. In an analysis the EWK production would be considered the signal and the QCD production a background, so a favorable ratio of the two helps greatly when comparing the size of the signal to the backgrounds. A study at  $\sqrt{s} = 8$  TeV [54] was done using the **SHERPA** Monte Carlo (MC) generator to calculate EWK and QCD production cross sections at leading order for a variety of  $VVjj$  processes decaying to leptons and can be found in Table 5.1. Despite its lower cross section compared to other  $VVjj$  processes, the EWK to QCD ratio for  $W^\pm W^\pm jj$  is approximately one-to-one, whereas for opposite-sign  $W^\pm W^\mp jj$  the ratio is closer to 3%.

Process	Final state	$\sigma_{\text{EWK}}$	$\sigma_{\text{QCD}}$
$W^\pm W^\pm$	$l^\pm l^\pm \nu\nu jj$	19.5 fb	18.8 fb
$W^\pm W^\mp$	$l^\pm l^\mp \nu\nu jj$	91.3 fb	3030 fb
$W^\pm Z$	$l^\pm l^\pm l^\mp \nu jj$	30.2 fb	687 fb
$ZZ$	$l^+ l^- \nu\nu jj$	2.4 fb	162 fb
$ZZ$	$l^+ l^- l^+ l^- jj$	1.5 fb	106 fb

Table 5.1: Predicted cross sections for EQK and QCD production of diboson processes relevant to VBS at  $\sqrt{s} = 8$  TeV using the **SHERPA** MC generator. Loose generator level cuts are applied on lepton  $p_T > 5$  GeV, dilepton invariant mass  $m_{ll} > 4$  GeV, and at least two jets with  $m_{jj} > 10$  GeV. Numbers taken from [54].

This analysis studies  $W^\pm W^\pm jj$  scattering where both  $W$  bosons decay leptonically to  $e\nu$  or  $\mu\nu$ <sup>9</sup>. The  $W^\pm W^\pm jj$  VBS final state consists of two leptons with the same electric charge, two neutrinos, and two high energy forward jets with a large invariant mass. Tree-level Feynman diagrams of VBS  $W^\pm W^\pm jj$  production can be found in Figure 5.5 and a visual representation of the VBS topology can be found in Figure 5.6. The two forward jets also serve as a powerful tool to suppress the QCD production mode. In EWK events, the two jets tend to have much higher separation and a larger combined invariant mass than the two leading jets in a QCD event. The two plots shown in

<sup>9</sup>Throughout the rest of this chapter,  $l$  denotes either electrons ( $e$ ) or muons ( $\mu$ ) unless stated otherwise. Additionally,  $e$ ,  $\mu$ , and  $\nu$  (neutrino) with no charge or anti-particle designation refer interchangeably to either the particle or anti-particle.

1132 Figure 5.7 highlight the differences in these dijet quantities between the two production modes. An  
 1133 ATLAS event display of a real  $W^\pm W^\pm jj$  candidate event is shown in Figure 5.8.

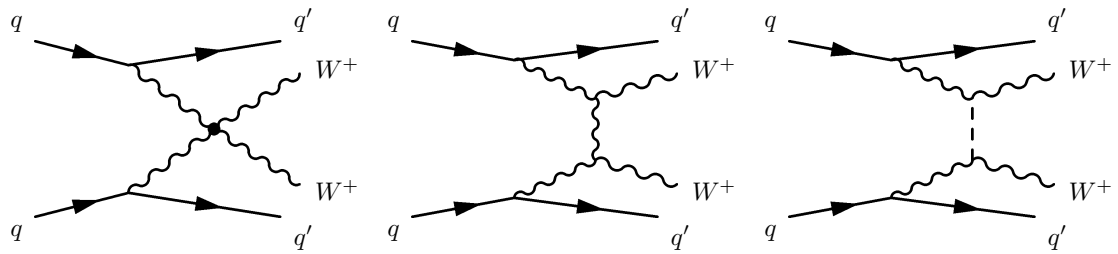


Figure 5.5: Feynman diagrams for VBS EWK production of  $W^\pm W^\pm jj$  events. The leftmost diagram contains a quartic gauge coupling vertex, and the rightmost diagram contains an exchange of a Higgs boson.

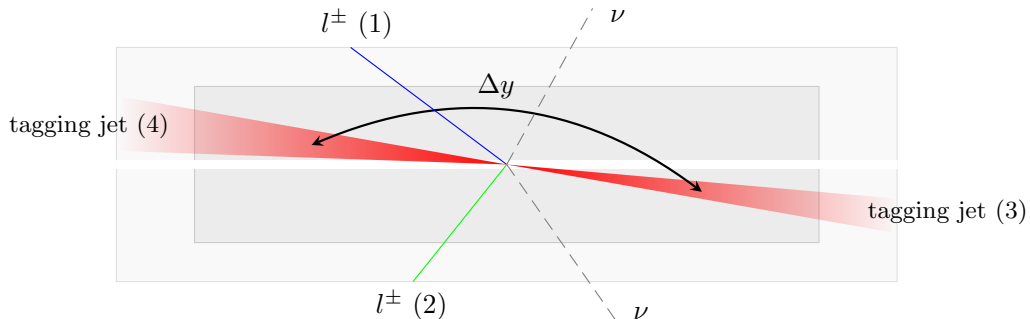


Figure 5.6:  $W^\pm W^\pm jj$  VBS event topology containing two leptons (1 and 2) with the same electric charge, two neutrinos, and two forward tagging jets (3 and 4) with large rapidity separation  $\Delta y$ .

#### 1134 5.0.4 Overview of backgrounds

1135 In addition to QCD production of  $W^\pm W^\pm jj$  events, there are several other processes that can end  
 1136 up with a final state of two same-sign leptons, two neutrinos, and two jets. However, due to the ±2  
 1137 final state charge, there is a considerable reduction in SM backgrounds (such as  $Z$  boson events)  
 1138 when compared to an analysis like opposite-sign  $W^\pm W^\mp jj$ .

1139 One of the largest sources of background involves processes with prompt leptons<sup>10</sup>. These are  
 1140 events that contain two leptons with the same electric charge and one or more additional leptons

<sup>10</sup>Prompt leptons are those that are produced in the primary collision and are a direct decay product of the process of interest. Non-prompt leptons originate from some secondary process, such as a  $b$ -hadron decay, or are jets that get mis-reconstructed as a lepton.

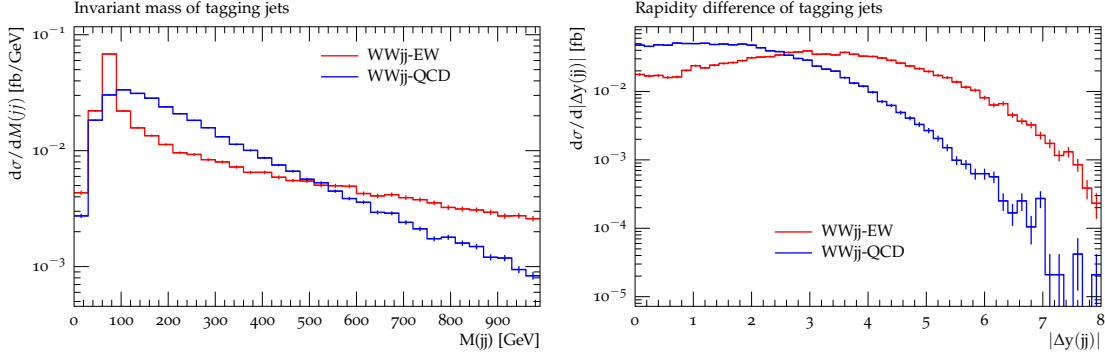


Figure 5.7: Generator level comparisons at  $\sqrt{s} = 8$  TeV of dijet invariant mass ( $m_{jj}$ , left) and dijet rapidity ( $\Delta y_{jj}$ , right) in EWK (red) and QCD (blue)  $W^\pm W^\pm jj$  events. Both data sets have been normalized to the same area. Plots taken from [54].

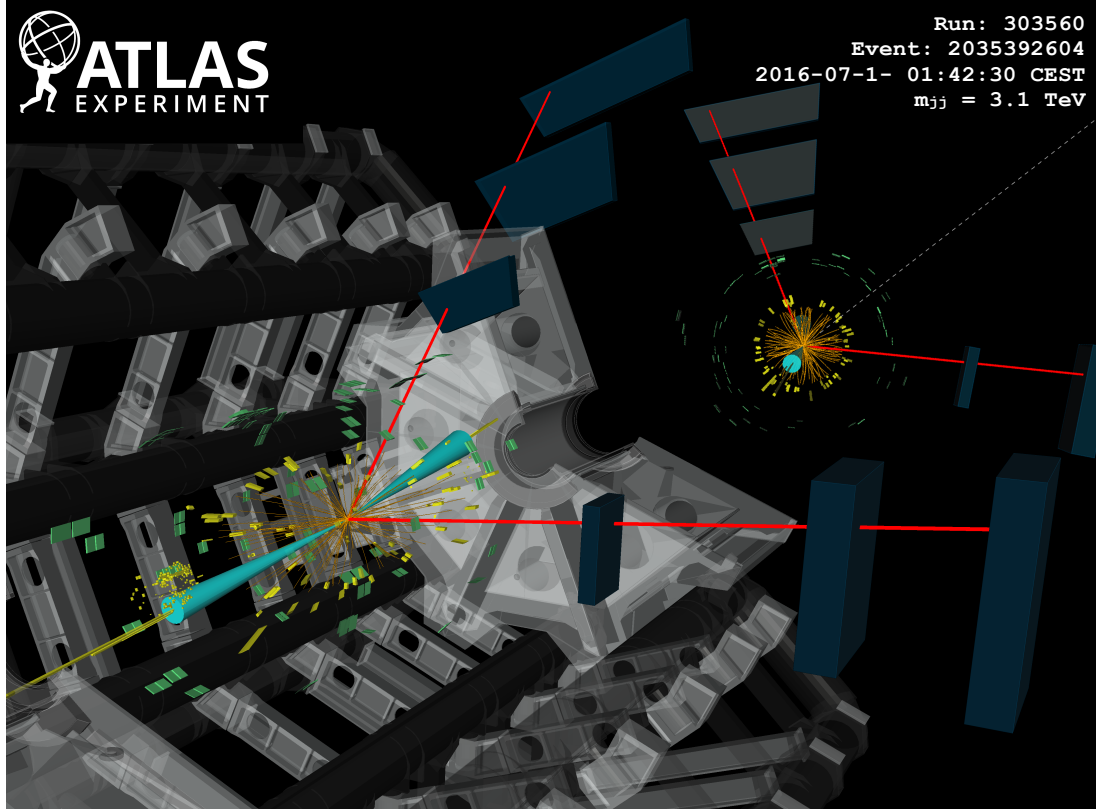


Figure 5.8: ATLAS event display of a  $pp \rightarrow W^\pm W^\pm \rightarrow \mu^\pm \nu_\mu \mu^\pm \nu_\mu jj$  event. The muons are represented by the red lines travelling from the ID through the MS, and the forward jets are represented by the blue cones with yellow energy deposits in the calorimeters. The direction of the  $E_T^{\text{miss}}$  in the transverse plane is indicated by the gray dashed line in the inset image. Event display taken from [45].

that are “lost”, either by failing the selection criteria or falling outside of the detector’s acceptance. The number of processes that can contribute is limited by the requirement of same-sign leptons, and as a result this background is dominated by processes involving two or more vector bosons, with the largest contribution coming from  $WZ$  events and smaller contributions from  $ZZ$  and  $t\bar{t}V$  events. Triboson events where one boson decays hadronically also contribute to this background; however, the jets are generally softer and more central than in a typical VBS event, and the cuts applied on the forward jets suppress these contributions.

The other dominant background comes from non-prompt, or “fake”, leptons. Here one or more leptons originate from the decay of another particle unrelated to the signal process, such as a heavy-flavor decay or photon conversion, or come from a jet that is misidentified as a lepton. This background is mostly made up of events from  $t\bar{t}$  and  $W+\text{jets}$  processes, with a much smaller contribution from  $V\gamma$  events. **TODO: check whether  $V\gamma$  really qualifies as non-prompt, we lump  $Z\gamma$  in with the charge flip background in the paper...**

Finally, opposite-sign lepton pairs can enter the signal region if one of the leptons is reconstructed with the wrong charge (called *charge misidentification*<sup>11</sup>). In practice, this only affects events with electrons, as the charge misidentification rate for muons is negligible [55]. This is a major background in events with two electrons, but is a much smaller contribution for events with one electron and one muon.

## 5.1 Data and Monte Carlo samples

This analysis uses  $36.1 \text{ fb}^{-1}$  of  $\sqrt{s} = 13$  TeV proton-proton collision data recorded by ATLAS during 2015 and 2016. The uncertainty in the combined integrated luminosity is 2.1%. It is derived following a methodology similar to that detailed in [56] and using the LUCID-2 detector for the baseline luminosity measurements [57] from calibration of the luminosity scale using  $x$ - $y$  beam-separation scans.

### 5.1.1 Monte Carlo samples

A number of Monte Carlo (MC) simulations are employed to model signal and background processes. In order to model the real collision data as closely as possible, each MC has been run through a full simulation of the ATLAS detector [58] in GEANT4 [59], and events have been reconstructed

---

<sup>11</sup>Charge misidentification is also referred to interchangeably as *charge mis-ID* and *charge flip*.

1169 using the same algorithms as the data. The simulation reproduces as closely as possible the momentum  
 1170 resolutions and calorimeter responses of the detector, and also includes the effects of pileup by  
 1171 including soft QCD interactions using PYTHIA v8.1 [60]. The MC samples used in this analysis are  
 1172 detailed in this section and summarized in Table 5.2.

1173 The  $W^\pm W^\pm jj$  samples are modeled using SHERPA v2.2.2 [61, 62, 63] with the NNPDF3.0 PDF  
 1174 set [64]. The EWK signal samples are generated by fixing the electroweak coupling constant to  
 1175  $\mathcal{O}(\alpha_W) = 6$ , and a QCD background sample was also generated with  $\mathcal{O}(\alpha_W) = 4$ . SHERPA includes  
 1176 up to one parton at next-to-leading order (NLO) and up to three at leading order (LO) in the  
 1177 strong coupling constant  $\alpha_s$ . A second  $W^\pm W^\pm jj$  EWK sample is generated using POWHEG-BOX  
 1178 v2 [65] with the NNPDF3.0 PDF set and at NLO accuracy. This sample is only used for systematic  
 1179 studies, as POWHEG-BOX does not include resonant triboson contributions in its matrix element, which  
 1180 are non-negligible at NLO [66].

1181 Diboson processes ( $VV$  where  $V = W, Z$ ) are simulated with SHERPA v2.2.2 for mixed hadronic  
 1182 and leptonic decays and SHERPA v2.2.1 for fully leptonic decays of the bosons. Similarly, triboson  
 1183 ( $VVV$ ) and  $V\gamma$  processes are simulated using SHERPA v2.1.1 with up to one parton at NLO and up  
 1184 to three at LO.  $W+jets$  processes are simulated with SHERPA2.2.1 with up to two partons at NLO  
 1185 and four at LO. All the above SHERPA samples use the NNPDF3.0 PDF set and SHERPA's own parton  
 1186 showering. The  $Z+jets$  events are generated with Madgraph5\_aMC@NLO [67] at LO and interfaced  
 1187 with PYTHIA v8.1 for parton showering.

1188  $t\bar{t}$  events are generated using POWHEG-BOX v2 with the CT10 PDF set [68].  $t\bar{t}V$  samples are  
 1189 generated at NLO with Madgraph5\_aMC@NLO and the NNPDF3.0 PDF set interfaced with PYTHIA v8  
 1190 for parton showering. Finally, single top events are generated with POWHEG-BOX v1 and the CT10f4  
 1191 PDF set interfaced with PYTHIA v6 [69] for parton showering.

## 1192 5.2 Object and event selection

1193 This section details the selection criteria for objects used in the analysis as well as the selection for  
 1194 signal events.

### 1195 5.2.1 Object selection

1196 Muons, electrons, and jets all must pass strict selection requirements to ensure that only high quality,  
 1197 well measured objects are used. For leptons, a baseline selection is defined (called the *preselection*),  
 1198 which all leptons must pass in order to be considered for the analysis. This preselection is an

Process	Generator	Comments
$W^\pm W^\pm jj$ (EWK)	SHERPA v2.2.2	Signal sample
$W^\pm W^\pm jj$ (EWK)	POWHEG-BOX v2	Systematics sample
$W^\pm W^\pm jj$ (QCD)	SHERPA v2.2.2	
Diboson	SHERPA v2.2.2	Both bosons decay leptonically ( $llll$ , $lll\nu$ , $ll\nu\nu$ )
Triboson	SHERPA v2.2.1	One boson decays leptonically, the other hadronically
$W + \text{jets}$	SHERPA v2.2.1	
$Z + \text{jets}$	Madgraph5_aMC@NLO	
$V\gamma$	SHERPA v2.1.1	
$V\gamma jj$ (EWK)	SHERPA v2.2.4	
$t\bar{t}V$	Madgraph5_aMC@NLO	
$t\bar{t}$	POWHEG-BOX v2	
Single top	POWHEG-BOX v1	EWK $t$ -, $s$ -, & $Wt$ -channels

Table 5.2: Summary of MC samples used in the analysis.

intentionally loose set of criteria in order to have high acceptance for rejecting backgrounds with additional leptons (i.e.  $WZ \rightarrow 3l\nu jj$ ). Signal leptons are then required to satisfy a much tighter *signal selection* aimed at suppressing backgrounds from non-prompt or fake leptons. A third set of lepton selection criteria, the *loose selection*, defines a sample enriched in non-prompt leptons, and it is used in the fake factor method for estimating the non-prompt background, discussed in detail in Section 5.3.4. Jets are only required to pass one set of selection criteria. These selections are detailed in the following sections and summarized in Table 5.3 for muons, Table 5.4 for electrons, and Table 5.5 for jets.

### 5.2.1.1 Muon candidate selection

Cuts on muon  $p_T$  serve to reject low momentum leptons from background processes and additional collisions from pileup events. Preselected muons must have  $p_T > 6$  GeV and signal muons  $p_T > 27$  GeV. The  $p_T$  requirement for loose muons is lower than for signal muons,  $p_T > 15$  GeV, for reasons that are discussed in Section 5.3.4. Muons are required to fall within the detector's  $\eta$  acceptance:  $|\eta| < 2.7$  for preselected muons, which is tightened to  $|\eta| < 2.5$  for the signal muons.

Cuts on the transverse and longitudinal impact parameters are applied to ensure that the candidate muon originated from the primary particle interaction and not some other source, such as a heavy flavor decay. The preselection and the loose selection both have looser requirements on the transverse impact parameter significance ( $d_0/\sigma_{d_0}$ ) than the signal selection; all three have the same requirement on the transverse impact parameter ( $|z_0 \times \sin \theta|$ ).

Finally, the muon candidates are required to pass a particle identification and an isolation criteria

as defined in [70]. The methods used in constructing the identification and isolation workingpoints are described in more detail in Section 3.2.4.2. The muon identification serves to select prompt muons with high efficiency and well measured momenta. This analysis uses two different workingpoints, **Loose** for preselected muons and **Medium** for loose and signal muons, where **Medium** muons are a tighter subset of those that pass the **Loose** requirement. Muon isolation is a measurement of detector activity around the muon candidate, and it is measured with both track-based and calorimeter-based variables. The isolation workingpoint used for the signal muons, **Gradient**, is defined such that there is 90% or better background rejection efficiency for 25 GeV muons, and 99% efficiency at 60 GeV. There is no minimum isolation requirement for preselected or loose muons. Loose muons are additionally required to fail one or both of the signal transverse impact parameter cut and signal isolation requirement.

Muon preselection	
Momentum cut	$p_T > 6$ GeV
Angular acceptance	$ \eta  < 2.7$
Longitudinal impact parameter	$ z_0 \times \sin \theta  < 0.5$ mm
Transverse impact parameter	$d_0/\sigma_{d_0} < 10$
Particle identification	<b>Loose</b>

Muon signal selection	
Momentum cut	$p_T > 27$ GeV
Angular acceptance	$ \eta  < 2.5$
Longitudinal impact parameter	$ z_0 \times \sin \theta  < 0.5$ mm
Transverse impact parameter	$d_0/\sigma_{d_0} < 3$
Particle identification	<b>Medium</b>
Particle isolation	<b>Gradient</b>

Muon loose selection	
Momentum cut	$p_T > 15$ GeV
Angular acceptance	$ \eta  < 2.5$
Longitudinal impact parameter	$ z_0 \times \sin \theta  < 0.5$ mm
Transverse impact parameter	$d_0/\sigma_{d_0} < 10$
Particle identification	<b>Medium</b>
Fail signal transverse impact parameter and/or isolation cuts	

Table 5.3: Muon selection criteria. All muons are required to pass the preselection (top), and then either the signal (middle) or loose (bottom) criteria is applied to the preselected electrons.

---

1230    **5.2.1.2 Electron candidate selection**

1231    The electron candidate selections are very similar to those for muons. The  $p_T$  cut starts at  $p_T >$   
 1232    6 GeV for the preselection, increases to  $p_T > 20$  GeV for loose electrons, and finally to  $p_T > 27$  GeV  
 1233    for signal electrons. The  $|\eta|$  cut for electrons requires  $|\eta| < 2.47$  for all electrons, with the region  
 1234     $1.37 \leq |\eta| \leq 1.52$  removed from loose and signal electrons. This region is where the electromagnetic  
 1235    calorimeter transitions from the barrel to the endcaps and is not fully instrumented. Both the  
 1236    transverse and longitudinal impact parameter cuts are the same for all electron selections.

1237    The electron particle identification uses a multivariate likelihood technique (LH) [71] detailed  
 1238    in Section 3.2.4.3. Preselected electrons must pass the loosest LH workingpoint `LooseLH` with  
 1239    an additional requirement that there be a reconstructed track hit in the first layer of the pixel  
 1240    detector (a so-called *B*-layer hit). The LH requirement for the loose and signal electrons the tightness  
 1241    of the identification using `MediumLH` and `TightLH`, respectively. As for isolation, the `Gradient`  
 1242    workingpoint is required for signal electrons only. The loose electrons must fail one or both of the  
 1243    signal identification and isolation requirements.

1244    **5.2.1.3 Jet candidate selection**

1245    The final objects that need to pass selection are jets. Jets are clustered using the anti- $k_t$  algo-  
 1246    rithm [72] within a radius of  $\Delta R = 0.4$ . The jets are then calibrated using  $E_T$ - and  $\eta$ -dependent  
 1247    correction factors that are trained using MC simulations [73]. These calibrated jets are then re-  
 1248    quired to have  $p_T > 30$  GeV if they lie in the forward regions of the detector ( $2.4 < |\eta| < 4.5$ ) and  
 1249     $p_T > 25$  GeV in the central region ( $|\eta| \leq 2.4$ ). In order to suppress pileup jets, the so-called jet-  
 1250    vertex-tagger (JVT) discriminant associates a jet with the primary interaction vertex [74]; central  
 1251    jets with  $p_T > 60$  GeV are required to pass the `Medium` JVT workingpoint, which corresponds to  
 1252    an average efficiency of over 92%. Finally, the jets are required to be separated by selected prompt  
 1253    leptons by at least  $\Delta R(j, l) > 0.3$ .

1254    **5.2.1.4 Treatment of overlapping objects**

1255    In the event that one or more objects are reconstructed very close to each other, there is the  
 1256    possibility for double-counting if both originated from the same object. The procedure by which  
 1257    this ambiguity is resolved is called *overlap removal* (OR). The standard ATLAS recommendation  
 1258    for OR is implemented in this analysis [75, 76] and is summarized in Table 5.6.

Electron preselection	
Momentum cut	$p_T > 6$ GeV
Angular acceptance	$ \eta  < 2.47$
Longitudinal impact parameter	$ z_0 \times \sin \theta  < 0.5$ mm
Transverse impact parameter	$d_0/\sigma_{d_0} < 5$
Particle identification	<b>LooseLH + <math>B</math>-layer hit</b>

Electron signal selection	
Momentum cut	$p_T > 27$ GeV
Angular acceptance	$ \eta  < 2.47$ , excluding $1.37 \leq  \eta  \leq 1.52$
Longitudinal impact parameter	$ z_0 \times \sin \theta  < 0.5$ mm
Transverse impact parameter	$d_0/\sigma_{d_0} < 5$
Particle identification	<b>TightLH</b>
Particle isolation	<b>Gradient</b>

Electron loose selection	
Momentum cut	$p_T > 20$ GeV
Angular acceptance	$ \eta  < 2.47$ , excluding $1.37 \leq  \eta  \leq 1.52$
Longitudinal impact parameter	$ z_0 \times \sin \theta  < 0.5$ mm
Transverse impact parameter	$d_0/\sigma_{d_0} < 5$
Particle identification	<b>MediumLH</b>
Fail signal identification and/or isolation cuts	

Table 5.4: Electron selection criteria. All electrons are required to pass the preselection (top), and then either the signal (middle) or loose (bottom) criteria is applied to the preselected electrons.

Jet selection	
Momentum cut	$p_T > 30$ GeV for $2.4 <  \eta  < 4.5$ $p_T > 60$ GeV for $ \eta  < 2.4$
JVT cut	<b>Medium</b>
Jet-lepton separation	$\Delta R(j, l) > 0.3$

Table 5.5: Jet selection criteria. All jets are required to pass the above selection in order to be used in the analysis.

1259 Since electrons leave a shower in the EM calorimeter, every electron has a jet associated with  
 1260 it. Therefore, any jets close to an electron (within  $\Delta R(e, j) < 0.2$ ) are rejected due to the high  
 1261 probability that they are the same object. On the other hand, when jets and electrons overlap  
 1262 within a large radius of  $0.2 < \Delta R(e, j) < 0.4$ , it is likely that the electron and jet both are part of  
 1263 a heavy-flavor decay, and the electron is rejected.

1264 High energy muons can produce photons via bremsstrahlung radiation or collinear final state  
 1265 radiation which results in a nearby energy deposit in the calorimeters. Non-prompt muons from  
 1266 hadronic decays produce a similar signature; however, in this case the jet has a higher track multiplicity  
 1267 in the ID. It is possible to address both cases by rejecting the jet when the ID track multiplicity  
 1268 is less than three and otherwise rejecting the muon for jets and muons within  $\Delta R(\mu, j) < 0.4$ .

1269 In addition to the case above where muon bremsstrahlung results in a nearby reconstructed jet,  
 1270 the ID track from the muon and the calorimeter energy deposit can lead to it being reconstructed  
 1271 as an electron. In this case, if both a muon and an electron share a track in the ID, the muon is  
 1272 kept and the electron is rejected, unless the muon is calorimeter-tagged<sup>12</sup>, in which case the muon  
 1273 is removed in favor of the electron.

Overlap	Check	Result (remove → keep)
Electron & Jet	$\Delta R(e, j) < 0.2$	Jet → electron
	$0.2 < \Delta R(e, j) < 0.4$	Electron → jet
Muon & Jet	$\Delta R(\mu, j) < 0.4$ and Jet $N_{ID}$ tracks $< 3$	Jet → muon
	$\Delta R(\mu, j) < 0.4$ and Jet $N_{ID}$ tracks $\geq 3$	Muon → jet
Electron & Muon	Shared ID track	Electron → muon
	Shared ID track & muon is calo-tagged	Muon → electron

Table 5.6: Summary of the overlap removal procedure used in the analysis. If the criteria in the “check” column is met, in the “result” column, the object on the left of the arrow is removed in favor of the object on the right.

### 1274 5.2.2 Signal event selection

1275 After the objects have been selected, cuts are applied on a per-event level to select  $W^\pm W^\pm jj$  signal  
 1276 events. The event selection is summarized in Table 5.8 and is detailed in this section. It includes  
 1277 the results of an optimization performed using a multidimensional grid scan.

1278 The initial event selection begins by choosing events that pass one or more of the trigger re-  
 1279 quirements listed in Table 5.7. At least one signal lepton is “matched” to a passed trigger in order

<sup>12</sup>A calorimeter-tagged (CT) muon is a muon that is identified by matching an ID track to a calorimeter energy deposit. CT muons have relatively low reconstruction efficiency compared to those measured by the MS, but can be used to recover acceptance in regions of the detector where the MS does not have full coverage [70].

to ensure that it was indeed a signal lepton that fired the trigger. A collection of *event cleaning* cuts must also be passed in order to remove events collected during periods in which one or more components of the detector was not operating optimally. Finally, the events are required to contain at least one interaction vertex. An event can have multiple reconstructed vertices from additional proton-proton collisions that occurred in the same bunch crossing. In this case, the *primary vertex* is determined by choosing the vertex with the largest sum of the  $p_T^2$  of its associated tracks.

	2015 data	2016 data
Electrons	$p_T > 24$ GeV and Medium ID	$p_T > 26$ GeV and Tight ID and Loose isolation
	$p_T > 60$ GeV and Medium ID	$p_T > 60$ GeV and Medium ID
	$p_T > 120$ GeV and Loose ID	$p_T > 140$ GeV and Loose ID
Muons	$p_T > 20$ GeV and Loose isolation $p_T > 50$ GeV	$p_T > 26$ GeV and Medium isolation $p_T > 50$ GeV

Table 5.7: Summary of trigger requirements for electrons and muons for  $\sqrt{s} = 13$  TeV data collected in 2015 and 2016. At least one of the triggers must be satisfied.

Events are then required to contain exactly two signal leptons with the same electric charge. The dilepton pair must have a combined invariant mass of  $m_{ll} \geq 20$  GeV in order to suppress low mass Drell-Yan backgrounds. Two additional selections are applied to events in the  $ee$ -channel: both electrons are required to have  $|\eta| < 1.37$  with an invariant mass at least 15 GeV away from the  $Z$ -boson mass to reduce events where one electron is reconstructed with the wrong charge (this background will be discussed in more detail in Section 5.3.3). To suppress backgrounds from events with more than two leptons, events with more than two leptons passing the preselection are vetoed.

Missing transverse energy ( $E_T^{\text{miss}}$ ) represents any particles that escape the detector without being measured, such as neutrinos, and is defined as the magnitude of the vector sum of transverse momenta of all reconstructed objects. It can be difficult to calculate accurately, as it involves measurements from all subsystems within the detector, and it is sensitive to any corrections that may be applied to the reconstructed physics objects [77]. These corrections, including the momentum smearing for muons, energy scale and smearing for electrons, and jet calibrations, are propagated to the  $E_T^{\text{miss}}$  calculation. Events are required to contain  $E_T^{\text{miss}} > 30$  GeV in order to account for the two neutrinos from the  $W$  boson decays.

At least two jets are required. The leading and subleading jets must have  $p_T > 65$  GeV and  $p_T > 35$  GeV, respectively, and are referred to as the *tagging jets*. Events are vetoed if they contain one or more jets that have been tagged as a  $b$ -jet to suppress backgrounds from heavy flavor decays (especially top quark events). The  $b$ -tagging algorithm used by ATLAS is a boosted decision tree

1305 (BDT) called MV2c10, and this analysis uses a workingpoint with 85% efficiency [78].

1306 Finally, cuts are applied on the VBS signature outlined in Section 5.0.3. The tagging jets are  
 1307 required to have a dijet invariant mass  $m_{jj} > 200$  GeV and be separated in rapidity by  $|\Delta y_{jj}| > 2.0$ .  
 1308 This preferentially selects the VBS EWK events over the QCD-produced  $W^\pm W^\pm jj$  events.

Event selection	
Event preselection	Pass at least one trigger with a matched lepton Pass event cleaning At least one reconstructed vertex
Lepton selection	Exactly two leptons passing signal selection Both signal leptons with the same electric charge $ \eta  < 1.37$ and $ M_{ee} - M_Z  > 15$ GeV ( $ee$ -channel only) Veto events with more than two preselected leptons
Missing transverse energy	$E_T^{\text{miss}} \geq 30$ GeV
Jet selection	At least two jets Leading jet $p_T > 65$ GeV Subleading jet $p_T > 35$ GeV $m_{jj} > 200$ GeV $N_{b\text{-jet}} = 0$ $ \Delta y_{jj}  > 2.0$

Table 5.8: The signal event selection.

### 1309 5.3 Background estimations

1310 The major sources of background events are summarized in Section 5.0.4, and the methods used to  
 1311 estimate them are detailed in this section. Prompt backgrounds from  $ZZ$  and  $t\bar{t}V$  are estimated  
 1312 directly from MC simulations. The shape of the  $WZ$  and  $V\gamma$  backgrounds are taken from MC, and  
 1313 the predicted yeilds are normalized to the data predictions in dedicated control regions, as outlined  
 1314 in Sections 5.3.1 and 5.3.2, respectively. Opposite sign events with a charge misidentified electron  
 1315 are estimated by a data-driven background method which is summarized in Section 5.3.3. Finally, a  
 1316 *fake factor* method is used to estimate the contributions from non-prompt backgrounds and is the  
 1317 subject of Section 5.3.4.

#### 1318 5.3.1 Estimation of the $WZ$ background

1319 The dominant background involving prompt leptons comes from  $WZ + \text{jets}$  events. The contribution  
 1320 is estimated from MC simulation and normalized to data in a control region enriched in  $WZ$  events

defined by the same event selection as Table 5.8 for the signal region, with the following changes applied to increase the purity of the  $WZ$  process:

- The third lepton veto is inverted, requiring a third lepton with  $p_T > 15$  GeV
- Two of the leptons must make a same-flavor opposite-sign pair. If more than one pair exists, the one with  $m_{ll}$  closest to the  $Z$  boson mass is chosen.
- The trilepton invariant mass is required to be  $m_{lll} > 106$  GeV to reduce contributions from  $Z\gamma$  and  $Z+jets$

Once the event yields in the control region are calculated, they are propagated to the final signal region fit, detailed in Section 5.4.1, in a single bin combining all the lepton channels. The systematic uncertainties of the  $WZ$  background are also calculated at this time. The event yields for the  $WZ$  control region are listed in Table 5.9, and distributions of the leading lepton  $p_T$  and  $\eta$  as well as trilepton invariant mass  $m_{lll}$  are found in Figures 5.10 and 5.9, respectively.

Event yields in the $WZ$ control region	
$WZ$	$197.9 \pm 1.4$
$ZZ$	$14.1 \pm 0.3$
Triboson	$1.26 \pm 0.1$
top	$10.8 \pm 1.1$
$Z\gamma$	$3.1 \pm 1.1$
$Z+jets$	$2.5 \pm 1.4$
Total prediction	$229.7 \pm 2.5$
Data	$201 \pm 14.2$

Table 5.9: Event yields in the  $WZ$  control region before normalization. All lepton flavor channels are combined.

### 5.3.2 Estimation of the $V\gamma$ background

Events from  $V\gamma$  processes can pass selection if the photon converts into an  $e^+e^-$  pair and one of the electrons passes the selection criteria. The background is estimated from MC simulations which are then scaled by a normalization factor calculated from a control region enriched in  $Z(\mu^+\mu^-)\gamma$  events. This control region selects two opposite-sign muons and an additional electron that is assumed to come from the photon conversion. The full event selection is detailed in Table 5.10.

The  $Z\gamma$  MC samples available do not cover the full range of  $p_T^\gamma$  and  $\Delta R(\gamma, l)$ ; thus, additional Drell-Yan samples ( $Z+jets$ ) are used to fill out the phase space. Overlap between the two samples

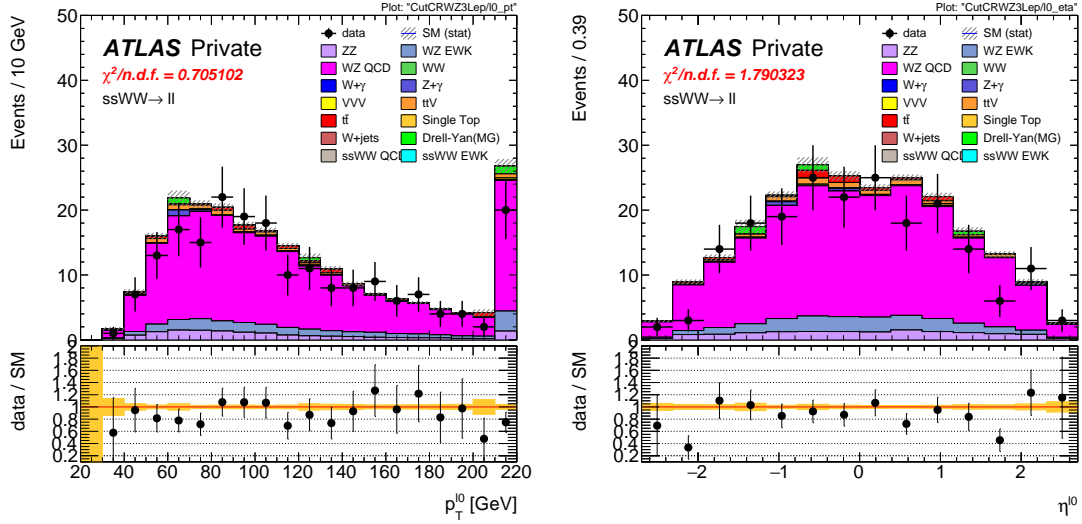


Figure 5.9: Leading lepton  $p_T$  (left) and  $\eta$  (right) distributions in the  $WZ$  control region before normalization. All lepton channels are combined.

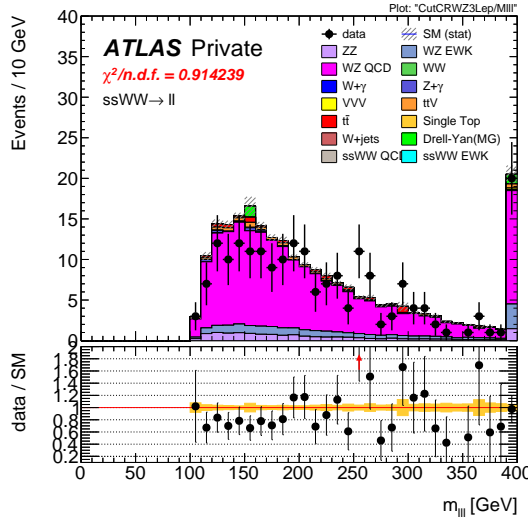


Figure 5.10: Trilepton invariant mass  $m_{lll}$  distribution in the  $WZ$  control region before normalization. All lepton channels are combined.

$V\gamma$ control region
Exactly two muons with $p_T > 27$ GeV and $p_T > 20$ GeV
Exactly one additional electron with $p_T > 15$ GeV
Remove overlap between $Z+jets$ and $Z\gamma$
Di-muon + photon invariant mass $75 < M_{\mu\mu\gamma} < 100$ GeV
$E_T^{\text{miss}} < 30$ GeV

Table 5.10: Selection criteria for the  $V\gamma$  control region.

1341 are removed based to avoid double counting. Events with final state photons at truth level are  
 1342 checked to ensure that the photon did not originate from a hadronic decay. Cuts on  $p_T^\gamma > 10$  GeV  
 1343 and  $\Delta R(\gamma, l) > 0.1$  are then applied at generator level, and  $Z\gamma$  events that fail and  $Z+jets$  events  
 1344 that pass this additional selection are removed.

1345 The normalization factor is calculated directly from the event yields in the  $V\gamma$  control region  
 1346 rather than in the signal fit, as is done for the  $WZ$  background. The event yields are listed in  
 1347 Table 5.11, and the normalization factor is determined to be 1.77. No MC events from  $Z\gamma$  processes  
 1348 survive the full event selection; thus, the scaling is only applied to the  $W\gamma$  background in the signal  
 1349 region. A systematic uncertainty of 44% is assigned to the background based off of the uncertainties  
 1350 in the calculation of the normalization factor.

Event yields in the $V\gamma$ control region	
$Z\gamma$	$24.6 \pm 3.3$
$Z+jets$	$3.0 \pm 1.5$
diboson + triboson	$6.7 \pm 0.3$
top	$1.5 \pm 0.5$
Total prediction	$35.8 \pm 3.7$
Data	$57 \pm 7.6$

Table 5.11: Event yields in the  $V\gamma$  control region. The  $V\gamma$  scale factor of 1.77 is calculated by scaling up the  $Z\gamma$  and  $Z+jets$  backgrounds to account for the difference between the data and predicted total background.

### 1351 5.3.3 Estimation of backgrounds from charge misidentification

1352 If an electron's charge is mis-reconstructed, it can lead to a real, opposite-sign lepton pair passing  
 1353 the same-sign requirement in the event selection. There are two primary reasons this can occur:

- 1354 1. An electron emits a photon via bremsstrahlung which then converts into an electron-positron  
 1355 pair, and the conversion track with the wrong electric charge is matched to the original electron.  
 1356 This is the dominant process leading to charge flip, and it is highly dependent on the electron  
 1357  $\eta$  due to the different amount of detector material the electron passes through.
- 1358 2. The curvature of the electron's track is mismeasured, resulting in the wrong charge being  
 1359 assigned. This process is dependent on the momentum of the electron, as its track becomes  
 1360 more straight as the momentum of the electron increases.

1361 In order to estimate this background, the rate at which an electron's charge is misidentified is  
 1362 calculated from  $Z \rightarrow e^+e^-$  MC simulation. It is known that the MC does not perfectly model

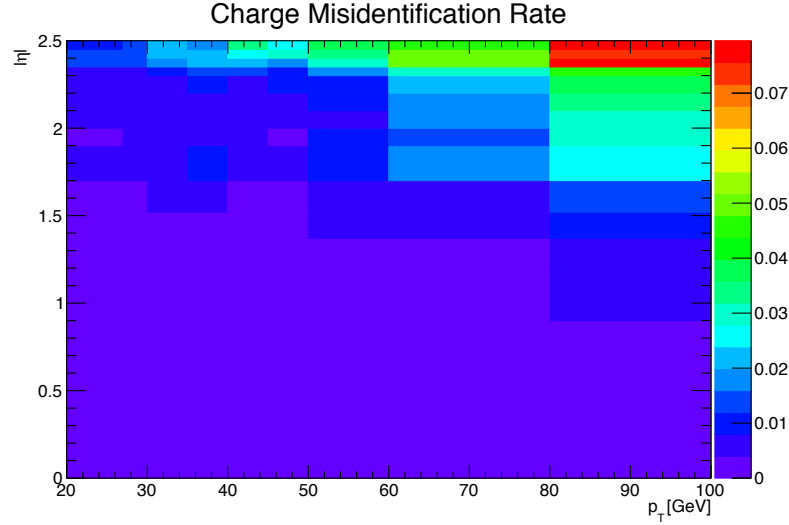


Figure 5.11: Charge misidentification rates for electrons as a function of  $|\eta|$  and  $p_T$ . Rates are calculated from  $Z \rightarrow e^+e^-$  MC after applying scale factors to approximate the charge mis-ID rates in data.

the material effects leading to charge flip; as a result, scale factors are applied to the MC in order for it to better reflect the real performance. These scale factors are obtained from the ratio of charge mis-ID rates in data and uncorrected MC in [47] following the method outlined in [79]. Once the scale factors are applied, the charge misidentification rate  $\varepsilon$  can be extracted by comparing the electron's reconstructed charge with the charge of its truth particle:

$$\varepsilon(\eta, p_T) = \frac{N_{\text{wrong charge}}}{N_{\text{prompt electrons}}} \quad (5.1)$$

The charge mis-ID rate is calculated in bins of electron  $|\eta|$  and  $p_T$  and varies from below 0.1% in the

central region of the detector up to 8% in the forward regions for high  $p_T$  (above 90 GeV) electrons.

A two-dimensional plot of  $\varepsilon$  can be found in Figure 5.11.

Given the charge flip rate  $\varepsilon(\eta, p_T)$ , the rate at which an electron has its charge correctly reconstructed is  $(1 - \varepsilon)$ . Thus there are three possible combinations of charge identification, assuming a two-electron event:

- 1374 1. Both electrons are reconstructed correctly:  $(1 - \varepsilon)^2$
- 1375 2. Both electrons are mis-reconstructed:  $\varepsilon^2$
- 1376 3. Only one electron is mis-reconstructed:  $2\varepsilon(1 - \varepsilon)$

1377 In order to estimate the size of the background from charge misidentification, opposite-sign events  
 1378 are selected using the default event selection for a given signal or control region with the same-sign  
 1379 requirement inverted. These events are then weighted by the probability for one of the electrons to  
 1380 be reconstructed with the wrong charge:

$$\omega = \frac{\varepsilon_1(1 - \varepsilon_2) + \varepsilon_2(1 - \varepsilon_1)}{(1 - \varepsilon_1)(1 - \varepsilon_2) + \varepsilon_1\varepsilon_2} \quad (5.2)$$

1381 where the subscripts 1 and 2 refer to the leading and subleading electrons, respectively, and  $\varepsilon_i$  is a  
 1382 function of the  $\eta$  and  $p_T$  of the  $i^{\text{th}}$  electron. In the case of an event with only one electron and one  
 1383 muon, Equation 5.2 simplifies:

$$\omega = \frac{\varepsilon}{1 - \varepsilon} \quad (5.3)$$

1384 This method assumes that there is little contamination from fake electrons in the opposite-sign  
 1385 sample, and this has been verified with MC simulation.

1386 Additionally, charge-flipped electrons tend to be reconstructed with lower energy when compared  
 1387 to electrons with the correct charge. This is due to energy loss from the material interactions that  
 1388 can cause the charge to be misidentified. A correction factor is calculated from MC simulations,  
 1389 comparing the  $p_T$  of the truth electron to its reconstructed counterpart:

$$\alpha = \frac{\left(\frac{p_T^{\text{reco}}}{p_T^{\text{truth}}} - 1\right)_{\text{correct charge}}}{\left(\frac{p_T^{\text{reco}}}{p_T^{\text{truth}}} - 1\right)_{\text{wrong charge}}} \quad (5.4)$$

1390 The correction is then applied to the  $p_T$  of the charge-flipped electron via

$$p_T = p_T^0 / (1 + \alpha) + dE \quad (5.5)$$

1391 where  $p_T^0$  is the uncorrected  $p_T$  of the electron and  $dE$  is a gaussian smearing factor centered at  
 1392 zero with a width related to the energy resolution. Since which electron is misreconstructed is never  
 1393 determined in this method, in the case of a two-electron event, the energy correction is applied  
 1394 randomly to one of the two electrons based on the probabilities for them to be charge-flipped. This  
 1395 also determines the overall sign of the event; the charge of the electron that does not receive the  
 1396 correction is taken to be the charge for both.

1397 Systematic uncertainties on the charge mis-ID rates are calculated by generating two additional  
 1398 sets of rates with the uncertainties on the scale factors varied up and down. The size of the esti-  
 1399 mated charge flip background without the energy correction applied is also taken as a systematic  
 1400 uncertainty. These systematic uncertainties are estimated to be approximately  $\pm 15\%$ .

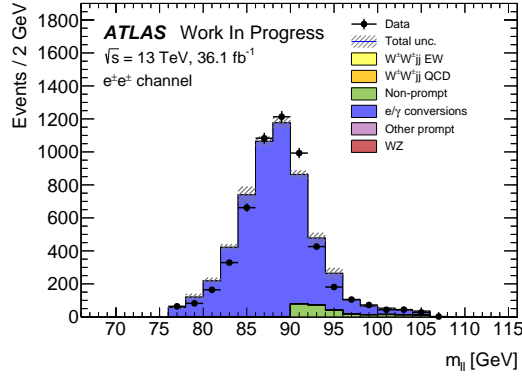


Figure 5.12: Dilepton invariant mass distribution  $m_{ll}$  for the  $ee$  channel in the same-sign inclusive VR.

#### 1401 5.3.3.1 Validation of the charge misidentification estimate

1402 The performance of the charge misidentification estimation is tested in the same-sign inclusive  
1403 validation region (VR), defined in Table 5.12. For  $ee$  events, the mass of the dilepton pair is required  
1404 to lie within 15 GeV of the  $Z$  boson mass to increase the purity of the charge flip background.  
1405  $t\bar{t}$  production, which can contribute to both the charge mis-ID and fake lepton backgrounds, is  
1406 suppressed by the  $b$ -jet veto. The di-electron invariant mass is shown in Figure 5.12, and distributions  
1407 of the leading and subleading electron  $p_T$  in the  $ee$ -channel are shown in Figure 5.13 with the  $Z$   
1408 mass cut inverted. Agreement between data and prediction is seen within the total statistical and  
1409 systematic uncertainties in the VR.

Same-sign inclusive VR
Exactly 2 same-sign signal leptons
$p_T > 27$ GeV for both leptons
$m_{ll} > 20$ GeV
$ m_{ee} - m_Z  > 15$ GeV ( $e^\pm e^\pm$ -channel only)
$N_{b\text{-jet}} = 0$

Table 5.12: Selection criteria for the same-sign inclusive validation region.

#### 1410 5.3.4 Estimation of non-prompt backgrounds with the fake factor method

1411 Events with one prompt lepton produced in association with hadronic jets can pass the event selection  
1412 if a jet is misidentified as a charged lepton or if a non-prompt lepton from the decay of a heavy  
1413 flavor particle (such as  $b$ - and  $c$ -hadrons) passes the signal lepton criteria. These misidentified jets

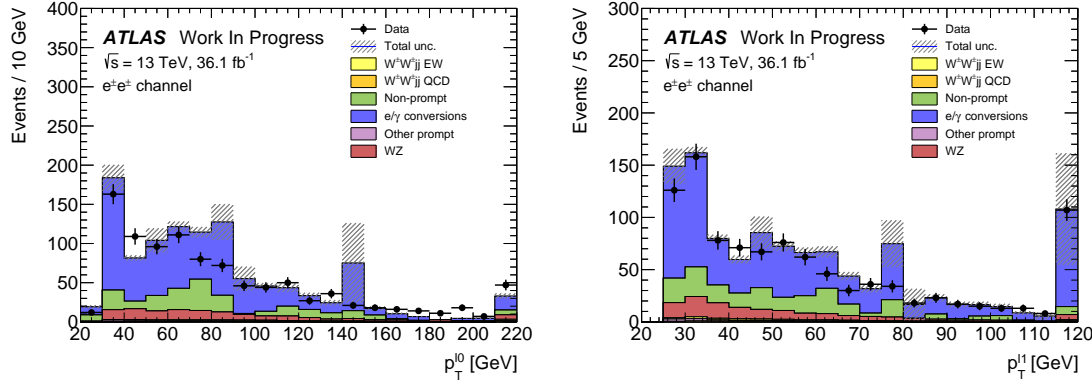


Figure 5.13:  $p_T$  distributions for the leading (left) and subleading (right) electron for the  $ee$  channel in the same-sign inclusive VR. In these plots, the cut requiring  $m_{ee}$  to fall within the  $Z$  mass window has been inverted in order to test the modelling away from the  $Z$  peak.

and non-prompt leptons are collectively referred to as *fake leptons*, or simply *fakes*. The rate at which a fake lepton is misidentified is generally not modelled well enough by the MC to accurately estimate their contributions directly from simulation. Therefore, a data-driven technique called the *fake factor* is used to estimate the size and shape of background processes from fake leptons. In this analysis, a new modification to the fake factor is used involving the particle isolation variables; the method is outlined in the context of the *default* fake factor in Section 5.3.4.1, and the modified fake factor is outlined in Section 5.3.4.2.

#### 5.3.4.1 Overview of the default fake factor method

The goal of the fake factor method is to measure the fake rate from real collision events in a region enriched in fake leptons and use it to estimate the size of the fake lepton background in a chosen signal or control region. This is done by creating two samples using different lepton definitions:

1. The *nominal* sample is made up of leptons passing the signal selection.
2. The *loose* sample is made up of leptons that fail the signal selection while still passing a loosened set of criteria. This sample is enriched in fake leptons and is orthogonal to the set of signal leptons.

Using the sets of nominal and loose leptons, a fake factor  $f$  can be calculated in a region enriched in processes that are prone to producing fake leptons:

$$f = \frac{N_{\text{nominal}}}{N_{\text{loose}}} \quad (5.6)$$

1431 Since the fake rate is not expected to be constant over the entire phase space, the fake factor can  
 1432 be divided into bins:

$$f(b) = \frac{N_{\text{nominal}}(b)}{N_{\text{loose}}(b)} \quad (5.7)$$

1433 where  $b$  represents the bin number. In this analysis, the fake factor is binned in lepton  $p_T$ .

1434 In order to estimate the fake background contribution in a given signal or control region, the  
 1435 fake factor is applied to a second control region with a selection identical to the region of interest  
 1436 with one of the leptons required to satisfy the loose criteria. The region for which the background  
 1437 is estimated contains two nominal leptons and is referred to as *nominal+nominal* (*NN*), and the  
 1438 associated control region where the fake factor is applied contains one nominal and one loose lepton  
 1439 and is referred to as *nominal+loose* (*NL*). The fake background in a *NN* region can then be  
 1440 calculated as:

$$N_{NN}^{\text{fake bkg.}} = \sum_b f(b) N_{NL}(b) \quad (5.8)$$

1441 Backgrounds containing two prompt leptons can also enter the *NL* region if one of the leptons  
 1442 passes the nominal selection and the other passes the loose selection. Since the fake factor method  
 1443 estimates the fake background by scaling the amount of non-prompt events in the *NL* region, if these  
 1444 prompt contributions are not removed, they will be included in the scaling and the background  
 1445 will be overpredicted. The final estimate of the fake background becomes:

$$N_{NN}^{\text{fake bkg.}} = \sum_b f(b) (N_{NL}(b) - N_{NL}^{\text{prompt}}(b)) \quad (5.9)$$

#### 1446 5.3.4.2 The fake factor with $p_T^{\text{cone}}$

1447 When a jet produces a non-prompt lepton, that lepton only carries a fraction of the underlying jet's  
 1448 total momentum. Due to the isolation cut applied to the nominal leptons, they typically carry a  
 1449 much larger percentage of the underlying jet momentum<sup>13</sup> than the loose leptons (which are allowed  
 1450 to fail this criteria).

1451 This discrepancy in the underlying jet momentum fraction can cause problems in the calculation  
 1452 of the fake factor  $f$ . Consider the case where two separate events have jets of identical momentum,  
 1453 but one produces a non-prompt lepton that passes the nominal selection, and the other produces a  
 1454 non-prompt lepton that passes the loose selection. The loose lepton on average will have lower  $p_T$   
 1455 than the nominal lepton despite both originating from jets with the same momentum. This can be

---

<sup>13</sup>Since the isolation variables are a measure of detector activity around the lepton, if other nearby particles carried a significant portion of the jet's momentum, the lepton would likely fail this cut.

1456 seen explicitly when comparing the  $p_T$  of a muon to its associated truth jet:

$$\Delta p_T(\mu, j) = \frac{p_T(j) - p_T(\mu)}{p_T(j) + p_T(\mu)} \quad (5.10)$$

1457 Since muons are not included in the jet reconstruction algorithm,  $\Delta p_T$  approximates the momentum  
 1458 of the muon compared to the rest of the jet. For muons that carry more than 50% of the jet's  
 1459 momentum,  $\Delta p_T$  will be negative and vice-versa. The  $\Delta p_T$  distributions for nominal and loose  
 1460 muons in  $t\bar{t}$  MC events is shown Figure 5.14, where a 50 GeV jet on average corresponds to a  
 1461 35 GeV nominal muon and a 20 GeV loose muon<sup>14</sup>.

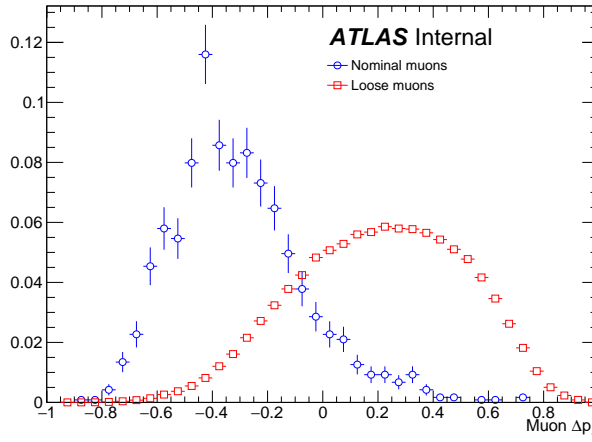


Figure 5.14:  $\Delta p_T$  distributions for nominal (blue) and loose (red) muons in simulated  $t\bar{t}$  events. Each muon has been matched to a truth-level jet. Both distributions are normalized to unit area.

1462 Since the default fake factor defined in Equation 5.7 is binned in lepton  $p_T$ , within a given bin,  
 1463 the underlying jet  $p_T$  spectrum can differ substantially between the numerator and the denominator.  
 1464 Additionally, these differences can vary depending on the process producing the non-prompt leptons  
 1465 or on the specific kinematic selections of the signal or control regions where the fake factor is applied.

1466 Fortunately, the majority of the jet momentum not carried by the non-prompt lepton (excluding  
 1467 neutrinos) can be recovered using isolation variables. A track-based isolation is chosen, referred to  
 1468 as  $p_T^{\text{cone}}$ , and it contains the sum of the  $p_T$  of all particle tracks originating from the primary vertex  
 1469 within a cone of  $\Delta R < 0.3$  around the lepton. Thus, the sample of loose leptons in the denominator  
 1470 of the fake factor calculation is binned in  $p_T + p_T^{\text{cone}}$  rather than simply lepton  $p_T$ . Adding the

<sup>14</sup>To better illustrate the point, here the muon is added back into the jet  $p_T$ , and the corresponding muon  $p_T$  is obtained via  $\Delta p_T(\mu, j) = \frac{(p_T(j) - p_T\mu) - p_T(\mu)}{(p_T(j) - p_T\mu) + p_T(\mu)} = \frac{p_T(j) - 2p_T(\mu)}{p_T(j)}$ .

isolation cone greatly reduces the difference in the fraction of the underlying jet momentum carried by the nominal and loose leptons. To check this, a new  $\Delta p_T$  is calculated between a lepton and its matched truth jet, where the truth jet  $p_T$  has been corrected to include all muons within a cone of  $\Delta R < 0.4$ :

$$p_T(j) = p_T(j_{\text{truth}}) + \sum_{\Delta R < 0.4} p_T(\mu_{\text{truth}}) \quad (5.11)$$

The  $\Delta p_T$  distributions comparing  $p_T$  and  $p_T + p_T^{\text{cone}}$  for nominal and loose leptons using the corrected jet  $p_T$  are found in Figure 5.15, and better agreement is seen between the numerator (nominal) and denominator (loose with  $p_T + p_T^{\text{cone}}$ ) distributions.

The numerator remains binned in lepton  $p_T$ , due to the fact that it is meant to mirror the signal region as closely as possible, and the signal lepton selection does not use  $p_T + p_T^{\text{cone}}$ . The impact of this is expected to be negligible due to the  $p_T^{\text{cone}}$  isolation being small for signal leptons, as shown for muons in Figure 5.16. Finally, the fake factor  $f$  becomes:

$$f(b) = \frac{N_{\text{nominal}}(b(p_T))}{N_{\text{loose}}(b(p_T + p_T^{\text{cone}}))} \quad (5.12)$$

#### 5.3.4.3 Application of the fake factor

The fake factor itself is measured from a sample of events passing a dijet selection requiring exactly one lepton (either passing the nominal or loose selections) and at least one jet. The leading jet must also be  $b$ -tagged and approximately back-to-back with the lepton in order to enhance non-prompt lepton contributions while reducing contributions from processes involving  $W$  and  $Z$  bosons.  $W$  boson events are further suppressed by requiring the sum of the  $E_T^{\text{miss}}$  and the transverse mass of the lepton and  $E_T^{\text{miss}}$  to be less than 50 GeV. The full event selection for the dijet region is summarized in Table 5.13.

The numerator sample is constructed from dijet events in which the lepton passes the nominal (signal) selection and is binned in the lepton  $p_T$ . Similarly, the denominator sample is made up of the remaining dijet events where the lepton passes the loose selection and is binned in the lepton  $p_T + p_T^{\text{cone}}$ . The nominal and loose leptons pass the signal selection<sup>15</sup> and loose selection, respectively, defined earlier in Table 5.3 for muons and Table 5.4 for electrons. Backgrounds from  $W + \text{jets}$ ,  $Z + \text{jets}$ ,  $t\bar{t}$ , and single top processes are estimated from MC simulations requiring one lepton to be prompt using the truth information; these contributions are subtracted from the dijet data. The fake factor

---

<sup>15</sup>The  $p_T > 27$  GeV cut in the signal lepton selection is dropped in favor of the  $p_T > 15$  GeV requirement in the dijet selection.

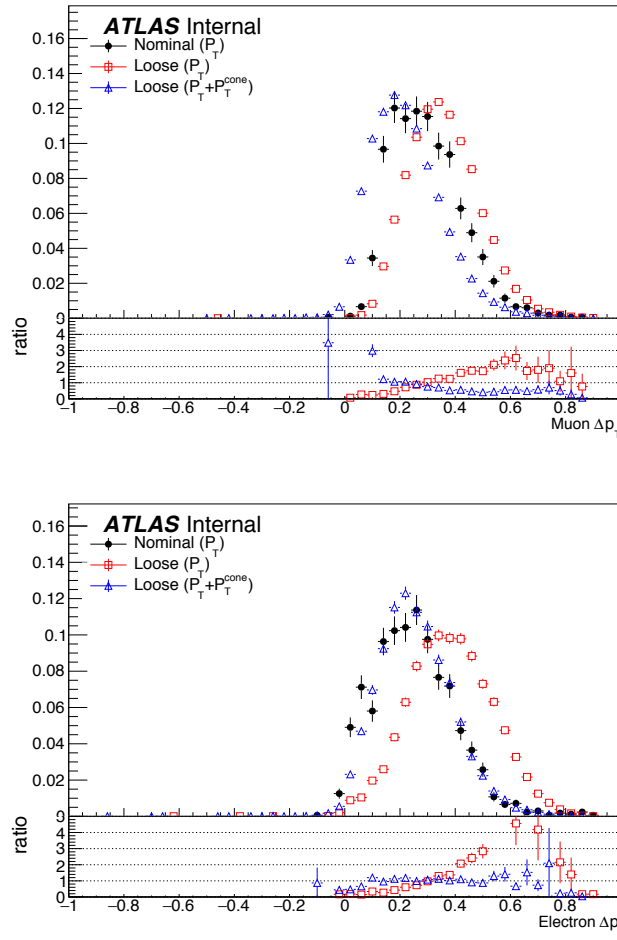


Figure 5.15:  $\Delta p_T$  distributions for muons (top) and electrons (bottom) in simulated  $t\bar{t}$  events. Each lepton has been matched to a truth-level jet, and that truth jet has had its  $p_T$  corrected to include all truth muons within a cone of  $\Delta R < 0.4$ . The nominal leptons are in black.  $\Delta p_T$  is calculated for the loose leptons using  $p_T$  (red) and  $p_T + p_T^{\text{cone}}$  (blue).

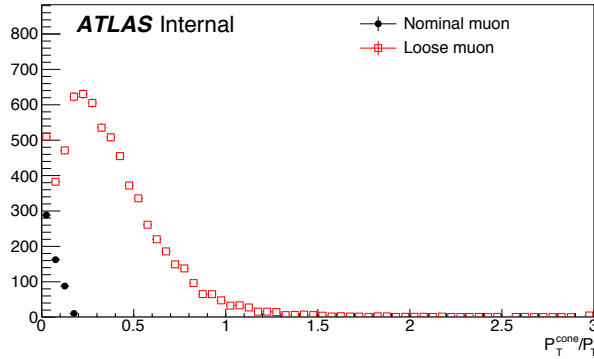


Figure 5.16: Distributions of  $p_T^{\text{cone}}/p_T$  for nominal (black) and loose (red) muons in simulated  $t\bar{t}$  events.

Dijet event selection	
Event preselection	
Exactly one lepton with $p_T > 15$ GeV	
$N_{\text{jet}} > 0$	
Leading jet is $b$ -tagged	
$p_T^{\text{lead. jet}} > 25$ GeV	
$p_T^{\text{lead. jet}} > 30$ GeV if $ \eta_j  > 2.5$	
$ \Delta\phi(l, \text{lead. jet})  > 2.8$	
$m_T(l, E_T^{\text{miss}}) + E_T^{\text{miss}} < 50$ GeV	

Table 5.13: Event selection for the dijet region used for calculating the fake factor. The selected lepton can pass either the nominal (signal) or loose selections. In the case of the nominal leptons, the  $p_T > 27$  GeV requirement is replaced with  $p_T > 15$  GeV.

1497 is then calculated using Equation 5.12 for muons and for central and forward electrons separately.  
 1498 The muon fake factor is shown in Figure 5.17, and the two electron fake factors are shown in  
 1499 Figure 5.18. The numerical values of the fake factors, including their systematic uncertainties which  
 1500 will be discussed in Section 5.3.4.4, are listed in Table 5.14.

1501 In order to properly account for the denominator being binned in  $p_T + p_T^{\text{cone}}$ , special care needs  
 1502 to be taken when estimating the fake background from the  $NL$  regions. For the purposes of the  
 1503 fake factor calculation, it is perhaps more intuitive to consider a loose *object* with  $p_T = p_T + p_T^{\text{cone}}$   
 1504 instead of simply a loose *lepton*, as the lepton and the underlying jet are treated as a whole with this  
 1505 method. When the lepton  $p_T$  cuts required by a particular signal or control region are applied to  
 1506 nominal and loose leptons, the cut is applied to the  $p_T$  of the nominal lepton and to the  $p_T + p_T^{\text{cone}}$   
 1507 of the loose object. Similarly, when looking up the fake factor weight for a given  $NL$  event, the  
 1508 value taken from the bin corresponding to the  $p_T + p_T^{\text{cone}}$  of the loose object. Finally, when applying

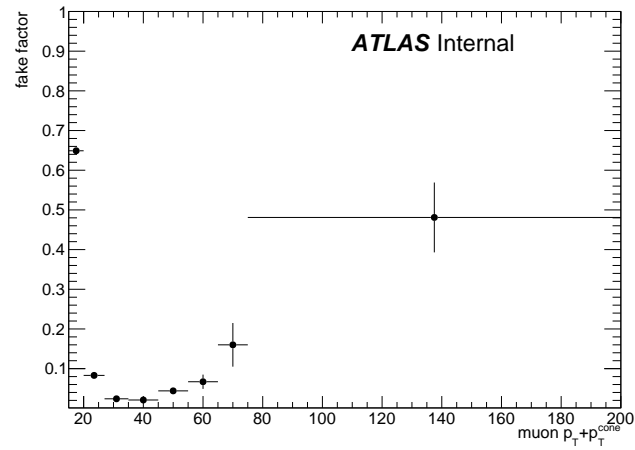


Figure 5.17: The measured fake factor as a function of muon  $p_T + p_T^{\text{cone}}$ . The error bars represent the statistical uncertainty only.

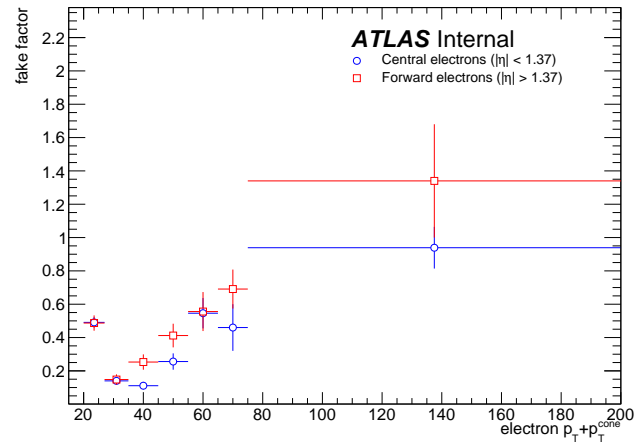


Figure 5.18: The measured fake factor as a function of electron  $p_T + p_T^{\text{cone}}$  in the central ( $|\eta| < 1.37$ , blue) and forward ( $|\eta| > 1.37$ , red) regions of the detector. The error bars represent the statistical uncertainty only.

1509 the weight to the event,  $p_T + p_T^{\text{cone}}$  is assigned as the  $p_T$  of the loose object. Figure 5.19 contains a  
 1510 graphical representation of this procedure.

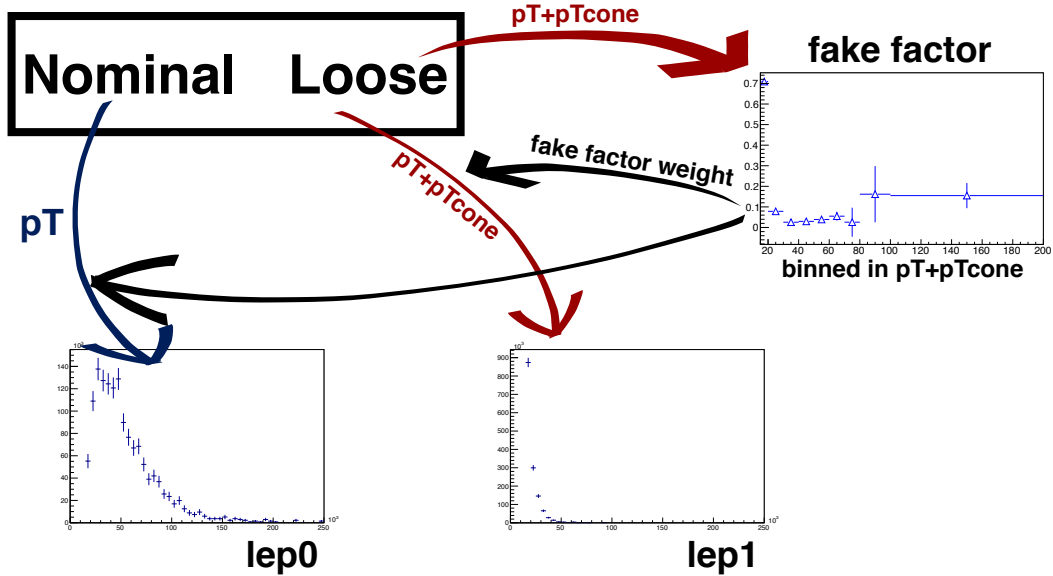


Figure 5.19: Graphical representation of the fake factor application using  $p_T + p_T^{\text{cone}}$ . The value of  $p_T + p_T^{\text{cone}}$  for the loose lepton is used to “look up” the fake factor weight which is then applied to the event. The loose lepton’s  $p_T$  becomes  $p_T + p_T^{\text{cone}}$  for the purpose of the fake background estimation.

1511 Finally, it should be noted that the addition of  $p_T^{\text{cone}}$  to the loose object may cause the loose  
 1512 leptons in the denominator sample to migrate into higher bins. This results in an overall decrease in  
 1513 the number of loose objects in the lower  $p_T + p_T^{\text{cone}}$  bins due to there not being additional leptons at  
 1514 lower  $p_T$  to replace them. Since the fake factor is a ratio of the number of events in a bin, this effect  
 1515 causes the first few bins of the fake factor to increase, as can be seen clearly in Figure 5.17. However,  
 1516 the signal and control regions (and their corresponding  $NL$  regions) contain a  $p_T > 27$  GeV cut that  
 1517 prevents these migrations from negatively impacting the fake estimation.

#### 1518 5.3.4.4 Systematic uncertainties

1519 Four sources of systematic uncertainty are considered: the dijet event selection, the prompt back-  
 1520 ground subtraction, the jet flavor composition, and residual dependence on the underlying jet  $p_T$   
 1521 spectrum. In order to measure the impact of these systematics, new fake factors are computed  
 1522 with each of the systematic variations and the differences from the nominal values are taken as the  
 1523 uncertainty.

- 1524 1. In order to estimate uncertainties due to the dijet selection, the cut on  $M_T + E_T^{\text{miss}}$  is varied  
 1525 by  $\pm 5$  GeV,  $\Delta\phi(l, j)$  by  $\pm 0.1$ , and the jet  $p_T$  cut by  $+5$  GeV.
- 1526 2. To estimate the systematic uncertainty on the prompt background subtraction, the MC pre-  
 1527 diction in a  $W+\text{jets}$  control region is compared to data. The discrepancy between data and  
 1528 MC is found to be approximately 10% [47]. Therefore, the prompt background used for the  
 1529 subtraction is scaled up and down by  $\pm 10\%$ .
- 1530 3. The difference in the jet flavor composition between the dijet events and the events in the  
 1531  $NL$  regions can affect the accuracy of the fake background estimation. The dijet sample is  
 1532 dominated by light jets, while the  $NL$  regions tend to be dominated by heavy flavor from  $t\bar{t}$ .  
 1533 To account for this, the fake factor is computed with a  $b$ -jet veto.
- 1534 4. To measure any residual dependence on the underlying jet  $p_T$  spectrum, the leading jet  $p_T$   
 1535 distribution is reweighted to match the  $p_T$  spectrum of truth jets that produce fake leptons  
 1536 in MC simulations. This results in an increase in the number of nominal and loose leptons at  
 1537 high momentum [47].

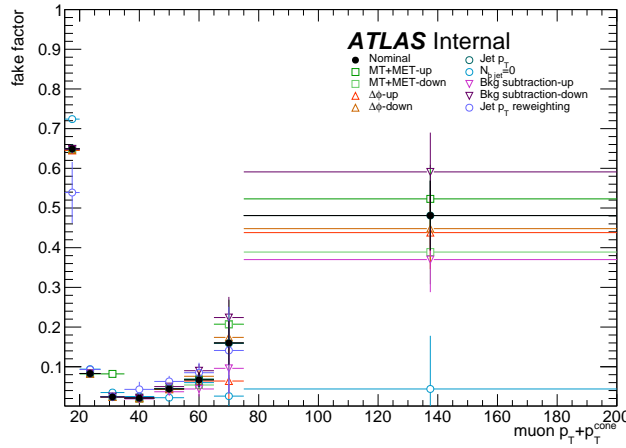


Figure 5.20: Systematic variations in the fake factor as a function of muon  $p_T + p_T^{\text{cone}}$ . The individual fake factors obtained for each systematic variation are displayed with their statistical uncertainties.

1538 **5.3.4.5 Results of the fake factor**

1539 The fake background contribution in the signal region is estimated by applying the fake factors  
 1540 to the equivalent  $NL$  region using Equation 5.9, where the fake factor used corresponds to the

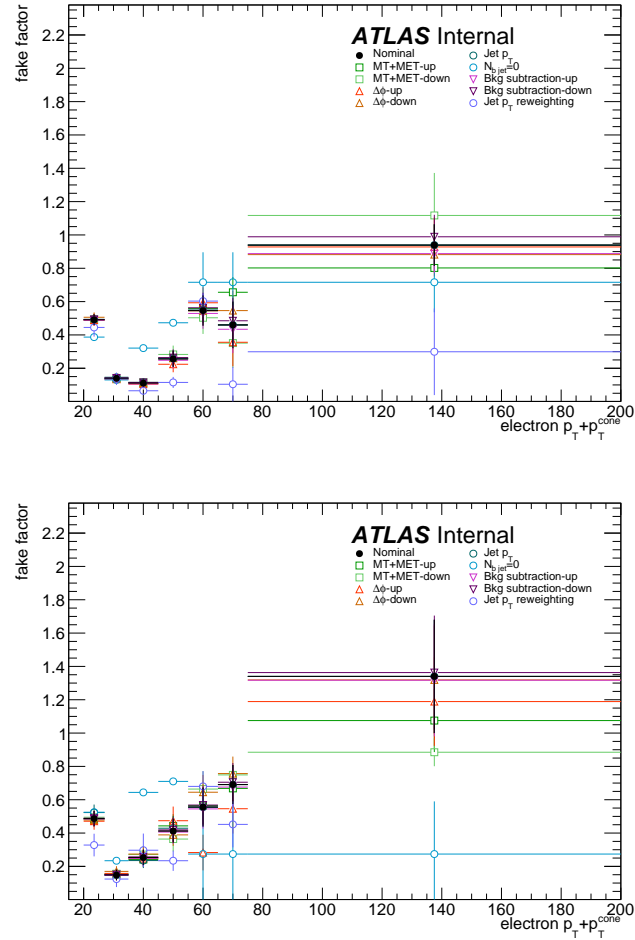


Figure 5.21: Systematic variations in the fake factor as a function of electron  $p_T + p_T^{\text{cone}}$  in the central ( $|\eta| < 1.37$ , top) and forward ( $|\eta| > 1.37$ , bottom) regions of the detector. The individual fake factors obtained for each systematic variation are displayed with their statistical uncertainties.

fake factor	$p_T$ [15, 20]	$p_T$ [20, 27]	$p_T$ [27, 35]	$p_T$ [35, 45]	$p_T$ [45, 55]	$p_T$ [55, 65]	$p_T$ [65, 75]	$p_T$ [75, 200]
nominal	0.649 ± 0.007	0.083 ± 0.002	0.024 ± 0.002	0.021 ± 0.003	0.044 ± 0.007	0.067 ± 0.018	0.160 ± 0.055	0.481 ± 0.088
MT+MET	0.649 ± 0.007	0.082 ± 0.002	0.082 ± 0.002	0.020 ± 0.003	0.045 ± 0.007	0.068 ± 0.018	0.207 ± 0.062	0.523 ± 0.086
$\Delta\phi(\ell, j)$	0.645 ± 0.008	0.083 ± 0.003	0.024 ± 0.002	0.021 ± 0.004	0.045 ± 0.008	0.064 ± 0.021	0.064 ± 0.058	0.438 ± 0.092
Jet $p_T$	0.650 ± 0.007	0.083 ± 0.002	0.024 ± 0.002	0.021 ± 0.003	0.045 ± 0.007	0.069 ± 0.018	0.159 ± 0.018	0.481 ± 0.088
$N_{b\text{-jet}} = 0$	0.724 ± 0.003	0.094 ± 0.001	0.035 ± 0.001	0.025 ± 0.002	0.022 ± 0.004	0.060 ± 0.015	0.026 ± 0.053	0.044 ± 0.134
Bkg. subtraction	0.648 ± 0.007	0.083 ± 0.002	0.024 ± 0.002	0.019 ± 0.003	0.037 ± 0.007	0.044 ± 0.019	0.096 ± 0.062	0.370 ± 0.082
Jet $p_T$ Reweighting	0.539 ± 0.077	0.093 ± 0.007	0.025 ± 0.004	0.043 ± 0.019	0.063 ± 0.014	0.085 ± 0.025	0.141 ± 0.110	1.962 ± 0.492

(a) Fake factor for muons.

fake factor	$p_T$ [20, 27]	$p_T$ [27, 35]	$p_T$ [35, 45]	$p_T$ [45, 55]	$p_T$ [55, 65]	$p_T$ [65, 75]	$p_T$ [75, 200]
nominal	0.491 ± 0.031	0.140 ± 0.020	0.111 ± 0.023	0.256 ± 0.049	0.546 ± 0.091	0.460 ± 0.140	0.939 ± 0.125
MT+MET	0.493 ± 0.030	0.138 ± 0.019	0.115 ± 0.022	0.261 ± 0.045	0.559 ± 0.084	0.656 ± 0.091	0.802 ± 0.016
$\Delta\phi(\ell, j)$	0.488 ± 0.032	0.137 ± 0.020	0.110 ± 0.025	0.283 ± 0.053	0.503 ± 0.097	0.351 ± 0.149	1.117 ± 0.255
Jet $p_T$	0.489 ± 0.035	0.134 ± 0.021	0.105 ± 0.025	0.224 ± 0.048	0.593 ± 0.093	0.356 ± 0.144	0.928 ± 0.177
$N_{b\text{-jet}} = 0$	0.506 ± 0.029	0.140 ± 0.018	0.111 ± 0.022	0.260 ± 0.046	0.545 ± 0.084	0.546 ± 0.120	0.882 ± 0.103
Bkg. subtraction	0.493 ± 0.032	0.146 ± 0.021	0.115 ± 0.024	0.259 ± 0.049	0.550 ± 0.091	0.460 ± 0.140	0.939 ± 0.125
$N_{b\text{-jet}} = 0$	0.387 ± 0.009	0.130 ± 0.008	0.321 ± 0.012	0.473 ± 0.015	0.716 ± 0.180	0.716 ± 0.180	0.716 ± 0.180
Bkg. subtraction	0.488 ± 0.031	0.138 ± 0.020	0.106 ± 0.023	0.248 ± 0.049	0.529 ± 0.092	0.434 ± 0.143	0.888 ± 0.115
Jet $p_T$ Reweighting	0.493 ± 0.031	0.142 ± 0.020	0.115 ± 0.023	0.264 ± 0.049	0.563 ± 0.090	0.485 ± 0.136	0.989 ± 0.132

(b) Fake factor for central electrons ( $|\eta| < 1.37$ ).

fake factor	$p_T$ [20, 27]	$p_T$ [27, 35]	$p_T$ [35, 45]	$p_T$ [45, 55]	$p_T$ [55, 65]	$p_T$ [65, 75]	$p_T$ [75, 200]
nominal	0.487 ± 0.046	0.148 ± 0.031	0.253 ± 0.046	0.412 ± 0.071	0.556 ± 0.117	0.691 ± 0.117	1.340 ± 0.340
MT+MET	0.483 ± 0.045	0.152 ± 0.031	0.241 ± 0.043	0.443 ± 0.070	0.565 ± 0.106	0.668 ± 0.117	1.075 ± 0.189
$\Delta\phi(\ell, j)$	0.495 ± 0.047	0.156 ± 0.033	0.271 ± 0.052	0.364 ± 0.074	0.664 ± 0.107	0.749 ± 0.056	0.885 ± 0.084
Jet $p_T$	0.471 ± 0.051	0.158 ± 0.035	0.247 ± 0.051	0.474 ± 0.085	0.283 ± 0.107	0.546 ± 0.149	1.189 ± 0.266
$N_{b\text{-jet}} = 0$	0.478 ± 0.042	0.170 ± 0.031	0.274 ± 0.046	0.389 ± 0.066	0.645 ± 0.104	0.757 ± 0.102	1.319 ± 0.326
Bkg. subtraction	0.523 ± 0.048	0.149 ± 0.033	0.235 ± 0.045	0.429 ± 0.073	0.555 ± 0.117	0.691 ± 0.117	1.340 ± 0.340
$N_{b\text{-jet}} = 0$	0.525 ± 0.011	0.234 ± 0.013	0.644 ± 0.016	0.710 ± 0.014	0.274 ± 0.316	0.274 ± 0.316	0.274 ± 0.316
Bkg. subtraction	0.484 ± 0.046	0.146 ± 0.031	0.248 ± 0.046	0.406 ± 0.071	0.545 ± 0.118	0.676 ± 0.118	1.317 ± 0.337
Jet $p_T$ Reweighting	0.328 ± 0.068	0.124 ± 0.048	0.297 ± 0.100	0.234 ± 0.061	0.680 ± 0.092	0.452 ± 0.138	2.385 ± 1.729

(c) Fake factor for forward electrons ( $1.37 < |\eta|$ ).Table 5.14: Values of the fake factor in each  $p_T$  bin and for each individual systematic source.

flavor of the loose lepton in the event. As usual, the prompt background is subtracted from the  $NL$  events using MC simulation. Charge misidentification is handled using the same method as in Section 5.3.3, with an additional set of charge flip rates calculated for loose leptons. The fake background yields in the signal region are listed in Table 5.15. An overall uncertainty of 50% is assigned to the fake background estimation in  $\mu^\pm\mu^\pm$  events, and between 40% to 90% for  $e^\pm e^\pm$  and  $\mu^\pm e^\pm$  events, including both statistical and systematic effects.

	estimated yield	$f_e$ stat. up	$f_e$ stat. dn	$f_e$ syst. up	$f_e$ syst. dn	$f_\mu$ stat. up	$f_\mu$ stat. dn	$f_\mu$ syst. up	$f_\mu$ syst. dn
$e^\pm e^\pm$	$11.42 \pm 3.13$	1.69	-1.69	1.67	-5.56	—	—	—	—
$\mu^\pm\mu^\pm$	$4.82 \pm 0.77$	—	—	—	—	0.65	-0.65	3.64	-0.61
$\mu^\pm e^\pm$	$37.08 \pm 5.16$	4.90	-4.90	5.59	-14.34	1.39	-1.39	16.10	-1.98

Table 5.15: Estimated yields for the fake lepton background. The estimated yield is shown in the first column together with the statistical uncertainty followed by the systematic uncertainties from variations of the the fake factors within their statistical (stat.) and systematic (syst.) uncertainties. The labels  $f_e$  and  $f_\mu$  indicate the fake factors for electrons and muons, respectively.

#### 5.3.4.6 Validation of the fake factor

The accuracy of the fake factor method is tested in several validation regions, the most sensitive of which is the same-sign top fakes VR (SS top VR), defined in Table 5.16. This region inverts the signal region's  $b$ -jet veto to accept events with exactly one  $b$ -jet. Due to this requirement, the dominant source of events comes from the  $t\bar{t}$  process where a  $b$ -jet fakes an isolated lepton. The distribution of the subleading lepton  $p_T$  in this VR is shown in Figure 5.22 for all lepton flavor combinations. There is good agreement between the data and the prediction, even when only taking into account the statistical uncertainty and not the large systematic uncertainties assigned to the fake estimation.

Same-sign inclusive VR
Exactly 2 same-sign signal leptons
$p_T > 27$ GeV for both leptons
$m_{ll} > 20$ GeV
$ m_{ee} - m_Z  > 15$ GeV ( $e^\pm e^\pm$ -channel only)
$N_{b\text{-jet}} = 1$
$N_{\text{jet}} \geq 2$
Leading jet $p_T > 65$ GeV
Subleading jet $p_T > 35$ GeV

Table 5.16: Selection criteria for the same-sign top fakes validation region.

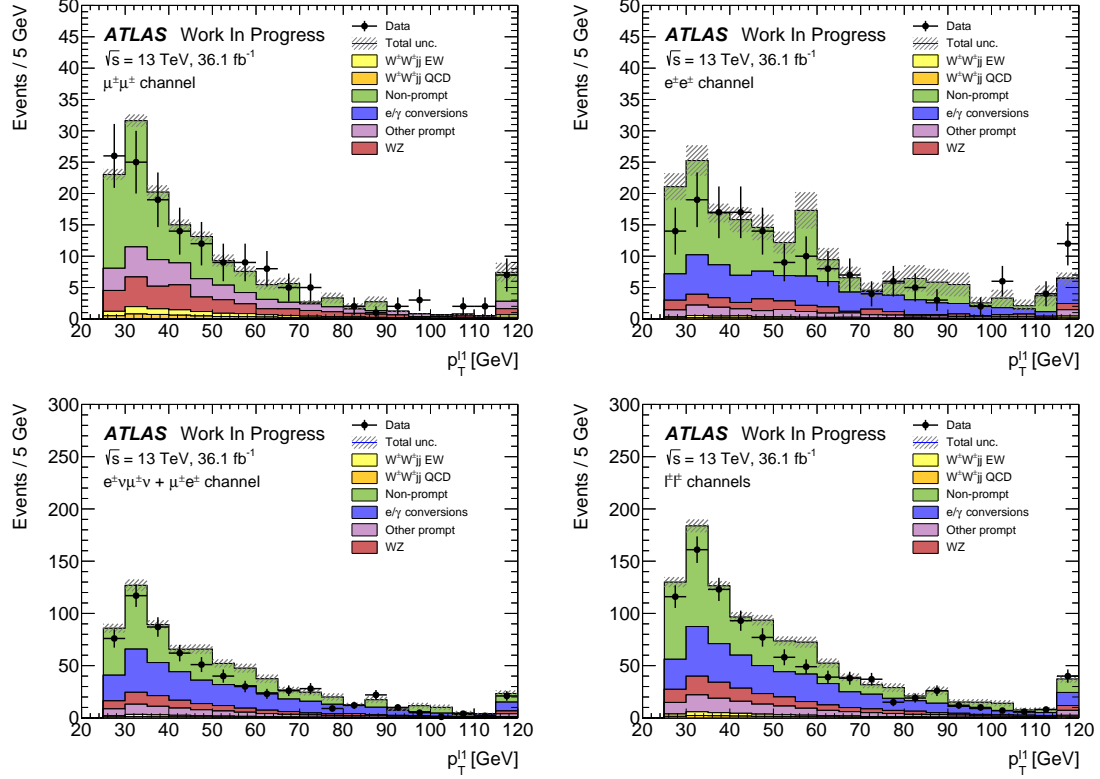


Figure 5.22: Distributions of the subleading lepton  $p_T$  in the same-sign top fakes VR for  $\mu^\pm\mu^\pm$  events (top right),  $e^\pm e^\pm$  events (top left),  $\mu^\pm e^\pm$  events (bottom left), and all events combined (bottom right). All errors are statistical only.

### 1556 5.3.5 Reduction of $WZ$ background using custom overlap removal

1557 The dominant source of prompt background in this analysis comes from  $WZ$  events where both  
 1558 bosons decay leptonically. Traditionally, the background is dealt with by imposing a veto on any  
 1559 event with a third lepton passing some loose identification criteria (the so-called *trilepton veto*). In  
 1560 the case of this analysis, if one or more leptons (in addition to the two signal leptons) passed the  
 1561 preselection criteria, the event would be rejected. However,  $WZ$  events can still enter the signal  
 1562 region if one of the leptons fails the veto selection or falls outside of the detector’s acceptance.

1563 In order to understand the sources of  $WZ$  events that are not removed by the trilepton veto,  
 1564 a study was performed on truth-level leptons<sup>16</sup> on  $W^\pm W^\pm jj$  and  $WZ$  MC samples. Events with  
 1565 three truth leptons were selected, and each was matched to its reconstruction-level partner by finding

<sup>16</sup>Truth particles are the particles produced directly by the MC generator before being passed through the full detector simulation, at which point they are considered *reconstruction-level* (or *reco-level*) particles.

the closest  $\Delta R(\text{truth, reco})$  and  $\Delta p_{\text{T,truth,reco}}$  match. For events surviving the trilepton veto, the two signal leptons were removed, and the remaining leptons represent real leptons that failed to be selected for the veto. Between 40-50% of these leptons fell outside of the eta acceptance of the analysis (see Figure 5.23) and were unrecoverable. The second largest source of leptons failing the preselection was the OR, defined in Section 5.2.1.4. The standard OR procedure appeared to be too aggressive in removing leptons in favor of jets, causing many three lepton events to “lose” their third lepton and pass the trilepton veto. Therefore a *custom OR* was investigated which would replace the standard OR in the preselection and allow for better  $WZ$  rejection by removing fewer third leptons.

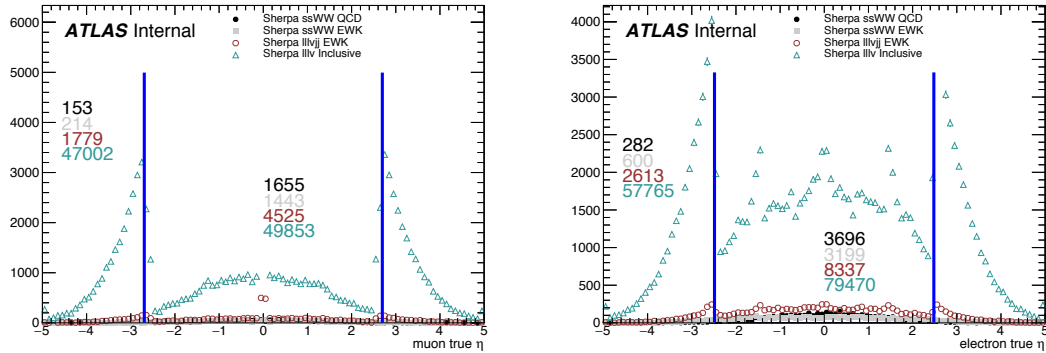


Figure 5.23: Pseudorapidity ( $\eta$ ) distributions of truth muons (top) and electrons (bottom) for Sherpa  $W^\pm W^\pm jj$  and  $WZ$  MC samples. The blue vertical lines represent the allowed  $\eta$  range for each lepton flavor. The numbers correspond to the number of raw MC events that fall within and outside of the allowed  $\eta$  range for each MC sample.

In order to construct this custom OR, a new quantity is defined between a lepton ( $l$ ) and a nearby jet ( $j$ )

$$p_{\text{T,ratio}}(l, j) = \frac{p_{\text{T},l}}{p_{\text{T},j}} \quad (5.13)$$

which, along with  $\Delta R(l, j)$ , will allow for more third leptons to pass the preselection. The idea behind including  $p_{\text{T,ratio}}$  is to be able to preferentially remove background leptons originating from jets (i.e. those that carry a low percentage of the total jet momentum) instead of removing *any* lepton near a jet. The distributions of  $p_{\text{T,ratio}}$  and the associated efficiency curves for muons and electrons can be found in Figures 5.24 and 5.26, respectively, and the distributions for  $\Delta R(\mu, j)$  for muons can be found in Figure 5.25. Since all electrons have an associated jet in the calorimeters, the  $\Delta R(e, j)$  variable is not a good quantity to use for this custom OR.

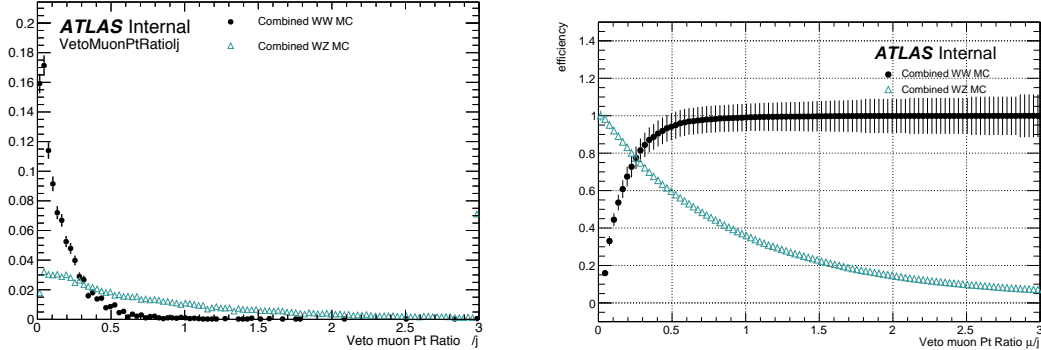


Figure 5.24: Distributions of  $p_{T,\text{ratio}}(\mu, j)$  for EWK and QCD  $W^\pm W^\pm jj$  signal (black) and  $WZ$  background (teal) for truth-matched third muons in events that pass the trilepton veto. Both distributions are normalized to unit area. The associated efficiency curves are on the right where efficiency is defined as the percentage of total events that would pass a cut on  $p_{T,\text{ratio}}(\mu, j)$  at a given value on the  $x$ -axis.

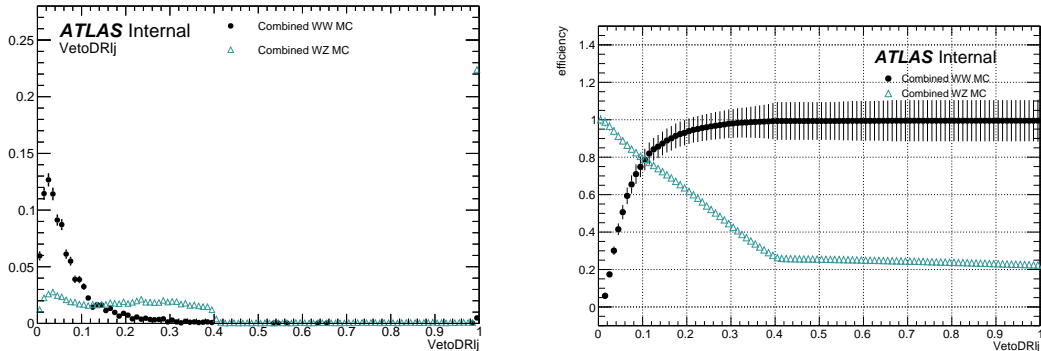


Figure 5.25: Distributions of  $\Delta R(\mu, j)$  for EWK and QCD  $W^\pm W^\pm jj$  signal (black) and  $WZ$  background (teal) for truth-matched third muons in events that pass the trilepton veto. Both distributions are normalized to unit area. The associated efficiency curves are on the right where efficiency is defined as the percentage of total events that would pass a cut on  $\Delta R(\mu, j)$  at a given value on the  $x$ -axis.

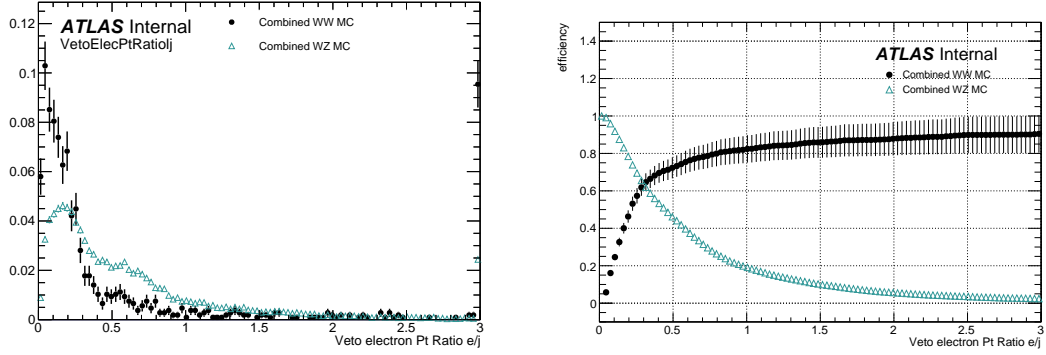


Figure 5.26: Distributions of  $p_{T,\text{ratio}}(e,j)$  for EWK and QCD  $W^\pm W^\pm jj$  signal (black) and  $WZ$  background (teal) for truth-matched third electrons in events that pass the trilepton veto. Both distributions are normalized to unit area. The associated efficiency curves are on the right where efficiency is defined as the percentage of total events that would pass a cut on  $p_{T,\text{ratio}}(e,j)$  at a given value on the  $x$ -axis.

1584 A workingpoint for the Custom OR was chosen by requiring 90% signal retention for muons  
 1585 and 90% background rejection for electrons. The cut on electrons was allowed to be much tighter  
 1586 because the number of signal events with a third electron is considerably smaller than for muons.  
 1587 It should be emphasized that the signal events present in Figures 5.24-5.26 do not represent the full  
 1588 set of signal events, but only those with a real third lepton (which must come from some source  
 1589 other than the signal  $W^\pm W^\pm jj$  process). For muons, a logical ‘or’ of  $p_{T,\text{ratio}}(\mu,j)$  and  $\Delta R(\mu,j)$  is  
 1590 used to maximize the third lepton acceptance due to correlations between the quantities, as shown  
 1591 in Figure 5.27; for electrons, only a cut on  $p_{T,\text{ratio}}(e,j)$  is used. The Custom OR workingpoint is  
 1592 outlined in Table 5.17.

Custom OR Definition	
Muons	$p_{T,\text{ratio}}(\mu,j) > 0.40 \text{ or } \Delta R(\mu,j) > 0.15$
Electrons	$p_{T,\text{ratio}}(e,j) > 0.18$

Table 5.17: Custom OR definition. Leptons must pass this selection in order to be counted for the trilepton veto.

1593 Tests of the performance of the Custom OR yield promising results, with approximately 20%  
 1594 reduction in  $WZ$  background compared to less than 2% signal loss in the signal region. Unfortu-  
 1595 nately, due to differences between the primary analysis framework and the one used for testing,  
 1596 in practice the gains in  $WZ$  rejection are not nearly as substantial, and ultimately the Custom  
 1597 OR is not included in the final analysis. However, it is still a potentially useful tool for improving

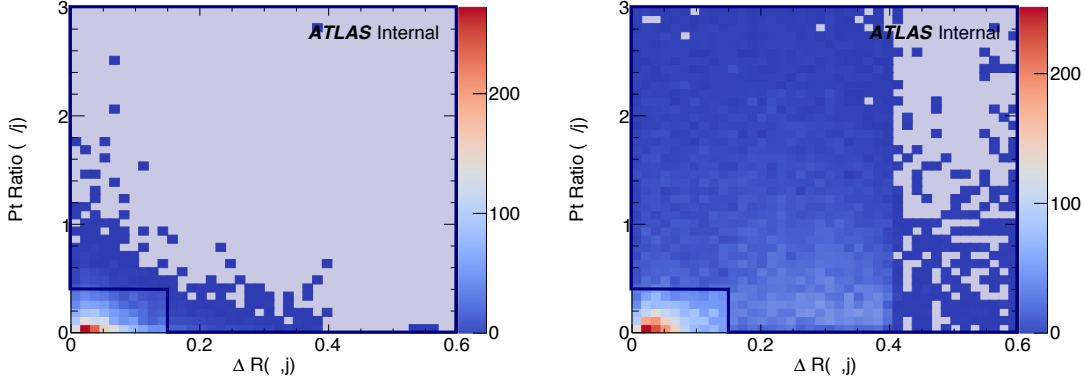


Figure 5.27: Two-dimensional plots of  $p_{T,\text{ratio}}(\mu, j)$  vs  $\Delta R(\mu, j)$  for truth-matched third muons in events that pass the trilepton veto for EWK and QCD  $W^\pm W^\pm jj$  signal (left) and  $WZ$  background (right). The blue overlay indicates the area in which the third leptons will pass the custom OR and result in the event failing the trilepton veto.

1598 background rejection via lepton number vetoes in analyses with overly aggressive OR procedures.

#### 1599 5.4 Cross section measurement

1600 The  $W^\pm W^\pm jj$  EWK cross section is extracted from the signal region using a maximum-likelihood  
 1601 fit applied simultaneously to four  $m_{jj}$  bins in the signal region as well as to the low- $m_{jj}$  and  $WZ$   
 1602 control regions. For the fit and cross section extraction, the signal region is defined as in Table 5.8  
 1603 with the dijet invariant mass requirement raised to  $m_{jj} > 500$  GeV. The low- $m_{jj}$  region is defined  
 1604 to mirror the signal region exactly with the dijet invariant mass inverted to  $200 < m_{jj} < 500$  GeV,  
 1605 and the  $WZ$  control region is defined previously in Section 5.3.1.

1606 The signal and low- $m_{jj}$  regions are split into six channels based on the flavor and charge of  
 1607 the dilepton pair:  $\mu^+\mu^+$ ,  $\mu^-\mu^-$ ,  $\mu^+e^+$ ,  $\mu^-e^-$ ,  $e^+e^+$ , and  $e^-e^-$ . This split by charge increases the  
 1608 sensitivity of the measurement due to the  $W^+/W^-$  charge asymmetry at hadron colliders favoring  
 1609 the production of  $W^+$  bosons [80]. Since the signal events contain two  $W$  bosons, the signal strength  
 1610 compared to charge-symmetric backgrounds is much greater in the  $++$  channels for both charges  
 1611 combined. The  $WZ$  control region is included in the fit as a single bin ( $l^\pm l^\pm l^\pm$ ).

1612 The maximum likelihood fit and cross section extractions are outlined in Sections 5.4.1 and  
 1613 5.4.3, respectively. The results of the cross section measurement and of the analysis as a whole are  
 1614 presented in Section 5.6.

1615 **5.4.1 Maximum likelihood fit**

1616 **TODO:** This section is very similar to what is written in the support note... May need to put  
 1617 some work into flushing it out so it's not so close to copy-paste The number of predicted signal  
 1618 events in each channel  $c$  and  $m_{jj}$  bin  $b$  can be calculated from the SM predicted signal cross section  
 1619  $\sigma_{\text{theo}}^{\text{tot}}$ , the total integrated luminosity  $\mathcal{L}$ , the signal acceptance  $\mathcal{A}$ , and the efficiency corrections  $\mathcal{C}(\theta)$ ,  
 1620 where  $\theta$  represents the set of nuisance parameters that parameterize the effects of each systematic  
 1621 uncertainty on the signal and background expectations. The acceptance and efficiency corrections  
 1622 will be covered in more detail in Section 5.4.2.

$$N_{cb}^{\text{sig}}(\theta) = \sigma_{\text{theo}}^{\text{tot}} \mathcal{A}_b \mathcal{C}_b(\theta) \mathcal{L} \quad (5.14)$$

1623 A signal strength parameter  $\mu$  is defined as the ratio of the measured cross section to the SM  
 1624 predicted cross section. The expected number of events in a given channel and bin can then be  
 1625 expressed as the sum of the estimated background ( $N_{cb}^{\text{bkg}}(\theta)$ ) and the number of predicted signal  
 1626 events scaled by  $\mu$ :

$$\begin{aligned} N_{cb}^{\text{exp}}(\theta) &= \mu N_{cb}^{\text{sig}}(\theta) + N_{cb}^{\text{bkg}}(\theta) \\ &= \mu \sigma_{\text{theo}}^{\text{tot}} \mathcal{A}_b \mathcal{C}_b(\theta) \mathcal{L} + N_{cb}^{\text{bkg}}(\theta) \end{aligned} \quad (5.15)$$

1627 The nuisance parameters are constrained by Gaussian probability distribution functions, and  
 1628 the normalization of the  $WZ$  background mentioned in Section 5.3.1 is included in the fit as a free  
 1629 parameter. The expected yields for signal and background processes are adjusted by the set of  
 1630 nuisance parameters within the constraints of the systematic uncertainties. The yields after the fit  
 1631 correspond to the value that best matches the observed data.

1632 The number of events per channel and bin after the fit can be written as a sum of the predicted  
 1633 event yields for each sample  $s$ :

$$\nu_{cb}(\phi, \theta, \gamma_{cb}) = \gamma_{cb} \sum_s [\eta_{cs}(\theta) \phi_{cs}(\theta) \lambda] h_{cbs}(\theta) \quad (5.16)$$

1634 In this equation, the fitted number of events in a given channel and bin is obtained by weighting  
 1635 the histogram of predicted yields  $h_{cbs}$  by the product of a given luminosity  $\lambda$  and any normalization  
 1636 factors  $\phi_{cs}$  that may be given for each channel and sample. The input histogram and the normaliza-  
 1637 tion factors may depend on the nuisance parameters  $\theta$  taking into account sources of systematic  
 1638 uncertainty. Uncertainties on the normalization factors  $\eta_{cs}(\theta)$  are also included. Finally, bin-by-bin  
 1639 scale factors  $\gamma_{cb}$  are included to parameterize the statistical uncertainties of the MC predictions.

1640 The binned likelihood function is given by a product of Gaussian functions for the luminosity  
 1641 and for the background uncertainties and a product of Poisson functions for the number of observed

1642 events in each bin and channel:

$$L(\mu|\theta) = \mathcal{G}(\mathcal{L}|\theta_{\mathcal{L}}, \sigma_{\mathcal{L}}) \cdot \prod_c \prod_b \mathcal{P}(N_{cb}^{\text{meas.}} | \nu_{cb}(\mu)) \prod_p \mathcal{G}(\theta_p^0 | \theta_p) \quad (5.17)$$

1643 where  $\mathcal{G}$  and  $\mathcal{P}$  are the Gaussian and Poisson functions, respectively. As before,  $\mathcal{L}$  represents the  
 1644 integrated luminosity with uncertainty  $\sigma_{\mathcal{L}}$  and associated nuisance parameter  $\theta_{\mathcal{L}}$ . The number of  
 1645 measured events in a given bin and channel is represented by  $N_{cb}^{\text{meas.}}$ , and  $\nu_{cb}(\mu)$  is the predicted  
 1646 number of events defined in Equation 5.16 expressed as a function of the signal strength  $\mu$ . Finally,  
 1647 the set of nuisance parameters  $\theta$  and any auxiliary measurements used to constrain them  $\theta^0$  are  
 1648 multiplied for each parameter  $p$ .

1649 The profile likelihood ratio is defined as

$$q_{\mu} = -2 \ln \frac{L(\mu, \hat{\theta}_{\mu})}{L(\hat{\mu}, \hat{\theta})} \quad (5.18)$$

1650 with  $\hat{\mu}$  and  $\hat{\theta}$  as the unconditional maximum likelihood estimates and  $\hat{\theta}$  as the conditional maximum  
 1651 likelihood estimate for a given value of  $\mu$ . The fitted signal strength  $\hat{\mu}$  is obtained by maximizing  
 1652 the likelihood function with respect to all parameters. The compatibility of the observed data  
 1653 with the background-only hypothesis can then be calculated by setting  $\mu = 0$ . Observation of the  
 1654  $W^{\pm}W^{\pm}jj$  EWK process is claimed if the data is found to be inconsistent with the background-only  
 1655 hypothesis by more than  $5\sigma$ .

#### 1656 5.4.2 Definition of the fiducial volume

1657 Before extracting the cross section, it is necessary to define the fiducial volume, or the phase space  
 1658 of measureable events. It is a subset of the total phase space defined by selection requirements  
 1659 designed to mirror those applied in the analysis as closely as possible. The selection criteria for the  
 1660 fiducial volume are listed in Table 5.18.

1661 In MC simulations, the total phase space is generated, providing the total theoretical cross section  
 1662  $\sigma_{\text{theo}}^{\text{tot}}$  and the total number of signal events  $\mathcal{N}_{\text{sig}}^{\text{tot}}$ <sup>17</sup>. After applying the fiducial selection at truth  
 1663 level, the total number of signal events in the fiducial region  $\mathcal{N}_{\text{sig}}^{\text{fid}}$  is obtained. An acceptance factor  
 1664  $\mathcal{A}$  is used to represent the efficiency of events falling in the fiducial region at truth level:

$$\mathcal{A} = \frac{\mathcal{N}_{\text{sig}}^{\text{fid}}}{\mathcal{N}_{\text{sig}}^{\text{tot}}} \quad (5.19)$$

---

<sup>17</sup>For the purpose of clarity, the number of events at truth level is represented by a script  $\mathcal{N}$ , and the number of events at reconstruction level uses a regular  $N$ .

Fiducial region selection	
Lepton selection	Two prompt leptons ( $e, \mu$ ) $p_T > 27$ GeV and $ \eta  < 2.5$ for both leptons Both leptons with the same electric charge Dilepton invariant mass $m_{ll} > 20$ GeV Dilepton separation $\Delta R(ll) > 0.3$
Missing transverse energy	Two neutrino system with $p_T^{\nu\nu} > 30$ GeV
Jet selection	At least two jets Leading jet $p_T > 65$ GeV Subleading jet $p_T > 35$ GeV Leading and subleading jet $ \eta  < 4.5$ Jet-lepton separation $\Delta R(l, j) > 0.3$ Dijet invariant mass $m_{jj} > 500$ GeV Dijet separation $\Delta y_{jj} > 2.0$

Table 5.18: Definition of the fiducial volume.

1665 A correction factor  $\mathcal{C}$  is also necessary to translate from the truth level fiducial volume to the  
 1666 reconstruction level signal region and is defined in terms of the number of reconstruction level MC  
 1667 events in the signal region  $N_{\text{sig},\text{MC}}^{\text{SR}}$ :

$$\mathcal{C} = \frac{N_{\text{sig},\text{MC}}^{\text{SR}}}{N_{\text{sig}}^{\text{fid}}} \quad (5.20)$$

1668 Since the fit is binned in  $m_{jj}$ , the acceptance and efficiency correction factors need to be as well.  
 1669 Therefore,  $\mathcal{A}_i$  and  $\mathcal{C}_{ij}$  are written in terms of truth  $m_{jj}$  bins  $i$  and reconstruction  $m_{jj}$  bins  $j$ . A  
 1670 graphical representation of these regions and the use of the acceptance and correction factors can  
 1671 be seen in Figure 5.28.

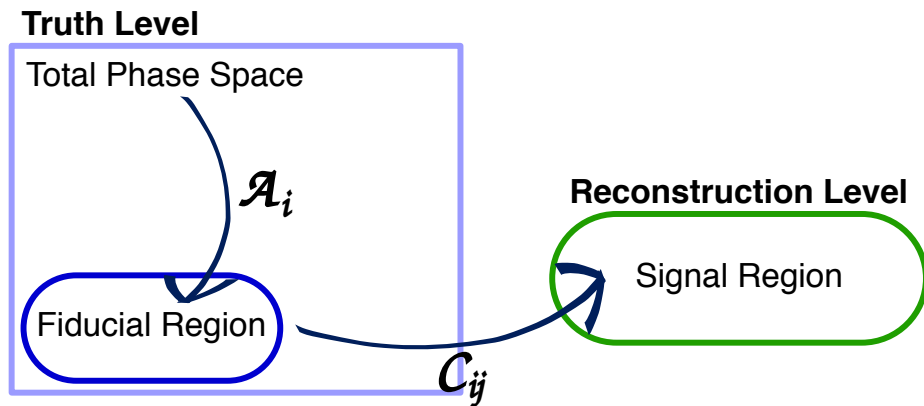


Figure 5.28: Visual representation of the different kinematic regions relevant to the cross section measurement. The acceptance factor  $\mathcal{A}$  converts from the truth level total phase space to the truth level fiducial region, and the efficiency correction  $\mathcal{C}$  translates the fiducial region into the reconstruction level signal region.

1672 **5.4.3 Cross section extraction**

1673 The  $W^\pm W^\pm jj$  EWK fiducial cross section is measured using the signal strength parameter  $\mu$  that is  
 1674 determined by the maximum likelihood fit. This parameter is dependent on the nuisance parameters  
 1675  $\theta$  and can be written explicitly in terms of the measured and theoretical cross sections as:

$$\mu(\theta) = \frac{\sigma_{\text{meas}}^{\text{SR}}}{\sigma_{\text{theo}}^{\text{SR}}} \quad (5.21)$$

1676 In the simple case with only one bin, the equation for the total number of expected events in the  
 1677 signal region first introduced in Equation 5.15 can be written as:

$$N_{\text{exp}}^{\text{SR}}(\theta) = \mu(\theta) \cdot \sigma_{\text{theo}}^{\text{tot}} \cdot \mathcal{L} \cdot \mathcal{A} \cdot \mathcal{C}(\theta) + N_{\text{bkg}}^{\text{SR}}(\theta) \quad (5.22)$$

1678 with the non-binned versions of  $\mathcal{A}$  and  $\mathcal{C}$  defined in Equations 5.19 and 5.20, respectively.

1679 If the measured fiducial cross section is written as:

$$\sigma_{\text{meas}}^{\text{fid}} = \mu \cdot \mathcal{A} \cdot \sigma_{\text{theo}}^{\text{tot}} \quad (5.23)$$

1680 then Equation 5.22 can be rearranged to read:

$$\sigma_{\text{meas}}^{\text{fid}} = \frac{N_{\text{exp}}^{\text{SR}}(\theta) - N_{\text{bkg}}^{\text{SR}}(\theta)}{\mathcal{L} \cdot \mathcal{C}(\theta)} \quad (5.24)$$

1681 The measured fiducial cross section can finally be rewritten in terms of  $\hat{\mu}$ , which is the best estimator  
 1682 of the signal strength as extracted from the fit:

$$\begin{aligned} \sigma_{\text{meas}}^{\text{fid}} &= \hat{\mu}(\theta) \cdot \sigma_{\text{theo}}^{\text{tot}} \cdot \mathcal{A} \\ &= \hat{\mu}(\theta) \cdot \sigma_{\text{theo}}^{\text{fid}} \end{aligned} \quad (5.25)$$

1683 In practice, however, the cross section is not extracted from a single bin, and Equation 5.22  
 1684 becomes for a single channel in truth and reconstruction level  $m_{jj}$  bins  $i$  and  $j$ , respectively:

$$N_{\text{exp}}^{\text{SR}}(\theta) = \mu(\theta) \cdot \sigma_{\text{theo}}^{\text{tot}} \cdot \mathcal{L} \cdot \sum_i \mathcal{A}_i \cdot \sum_j \mathcal{C}_{ij} + \sum_j N_{\text{bkg},j}^{\text{SR}}(\theta) \quad (5.26)$$

1685 where now the binned versions of  $\mathcal{A}_i$  and  $\mathcal{C}_{ij}$  are used. This equation can be extended to include all  
 1686 the analysis channels by increasing the number of bins  $i$  and  $j$ . Additionally, it can be shown that  
 1687 Equation 5.25 holds for this more complex case as well [47], provided care is taken to ensure that  
 1688 all the uncertainties are handled properly.

---

1689 **5.5 Summary of uncertainties**

1690 Systematic uncertainties enter the final fit as nuisance parameters which can impact the estimated  
1691 signal and background yields and the shapes of the  $m_{jj}$  distributions. These uncertainties can arise  
1692 from the experimental methods or from the theoretical calculations used in the analysis. This section  
1693 summarizes the systematic uncertainties; the experimental uncertainties are detailed in Section 5.5.1,  
1694 and the theoretical uncertainties are covered in Section 5.5.2. The impacts of the systematic uncer-  
1695 tainties on the final cross section measurement are summarized in Table 5.19.

Source	Impact [%]
Reconstruction	$\pm 4.0$
Electrons	$\pm 0.5$
Muons	$\pm 1.2$
Jets and $E_T^{\text{miss}}$	$\pm 2.8$
$b$ -tagging	$\pm 2.0$
Pileup	$\pm 1.5$
Background	$\pm 5.0$
Misid. leptons	$\pm 3.9$
Charge misrec.	$\pm 0.3$
$WZ$	$\pm 1.3$
$W^\pm W^\pm jj$ QCD	$\pm 2.8$
Other	$\pm 0.8$
Signal	$\pm 3.6$
Interference	$\pm 1.0$
EW Corrections	$\pm 1.3$
Shower, Scale, PDF & $\alpha_s$	$\pm 3.2$
Total	$\pm 7.4$

Table 5.19: Impact of various systematic effects on the fiducial cross section measurement. The impact of a given source of uncertainty is computed by performing the fit with the corresponding nuisance parameter varied up or down by one standard deviation from its nominal value.

---

1696 **5.5.1 Experimental uncertainties**

1697 Experimental uncertainties include detector effects as well as uncertainties on the background es-  
1698 timation methods. Sources of systematic uncertainty on the measurement of physics objects are  
1699 listed in Table 5.20, grouped by the relevant object type. For backgrounds estimated from MC  
1700 simulations, variations in these sources of uncertainty are propagated through the analysis to obtain  
1701 the corresponding uncertainties on the event yields. Additional experimental uncertainties include  
1702 the integrated luminosity, the photon conversion rate from Section 5.3.2, and the data driven charge

misidentification and fake lepton background estimations from Sections 5.3.3 and 5.3.4.5, respectively.

The largest sources of experimental uncertainty on the MC estimations come from the jet-related uncertainties and the  $b$ -tagging efficiency, while the largest uncertainty on the background estimation comes from the fake factor. The effects of the uncertainties on the  $W^\pm W^\pm jj$  EWK signal and the dominant MC estimated background,  $WZ$ , are listed in Tables 5.21 and 5.22, respectively. Since the overall contributions from other processes estimated with MC are small, the uncertainties on these backgrounds have a lesser impact on the final measurement; these tables can be found in Appendix B.1.

Experimental uncertainties	
Electrons	Energy resolution
	Energy scale
	Identification efficiency
	Isolation efficiency
	Reconstruction efficiency
	Trigger efficiency
Muons	Energy scale
	Identification efficiency
	Inner detector track resolution
	Muon spectrometer resolution
	Trigger efficiency
$E_T^{\text{miss}}$	Resolution
	Scale
Jets	Energy resolution
	Energy scale
	JVT cut efficiency
	$b$ -tagging efficiency
	Jets from pileup

Table 5.20: List of sources of experimental uncertainties on the reconstruction of physics objects.

$W^\pm W^\pm jj$ EWK	$e^\pm e^\pm$ % Yield	$\mu^\pm e^\pm$ % Yield	$\mu^\pm \mu^\pm$ % Yield
Jet-related Uncertainties	2.28	2.22	2.28
$b$ -tagging efficiency	1.81	1.76	1.74
Pile-up	0.48	0.97	2.42
Trigger efficiency	0.02	0.08	0.47
Lepton reconstruction/ID	1.45	1.14	1.83
MET reconstruction	0.26	0.17	0.21

Table 5.21: Impact of experimental uncertainties for the  $W^\pm W^\pm jj$  EWK processes in all channels.

$WZ$	$e^\pm e^\pm$ % Yield	$\mu^\pm e^\pm$ % Yield	$\mu^\pm \mu^\pm$ % Yield
Jet-related Uncertainties	9.58	5.03	8.45
b-tagging efficiency	2.49	2.23	2.40
Pile-up	2.99	3.49	3.33
Trigger efficiency	0.03	0.09	0.43
Lepton reconstruction/ID	1.52	1.24	3.07
MET reconstruction	0.93	0.79	1.63

Table 5.22: Impact of experimental uncertainties for the  $WZ$  process in all channels.

### 1712 5.5.2 Theoretical uncertainties

1713 It is also necessary to consider uncertainties on the theoretical predictions in the fiducial region. They  
 1714 include the choice of PDF set, the value of the strong coupling constant  $\alpha_s$ , the renormalization  
 1715 scale  $\mu_R$ , the factorization scale  $\mu_F$ , and the parton showering. The size of these uncertainties are  
 1716 measured by generating new samples with variations in a chosen parameters and comparing them  
 1717 to samples using the nominal choice of the parameter. Internal variations on the PDF sets or using  
 1718 a different set entirely results in a relative uncertainty of up to 2.25% on the nominal sample. The  
 1719 impact from varying  $\alpha_s$  is very small, on the order of < 0.01%. The factorization and renormalization  
 1720 scales are independently varied between 0.5-2.0 from their nominal values of 1.0. This results in  
 1721 relative uncertainties on the prediction of up to 15%. Finally, varying the parameters in the parton  
 1722 showering results in up to 8% uncertainty.

#### 1723 5.5.2.1 Uncertainties from EWK-QCD interference

1724 As mentioned in Section 5.0.2,  $W^\pm W^\pm jj$  production consists of both EWK processes. The two  
 1725 production modes cannot be naively separated due to cross terms in the matrix element calculation.  
 1726 These cross terms are referred to as *interference* terms. Since the  $W^\pm W^\pm jj$  EWK production is  
 1727 the focus of the analysis, and the signal region is designed to preferentially select those events, it is  
 1728 important to measure the size of the EWK-QCD interference contributions.

1729 The interference effects are estimated using the `MadGraph` MC generator, as it has a feature that  
 1730 allows direct modelling of the interference term. This allows four samples to be generated:

- 1731 1. Inclusive: All available diagrams are used in the matrix element calculation
- 1732 2. EWK only: Only EWK diagrams ( $\mathcal{O}(\alpha_{\text{EWK}}) = 4$ ) are used
- 1733 3. QCD only: Only QCD diagrams ( $\mathcal{O}(\alpha_s) = 2 \otimes \mathcal{O}(\alpha_{\text{EWK}}) = 2$ ) are used

1734     4. Interference: Only the interference terms are used

1735     A minimal set of generator level cuts, listed in Table 5.23, is applied in order to avoid biasing the  
 1736     sample towards either production mode. The cross sections for each of the four channels can be  
 1737     found in Table 5.24. The size of the interference is found to be approximately 6% of the total cross  
 1738     section and is taken as a systematic uncertainty.

Generator level cuts
$\Delta\eta_{jj} < 10$
Jet $p_T > 20$ GeV
$M_{jj} > 10$ GeV

Table 5.23: The set of generator level cuts used for generating the interference samples with **MadGraph**.

Sample	$\sigma$ (fb)
Inclusive	$3.646 \pm 0.0012$
EWK only	$2.132 \pm 0.0005$
QCD only	$1.371 \pm 0.0008$
Interference	$0.227 \pm 0.0002$

Table 5.24: Cross sections for each different  $W^\pm W^\pm jj$  production mode (inclusive, EWK only, QCD only, and interference only) generated using **MadGraph**. The cross sections are calculated using a minimal set of generator level cuts from events where the  $W$  decays to a muon.

## 1739     5.6 Results

1740     After running the full analysis chain, the event yields in the signal region, low- $m_{jj}$  control region,  
 1741     and  $WZ$  control region as well as associated nuisance parameters representing the uncertainties are  
 1742     passed to the maximum likelihood fit. From this fit, the normalization factor for the  $WZ$  control  
 1743     region  $\mu_{WZ}$  and the signal strength parameter in the signal region  $\mu_{\text{obs}}$  are determined, and the  
 1744     predicted yields in each input bin have been shifted according to the process detailed in Section 5.4.1.

1745     The  $WZ$  normalization factor is measured to be:

$$\mu_{WZ} = 0.88^{+0.07}_{-0.07}(\text{stat})^{+0.31}_{-0.21}(\text{theory})^{+0.22}_{-0.11}(\text{sys}) \quad (5.27)$$

1746     and is constrained primarily by the number of data events in the  $WZ$  control region. The observed  
 1747     signal strength of  $W^\pm W^\pm jj$  EWK production, defined in Equation 5.21, is extracted from the fit  
 1748     and measured with respect to the prediction of the **SHERPA v2.2.2** MC generator:

$$\mu_{\text{obs}} = 1.45^{+0.25}_{-0.24}(\text{stat})^{+0.06}_{-0.08}(\text{theory})^{+0.27}_{-0.22}(\text{sys}) \quad (5.28)$$

1749 This corresponds to a rejection of the background-only hypothesis with a significance of  $6.9\sigma$ .

1750 The observed number of data events are compared to the predicted signal and background yields  
 1751 in the signal region in Table 5.25 before applying the fit and in Table 5.26 after the fit. The  $m_{jj}$   
 1752 distributions for data and prediction are shown in Figure 5.29 after the fit, and the fitted event  
 1753 yields in the low- $m_{jj}$  and  $WZ$  control regions are shown in Figure 5.30. Additional distributions  
 1754 can be found in Appendix B.

	$e^+e^+$	$e^-e^-$	$\mu^+e^+$	$\mu^-e^-$	$\mu^+\mu^+$	$\mu^-\mu^-$	combined
$WZ$	$1.9 \pm 0.6$	$1.3 \pm 0.4$	$14 \pm 4$	$8.9 \pm 2.6$	$5.5 \pm 1.6$	$3.6 \pm 1.1$	$35 \pm 10$
Non-prompt	$4.1 \pm 2.3$	$2.3 \pm 1.7$	$9 \pm 5$	$6 \pm 4$	$0.57 \pm 0.15$	$0.67 \pm 0.25$	$23 \pm 10$
$e/\gamma$ conversions	$1.74 \pm 0.29$	$1.8 \pm 0.4$	$6.1 \pm 1.6$	$3.7 \pm 0.8$	—	—	$13.4 \pm 2.5$
Other prompt	$0.17 \pm 0.05$	$0.14 \pm 0.04$	$0.90 \pm 0.19$	$0.60 \pm 0.14$	$0.36 \pm 0.10$	$0.19 \pm 0.05$	$2.4 \pm 0.5$
$W^\pm W^\pm jj$ QCD	$0.38 \pm 0.13$	$0.16 \pm 0.05$	$3.0 \pm 1.0$	$1.2 \pm 0.4$	$1.8 \pm 0.6$	$0.76 \pm 0.25$	$7.3 \pm 2.5$
Expected background	$8.2 \pm 2.4$	$5.7 \pm 1.8$	$33 \pm 7$	$21 \pm 5$	$8.2 \pm 1.8$	$5.3 \pm 1.2$	$81 \pm 14$
$W^\pm W^\pm jj$ EWK	$3.8 \pm 0.6$	$1.49 \pm 0.22$	$16.5 \pm 2.5$	$6.5 \pm 1.0$	$9.1 \pm 1.4$	$3.5 \pm 0.5$	$41 \pm 6$
Data	10	4	44	28	25	11	122

Table 5.25: Table of the data and prediction event yields in the signal region before the fit. Numbers are shown for the six lepton flavor and charge channels and for all channels combined. Here the  $WZ$  background yields are normalized to the data in the  $WZ$  control region. The background estimations from the fake factor are included in the “Non-prompt” category, and backgrounds from  $V\gamma$  production and electron charge misidentification are combined in the “ $e/\gamma$  conversions” category. Finally,  $ZZ$ ,  $VVV$ , and  $t\bar{t}V$  backgrounds are combined in the “Other prompt” category.

	$e^+e^+$	$e^-e^-$	$\mu^+e^+$	$\mu^-e^-$	$\mu^+\mu^+$	$\mu^-\mu^-$	combined
$WZ$	$1.49 \pm 0.30$	$1.10 \pm 0.26$	$11.7 \pm 1.7$	$8.0 \pm 1.3$	$5.0 \pm 0.6$	$3.5 \pm 0.6$	$31 \pm 4$
Non-prompt	$2.2 \pm 1.3$	$1.2 \pm 0.7$	$5.7 \pm 2.8$	$4.5 \pm 1.8$	$0.57 \pm 0.06$	$0.65 \pm 0.14$	$15 \pm 6$
$e/\gamma$ conversions	$1.6 \pm 0.4$	$1.6 \pm 0.5$	$6.3 \pm 1.6$	$4.3 \pm 1.1$	—	—	$13.8 \pm 2.9$
Other prompt	$0.16 \pm 0.04$	$0.14 \pm 0.04$	$0.90 \pm 0.19$	$0.63 \pm 0.13$	$0.39 \pm 0.09$	$0.22 \pm 0.05$	$2.4 \pm 0.5$
$W^\pm W^\pm jj$ QCD	$0.35 \pm 0.13$	$0.15 \pm 0.05$	$2.9 \pm 1.0$	$1.2 \pm 0.4$	$1.8 \pm 0.6$	$0.76 \pm 0.25$	$7.2 \pm 2.4$
Expected background	$5.8 \pm 1.5$	$4.1 \pm 1.1$	$27 \pm 4$	$18.7 \pm 2.6$	$7.7 \pm 0.8$	$5.1 \pm 0.6$	$69 \pm 7$
$W^\pm W^\pm jj$ EWK	$5.6 \pm 1.0$	$2.2 \pm 0.4$	$24 \pm 5$	$9.4 \pm 1.8$	$13.5 \pm 2.5$	$5.2 \pm 1.0$	$60 \pm 11$
Data	10	4	44	28	25	11	122

Table 5.26: Table of the data and prediction event yields in the signal region after the fit. Numbers are shown for the six lepton flavor and charge channels and for all channels combined. The background estimations from the fake factor are included in the “Non-prompt” category, and backgrounds from  $V\gamma$  production and electron charge misidentification are combined in the “ $e/\gamma$  conversions” category. Finally,  $ZZ$ ,  $VVV$ , and  $t\bar{t}V$  backgrounds are combined in the “Other prompt” category.

1755 The last ingredient necessary to measure the  $W^\pm W^\pm jj$  EWK cross section is the theory predicted  
 1756 cross section in the fiducial region defined in Table 5.18. SHERPA v2.2.2 is used for the calculation,  
 1757 and the cross section in the total generator phase space is  $40.81 \pm 0.05$  fb, and the fiducial cross section  
 1758 is  $2.01 \pm 0.02$  fb. This corresponds to an acceptance factor of  $\mathcal{A} = 0.0493 \pm 0.0002$ . Uncertainties on  
 1759 the simulation are estimated using variations of the scale, parton shower, and PDF set. The final

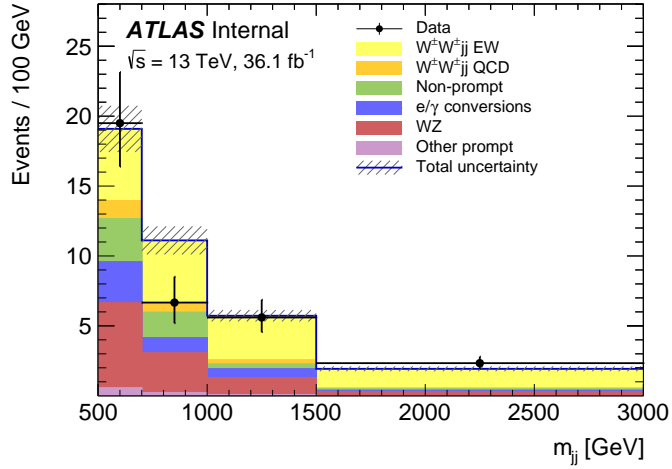


Figure 5.29: The dijet invariant mass  $m_{jj}$  distributions for data and predicted signal and background in the signal region after the fit. The shaded band represents the statistical and systematic uncertainties added in quadrature. Note that the bins have been scaled such that they represent the number of events per 100 GeV in  $m_{jj}$ . The background estimations from the fake factor are included in the “Non-prompt” category, and backgrounds from  $V\gamma$  production and electron charge misidentification are combined in the “ $e/\gamma$  conversions” category. Finally,  $ZZ$ ,  $VVV$ , and  $t\bar{t}V$  backgrounds are combined in the “Other prompt” category.

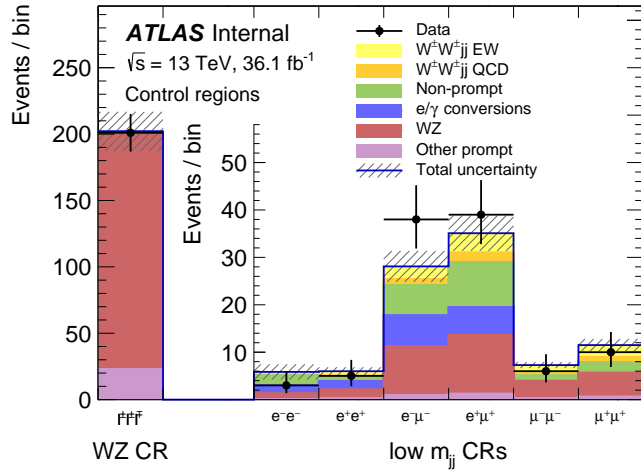


Figure 5.30: The event yields for data and predicted signal and background in the  $WZ$  and low- $m_{jj}$  control regions after the fit. The shaded band represents the statistical and systematic uncertainties added in quadrature. The background estimations from the fake factor are included in the “Non-prompt” category, and backgrounds from  $V\gamma$  production and electron charge misidentification are combined in the “ $e/\gamma$  conversions” category. Finally,  $ZZ$ ,  $VVV$ , and  $t\bar{t}V$  backgrounds are combined in the “Other prompt” category.

1760 prediction used in the cross section measurement including uncertainties from Section 5.5.2 is:

$$\sigma_{\text{SHERPA}}^{\text{fid}} = 2.01 \pm 0.02(\text{stat}) \pm^{+0.29}_{-0.23}(\text{scale}) \pm^{+0.16}_{-0.02}(\text{parton shower}) \pm^{+0.05}_{-0.03}(\text{PDF}) \text{ fb} \quad (5.29)$$

1761 Combining this **SHERPA** prediction with the measured signal strength  $\mu_{\text{obs}}$  from Equation 5.28,  
 1762 the measured fiducial cross section  $\sigma_{\text{meas}}^{\text{fid}}$  can be calculated using Equation 5.25:

$$\sigma_{\text{meas}}^{\text{fid}} = 2.91^{+0.51}_{-0.47}(\text{stat}) \pm^{+0.12}_{-0.16}(\text{theory}) \pm^{+0.24}_{-0.23}(\text{sys}) \pm^{+0.08}_{-0.06}(\text{luminosity}) \text{ fb} \quad (5.30)$$

1763 A plot comparing the measured fiducial cross section to two theoretical calculations is shown in  
 1764 Figure 5.31. The measured value is compared to the **SHERPA v2.2.2** prediction used to calculate  
 1765  $\mu_{\text{obs}}$  as well as to **POWHEG-BOX v2**. As mentioned in Section 5.1.1, this **POWHEG** sample does not  
 1766 include the resonant triboson diagrams and is only used here for a visual comparison.

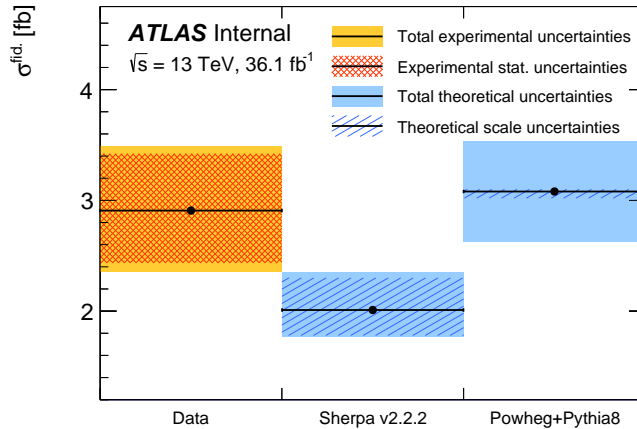


Figure 5.31: Comparison of the measured  $W^\pm W^\pm jj$  EWK fiducial cross section with theoretical calculations from **SHERPA v2.2.2** and **POWHEG-BOX v2**. The light orange band represents the total experimental uncertainty on the measured value, and the dark orange hashed band is the statistical uncertainty. For the simulations, the light blue band represents the total theoretical uncertainty, and the dark blue hashed band are the scale uncertainties. The theory predictions do not include the interference between the EWK and QCD production.

## CHAPTER 6

---

# Prospects for same-sign $WW$ at the High Luminosity LHC

---

1770 On December 3, 2018, Run 2 of the LHC officially ended, and the collider was shut down to begin  
 1771 the first of two scheduled extended maintenance periods [81]. During these two long shutdowns,  
 1772 the Phase-I and Phase-II upgrades of the LHC and ATLAS will occur in order to prepare for the  
 1773 High-Luminosity LHC (HL-LHC) which is scheduled to begin operation in 2026 [82].

1774 The HL-LHC is planned to run at a center-of-mass energy of  $\sqrt{s} = 14$  TeV with an instantaneous  
 1775 luminosity of  $\mathcal{L} = 5 \times 10^{34}$  cm $^{-2}$ s $^{-1}$  with up to 200 collisions per beam-crossing. Over the course  
 1776 of operation, the HL-LHC is expected to collect a total integrated luminosity of  $\mathcal{L} = 3000$  fb $^{-1}$  by  
 1777 2035 [83].

1778 These run conditions will be much harsher than what ATLAS has experienced so far, and there  
 1779 are several upgrades planned for the detector to operate in the high luminosity environment. Most  
 1780 notably, the entire ID will be replaced with an all-silicon tracker which will extend the coverage from  
 1781  $|\eta| \leq 2.7$  up to  $|\eta| \leq 4.0$ . This will allow for reconstruction of charged particle tracks which can  
 1782 in turn be matched to clusters in the calorimeters for electron identification or forward jet tagging  
 1783 [84].

1784 The upgraded detector, the higher beam energy, and the increased volume of data to be collected  
 1785 provides the opportunity to measure rarer processes with a much higher precision than what was  
 1786 possible in Run 1. Same-sign  $W^\pm W^\pm jj$  production, is one such process. With greater statistics,  
 1787 the accuracy of the cross section measurement can be improved over the 13 TeV analysis detailed in  
 1788 Chapter 5, and it also will allow for more detailed physics studies, such as measuring the polarization  
 1789 of the  $W$  bosons. A measurement of the longitudinal polarization of the scattered  $W$  bosons has

1790 not yet been possible, but it remains of great interest due to its sensitivity to electroweak symmetry  
 1791 breaking [85]. The analysis detailed in this chapter is based off of the 2018 ATLAS HL-LHC  
 1792  $W^\pm W^\pm jj$  prospects study [86] which extends upon the results of the previous year’s study [87].

### 1793 6.0.1 Analysis Overview

1794 The experimental signature of interest is identical to the 13 TeV analysis: two prompt leptons (either  
 1795 electrons or muons) with the same charge, missing transverse energy, and two high energy, forward  
 1796 jets. These jets are again required to have a large angular separation and a high combined invariant  
 1797 mass to preferentially select EWK- over QCD-produced  $W^\pm W^\pm jj$  events.

1798 Background processes are again similar to the 13 TeV analysis and are summarized again here.  
 1799 The dominant source of prompt background from  $WZ + \text{jets}$  events where both bosons decay lepton-  
 1800ically. If the lepton from the  $Z$ -decay with opposite charge from the  $W$  falls outside of the detector  
 1801 acceptance or is not identified, the remainder could appear to be a  $W^\pm W^\pm jj$  signal event. To a  
 1802 lesser extent,  $ZZ + \text{jets}$  events can enter the signal region in much the same way provided two lep-  
 1803 tons are “lost”. Other prompt sources include  $t\bar{t} + V$  and multiple parton interactions, however  
 1804 these processes do not contribute much. These prompt backgrounds are expected to contribute  
 1805 less than in Run 2 with the addition of forward tracking in the upgraded ATLAS detector. Jets  
 1806 mis-reconstructed as leptons or leptons from hadronic decays (such as  $t\bar{t}$  and  $W + \text{jets}$  production)  
 1807 comprise the non-prompt lepton background. Lastly, events with two prompt, opposite-charge elec-  
 1808 trons can appear as a same-sign event provided one of the electrons is mis-reconstructed as the  
 1809 wrong charge.

1810 In this analysis, the EWK production of  $W^\pm W^\pm jj$  is studied in the context of the planned  
 1811 HL-LHC run conditions and upgraded ATLAS detector. An optimized event selection (referred to  
 1812 as the *optimized selection*) is also explored in an effort to gain increased signal significance over  
 1813 the *default selection*. The cross section of the inclusive EWK production is measured for both the  
 1814 default and optimized selections, and the extraction of the longitudinal scattering significance is  
 1815 measured with the optimized selection.

## 1816 6.1 Theoretical motivation

1817 The theoretical motivation for studying the ssWW process—and VBS in general—is detailed in Sec-  
 1818 tion 5.0.2. Since it is specifically the scattering of *longitudinally polarized* vector bosons that violates

unitarity without a SM Higgs boson, a direct measurement of this cross section will be very useful for understanding how the Higgs unitarizes the process [85].

### 6.1.1 Experimental sensitivity to longitudinal polarization

**TODO:** mention that since there are so many polarization possibilities, a large integrated luminosity is needed to measure just one of them individually **TODO:** Paragraph about polarization vector and what it means physically There are three possible polarization states for a massive vector boson: two transverse (+ or -) and one longitudinal (0). Therefore, in a system with two  $W$  bosons, the overall polarization can be purely longitudinal (00), purely transverse (++, --, and +−), or mixed (+0 and −0). The three combinations will be referred to as *LL*, *TT*, and *LT* respectively.

In order extract the longitudinal scattering component, it is necessary to find variables that can help distinguish the LL from the TT and LT events. Several were studied, and those with the best discriminating power between the polarizations are the leading and subleading lepton  $p_T$  as well as the azimuthal separation ( $|\Delta\phi_{jj}|$ ) of the two VBS jets. Both leptons in LL events tend to be softer than the TT and LT events (see Figure 6.1), which motivates keeping cuts on these quantities as low as possible in the event selection. In the case of  $|\Delta\phi_{jj}|$ , the LL events generally had a larger dijet separation (see Figure 6.2), and this variable is used in a binned likelihood fit to extract the longitudinal scattering significance.

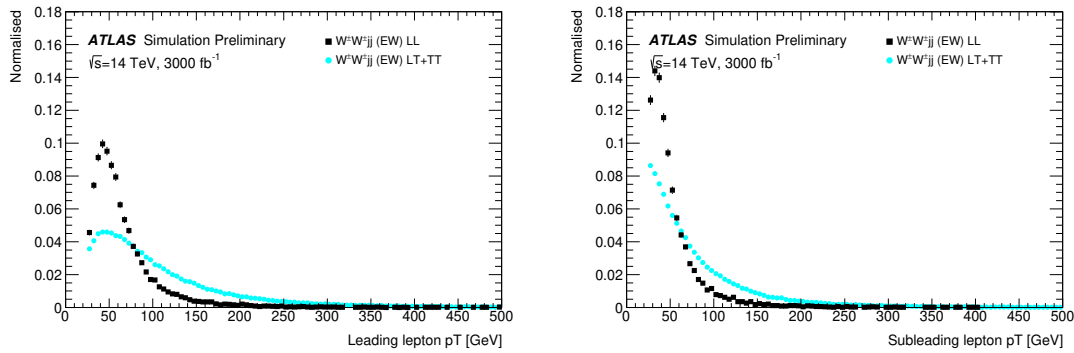


Figure 6.1: Comparison of the leading (left) and subleading (right) lepton  $p_T$  distributions for purely longitudinal (LL, black) and mixed polarization (LT+TT, cyan)  $W^{\pm}W^{\pm}jj$  events.

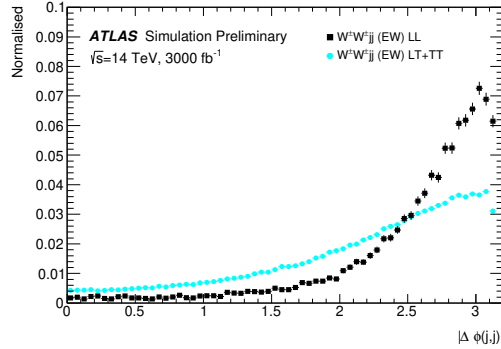


Figure 6.2: Comparison of the azimuthal dijet separation ( $|\Delta\phi_{jj}|$ ) for purely longitudinal (LL, black) and mixed polarization (LT+TT, cyan)  $W^\pm W^\pm jj$  events.

## 1836 6.2 Monte Carlo samples

1837 As no real HL-LHC data will be available for many years, all signal and background processes  
 1838 are modeled using MC simulations generated at  $\sqrt{s} = 14$  TeV, with the event yields scaled to the  
 1839 anticipated HL-LHC integrated luminosity of  $\mathcal{L} = 3000 \text{ fb}^{-1}$ . The MC samples used in the analysis  
 1840 are generated at particle-level and have not been run through the typical full simulation of the  
 1841 ATLAS detector. Instead, smearing functions derived from a **GEANT4** simulation of the upgraded  
 1842 ATLAS detector are used to estimate detector effects such as momentum resolution. In addition,  
 1843 pileup events are fully simulated. The MC samples used in this analysis are summarized in Table 6.1.

1844 The signal sample consists of both VBS and non-VBS electroweak (EWK)  $W^\pm W^\pm jj$  production,  
 1845 and it is simulated with the **Madgraph5\_aMC@NLO** generator using the **NNPDF3.0** PDF set and in-  
 1846 terfaced with **PYTHIA v8** [88] for hadronization and parton showering. To study the longitudinal  
 1847 polarization more directly, two additional **Madgraph5\_aMC@NLO**  $W^\pm W^\pm jj$  samples are used: one  
 1848 containing only the longitudinal contribution (LL) and a second containing the transverse (TT) and  
 1849 mixed (LT) contributions.

1850 There are many other processes that can produce the same final state as the  $W^\pm W^\pm jj$  and  
 1851 must also be accounted for using MC simulations.  $WZ$  events are generated using **SHERPA v2.2.0**,  
 1852 which includes up to one parton at NLO in the strong coupling constant and up to three addi-  
 1853 tional partons at LO. Both EWK and QCD production are included in these samples.  $ZZ$  and  
 1854 triboson  $VVV$  ( $V = W, Z$ ) events are generated using **SHERPA v2.2.2** with up to two additional  
 1855 partons in the final state. For the triboson backgrounds, the bosons can decay leptonically or  
 1856 hadronically.  $W+jets$  backgrounds are generated for electron, muon, and tau final states at LO

Process	Generator	Comments
$W^\pm W^\pm jj$ (EWK)	Madgraph5_aMC@NLO	Signal sample
$W^\pm W^\pm jj$ (QCD)	Madgraph5_aMC@NLO	
$W^\pm W^\pm jj$ (LL)	Madgraph5_aMC@NLO	Pure longitudinal polarization sample
$W^\pm W^\pm jj$ (TT+LT)	Madgraph5_aMC@NLO	Mixed and transverse polarization sample
Diboson	SHERPA v2.2.0	$WZ$ events
	SHERPA v2.2.2	$ZZ$ events
Triboson	SHERPA v2.2.2	
$W+jets$	Madgraph5_aMC@NLO	
$Z+jets$	POWHEG-BOX v2	
$t\bar{t}$	POWHEG-BOX	
Single top	POWHEG-BOS	

Table 6.1: Summary of MC samples used in the analysis.

1857 with Madgraph5\_aMC@NLO and the NNPDF3.0 set with showering from PYTHIA v8.  $Z+jets$  events are  
 1858 produced using POWHEG-BOX v2 and the CT10 PDF set interfaced with PYTHIA v8. Finally,  $t\bar{t}$  and  
 1859 single-top events are generated using POWHEG-BOX with showering from PYTHIA v6.

### 1860 6.3 Background estimations

1861 In this analysis, all background contributions are estimated using MC simulations. Backgrounds such  
 1862 as electron charge misidentification and fake electrons from jets (which are traditionally estimated  
 1863 using data-driven techniques) are estimated using a set of parameterization functions applied to the  
 1864 MC. These functions calculate the probability that an electron is assigned the wrong charge or a  
 1865 jet is mis-reconstructed as an electron parameterized by the  $p_T$  and  $\eta$  of the electron or jet. The  
 1866 probabilities are derived from studies on expected electron performance with the upgraded ATLAS  
 1867 detector [89].

1868 Processes involving two  $W$  and  $Z$  bosons are grouped together as *diboson* backgrounds, with the  
 1869 exception of  $W^\pm W^\pm jj$  events produced via QCD interactions, which are kept separate. Similarly,  
 1870 all backgrounds with three vector bosons are combined and labeled as *triboson*. Any  $W+jets$  or top  
 1871 events that pass selection and do not contain a fake electron, as well as any  $Z+jets$  events without an  
 1872 electron identified as having its charge misidentified are combined as *other non-prompt* backgrounds.

#### 1873 6.3.1 Truth-based isolation

1874 To properly calculate particle isolation, it requires information from several detector subsystems  
 1875 including tracking and calorimeter responses. Since the MC samples used in this analysis have not

been run through a full detector simulation, it is not possible to construct the canonical isolation variables used in analyses. At truth-level, this is generally not a serious concern as  $p_T$  signal leptons tend to be well isolated to begin with. However, isolation is one of the most powerful tools for rejecting leptons from non-prompt sources such as top events, which are produced in association with additional nearby particles from  $b$  and  $c$  quark decays. In this analysis, with the absence of any sort of isolation requirement, contributions from top backgrounds (including single top,  $t\bar{t}$  and  $t\bar{t} + V$ ) are more than an order of magnitude higher than expected.

As a result, it is necessary to find one or more quantities that are comparable to the isolation information that is available in fully-simulated samples. Analogues to track- and calorimeter-based isolation variables are constructed by summing the momentum and energy, respectively, of stable truth particles with  $p_T > 1$  GeV within a specified radius of each signal lepton. For the track-based isolation, only charged truth particles are used; both charged and neutral particles (excluding neutrinos) are included for the calorimeter-based isolation. Ultimately, a set of isolation cuts are chosen that are similar to those recommended by ATLAS for Run 2 analyses. The truth-based isolation requirements are listed in Table 6.2.

	Electron Isolation	Muon Isolation
Track-based isolation cone size	$\Delta R < 0.2$	$\Delta R < 0.3$
Track-based isolation requirement	$\sum p_T/p_T^e < 0.06$	$\sum p_T/p_T^\mu < 0.04$
Calorimeter-based isolation cone size	$\Delta R < 0.2$	$\Delta R < 0.2$
Calorimeter-based isolation requirement	$\sum E_T/p_T^e < 0.06$	$\sum E_T/p_T^\mu < 0.15$

Table 6.2: Truth-based isolation requirements for electrons and muons.

The truth-based isolation requirement reduces the top background by over 99%, and the percentage of the total background consisting of top events is reduced from 83% to 2%. Additional details on the truth-based isolation studies are presented in Appendix A.1.

## 6.4 Object and event selection

### 6.4.1 Object selection

Electrons and muons are preselected to have  $p_T > 7$  and 6 GeV, respectively, and  $|\eta| \leq 4.0$ . The likelihood of a given lepton to pass the trigger and identification requirements is estimated by calculating an efficiency dependent on the  $p_T$  and  $\eta$  of the lepton. The leptons are also required to pass the isolation criteria detailed in Table 6.2. Jets that have been tagged as a fake electron by the functions described in Section 6.3 are treated as electrons for the purpose of the object selection and

1901 are subject to the same criteria. In order to be considered a signal lepton, an additional requirement  
 1902 of  $p_T > 25$  GeV is applied on top of the preselection. The two highest  $p_T$  leptons passing this  
 1903 selection are chosen to be the leading and subleading signal leptons.

1904 Jets are clustered using the anti- $k_t$  algorithm [72] from final-state particles within a radius of  
 1905  $\Delta R = 0.4$  (excluding muons and neutrinos). Jets are required to have  $p_T > 30$  GeV and lie within  
 1906  $|\eta| < 4.5$ , with an additional cut of  $p_T > 70$  GeV for jets above  $|\eta| \geq 3.8$  in order to suppress jets  
 1907 from pileup interactions. Jets overlapping with a preselected electron within  $\Delta R(e, j) < 0.05$  are  
 1908 removed in order to prevent double counting. The two highest  $p_T$  jets are defined as the leading  
 1909 and subleading *tag jets*.

1910 **6.4.2 Event selection**

1911 The default event selection is summarized in Table 6.3 and described here. Exactly two signal  
 1912 leptons are required with the same electric charge and separated from each other by  $\Delta R(l l) > 0.3$ .  
 1913 In order to suppress contributions from Drell-Yan backgrounds, the two signal leptons must have  
 1914 an invariant mass  $m_{ll}$  greater than 20 GeV. Additionally, if both signal leptons are electrons, their  
 1915 mass must be at least 10 GeV from the  $Z$ -boson mass in order to reduce background from  $Z$ -boson  
 1916 decays<sup>18</sup>. The event is required to have at least 40 GeV of missing transverse energy ( $E_T^{\text{miss}}$ ) to  
 1917 account for the two neutrinos from the  $W$  decays. Events with additional preselected leptons are  
 1918 vetoed, which greatly reduces  $WZ$  and  $ZZ$  backgrounds.

1919 Each event must have at least two jets, and both tag jets are required to not overlap with the  
 1920 signal leptons, and there is a veto on events with one or more  $b$ -jets. In order to preferentially select  
 1921 EWK production, the tag jets are also required to have a large separation between them and a large  
 1922 invariant mass. Finally, a cut on the lepton centrality<sup>19</sup>,  $\zeta$ , defined in Equation 6.1 enhances the  
 1923 EWK  $W^\pm W^\pm jj$  signal.

$$\zeta = \min[\min(\eta_{\ell 1}, \eta_{\ell 2}) - \min(\eta_{j 1}, \eta_{j 2}), \max(\eta_{j 1}, \eta_{j 2}) - \max(\eta_{\ell 1}, \eta_{\ell 2})] \quad (6.1)$$

---

<sup>18</sup>The electron charge misidentification rate in the upgraded ATLAS detector is estimated to be high enough that contributions from  $Z \rightarrow ee$  backgrounds are non-negligible.

<sup>19</sup> $\zeta$  is a measurement of whether the two signal leptons lie between the two tagging jets in  $\eta$ , as is preferred by the VBS topology.

Selection requirement	Selection value
Lepton kinematics	$p_T > 25 \text{ GeV}$ $ \eta  \leq 4.0$
Jet kinematics	$p_T > 30 \text{ GeV}$ for $ \eta  \leq 4.5$ $p_T > 70 \text{ GeV}$ for $ \eta  > 3.8$
Dilepton charge	Exactly two signal leptons with same charge
Dilepton separation	$\Delta R_{l,l} \geq 0.3$
Dilepton mass	$m_{ll} > 20 \text{ GeV}$
$Z$ boson veto	$ m_{ee} - m_Z  > 10 \text{ GeV}$ ( $ee$ -channel only)
$E_T^{\text{miss}}$	$E_T^{\text{miss}} > 40 \text{ GeV}$
Jet selection	At least two jets with $\Delta R_{l,j} > 0.3$
$b$ jet veto	$N_{\text{b-jet}} = 0$
Dijet separation	$\Delta \eta_{jj} > 2.5$
Trilepton veto	No additional preselected leptons
Dijet mass	$m_{jj} > 500 \text{ GeV}$
Lepton-jet centrality	$\zeta > 0$

Table 6.3: Summary of the signal event selection.

## 1924 6.5 Selection optimization

1925 An upgraded detector along with an increase in center of mass energy and integrated luminosity  
 1926 provides an opportunity to study whether the event selection can be optimized to improve the signal  
 1927 to background ratio.

### 1928 6.5.1 Random grid search algorithm

1929 The chosen method for optimizing the event selection is a cut-based algorithm known as the Random  
 1930 Grid Search (RGS) [90]. Consider a simple case of two variables  $x$  and  $y$  chosen to differentiate signal  
 1931 from background. In order to be considered a signal event, a given event would be required to pass  
 1932 a set of selection criteria, called a *cut point*:  $c = \{x > x_c, y > y_c\}$ . A simple method to choose the  
 1933 optimal cut point (i.e. the “best” values of the cuts  $x_c$  and  $y_c$ ) would be to construct an  $n \times m$   
 1934 rectangular grid in  $x$  and  $y$  consisting of points  $(x_0, y_0), (x_1, y_1), \dots, (x_n, y_m)$ , as in the left plot of  
 1935 Figure 6.3. One can then choose a cut point  $c_k = \{x > x_i, y > y_j\}$  that maximizes the signal  
 1936 significance as measured by a chosen metric. This would be considered a *rectangular grid search*.

1937 While effective in principle, a rectangular grid search comes with two major drawbacks:

- 1938 1. The algorithm scales exponentially as the number of variables to be optimized increases, as  
 1939 this is effectively increasing the dimensionality of the grid. In the simple case of a square grid  
 1940 with  $N$  bins per variable  $v$ , the number of cut points to be evaluated grows as  $N^v$ .

1941     2. Signal and background samples are rarely evenly distributed over the entire grid, resulting  
 1942       in many cut points being sub-optimal and evaluating them would be a waste of computing  
 1943       resources.

1944     To combat these limitations, the RGS algorithm constructs a grid of cut points directly from  
 1945       the signal sample itself. In the two-dimensional example, this means that the variables  $x_i$  and  $y_j$   
 1946       making up the cut point  $c_k = \{x > x_i, y > y_j\}$  take their values directly from a given signal event.  
 1947     This has the benefit of creating a *random grid* of cut points that is biased towards regions of high  
 1948       signal concentration by construction. This reduces the need for exponentially increasing numbers of  
 1949       cut points while ensuring that computing resources are not wasted in regions with few to no signal  
 1950       events. An example of a two-dimensional random grid is shown in the right-hand plot in Figure 6.3.

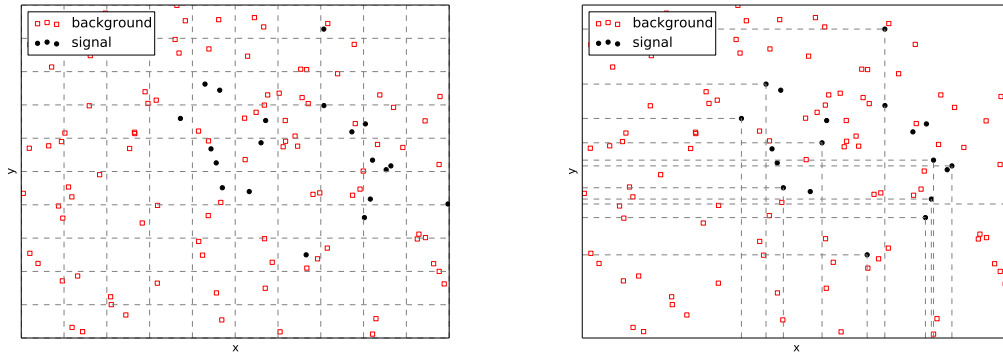


Figure 6.3: A visual representation of a two-dimensional rectangular grid (left) and a random grid (right) in variables  $x$  and  $y$ . The signal events are the black circles, and the red squares are the background events. Each intersection of gray dashed lines represents a cut point to be evaluated by the optimization.

1951     Once the random grid of cut points is constructed, the optimal cut point can be chosen using any  
 1952       number of metrics, such as signal to background ratio. For the purpose of the  $W^\pm W^\pm jj$  upgrade  
 1953       study, the optimal cut point is chosen to be the one that maximizes the signal significance  $Z$  as  
 1954       defined in Equation 6.2 [91].

$$Z = \sqrt{2 \left[ (s + b) \ln \left( \frac{s + b}{b_0} \right) + b_0 - s - b \right] + \frac{(b - b_0)^2}{\sigma_b^2}} \quad (6.2)$$

1955     where  $s$  and  $b$  are the number of signal and background events, respectively,  $\sigma_b$  is the total uncertainty  
 1956       on the background, and  $b_0$  is defined as:

$$b_0 = \frac{1}{2} \left( b - \sigma_b^2 + \sqrt{(b - \sigma_b^2)^2 + 4(s + b)\sigma_b^2} \right) \quad (6.3)$$

1957 In the case where the background is known precisely (i.e.  $\sigma_b = 0$ ), Equation 6.2 simplifies to

$$Z = \sqrt{2 \left( b[(1 + s/b) \ln(1 + s/b) - s/b] \right)} \quad (6.4)$$

1958 which further reduces to the familiar  $Z = s/\sqrt{b}$  for the case when  $s \ll b$ .

### 1959 6.5.2 Inputs to the optimization

1960 In order to train the RGS, signal and background samples are prepared from events passing the  
 1961 event selection outlined in Table 6.3 up through the  $b$ -jet veto. The signal sample is chosen to be  
 1962 the longitudinally polarized  $W^\pm W^\pm jj$  EWK events, and the transverse and mixed polarizations  
 1963 are treated as background along with  $W^\pm W^\pm jj$  events from QCD interactions and the traditional  
 1964 backgrounds listed in Section 6.3. Splitting the inclusive  $W^\pm W^\pm jj$  EWK events by polarization  
 1965 allows the optimization to favor the longitudinally polarized events as much as possible, even though  
 1966 they both contribute to the EWK signal.

1967 The following variables are chosen for optimization:

- 1968 • Leading lepton  $p_T$
- 1969 • Dilepton invariant mass ( $m_{ll}$ )
- 1970 • Leading and subleading jet  $p_T$
- 1971 • Dijet invariant mass ( $m_{jj}$ )
- 1972 • Lepton-jet centrality ( $\zeta$ )

1973 Subleading lepton  $p_T$  is omitted as it is desirable to keep the cut value as low as possible due to  
 1974 its sensitivity to the longitudinal polarization (as discussed in Section 6.1.1). Additionally, the dijet  
 1975 separation  $\Delta\eta_{jj}$  was included in the optimization originally, however it was dropped from the list due  
 1976 to the cut value being motivated by differences between EWK and QCD produced  $W^\pm W^\pm jj$  events.

1977 Two additional constraints were imposed when selecting the optimal cut point:

- 1978 1. At least 1000 signal events must survive in order to prevent the optimization from being too  
 1979 aggressive and unnecessarily reducing signal statistics.
- 1980 2. The dijet invariant mass may only vary within a 50 GeV range of the default value (from  
 1981 450 – 550 GeV) due to the cut being physically motivated by the VBS event topology (see  
 1982 Section 5.0.3).

1983     Lastly, the signal significance is calculated without taking into account the uncertainty of the  
 1984 background using Equation 6.4. This is due to the fact that the statistical uncertainties of the fake  
 1985 electron and charge misidentification backgrounds are quite large, owing to poor MC statistics in a  
 1986 few of the samples. If Equation 6.2 were used instead, the optimization will cut unreasonably hard  
 1987 against these backgrounds. Since Monte Carlo statistics is not expected to be a limiting factor when  
 1988 this analysis is performed at the HL-LHC, it is more realistic to simply ignore these large statistical  
 1989 uncertainties for the purpose of the optimization.

### 1990 6.5.3 Results of the optimization

1991     Ultimately, the random grid is constructed from over 38,000 LL-polarized  $W^\pm W^\pm jj$  events in the  
 1992 six variables listed above. After applying the constraints, the optimal cut point reduces the total  
 1993 background from 9900 to 2310 while reducing the signal from 3489 to 2958. This corresponds to  
 1994 an increase in signal significance from  $Z = 33.26$  to  $Z = 52.63$  as calculated by Equation 6.4. The  
 1995 updates to the event selection are listed in Table 6.4.

1996     The large reduction in the background is primarily a result of the increase in the leading and  
 1997 subleading jet  $p_T$  from 30 GeV to 90 GeV and 45 GeV, respectively. As can be seen in Figure 6.4,  
 1998 this increase removes a significant portion of the backgrounds from jets faking electrons and charge  
 1999 mis-ID. Additionally, the loosening of the lepton-jet centrality cut  $\zeta$  allows more signal events to  
 2000 survive the event selection (see Figure 6.5). Other changes to the event selection are minor and  
 2001 do not individually have a large impact on the signal or background yields; similar distributions of  
 2002 these variables are shown in Appendix A.2.

2003     The full event yields after optimization as well as the cross section measurement are detailed  
 2004 alongside those using the default selection in Section 6.6.

Selection requirement	Selection value
Lepton kinematics	$p_T > 28$ GeV (leading lepton only)
Jet kinematics	$p_T > 90$ GeV (leading jet) $p_T > 45$ GeV (subleading jet)
Dilepton mass	$m_{ll} > 28$ GeV
Dijet mass	$m_{jj} > 520$ GeV
Lepton-jet centrality	$\zeta > -0.5$

Table 6.4: Updates to the  $W^\pm W^\pm jj$  event selection criteria after optimization. Cuts not listed remain unchanged from the default selection in Table 6.3.

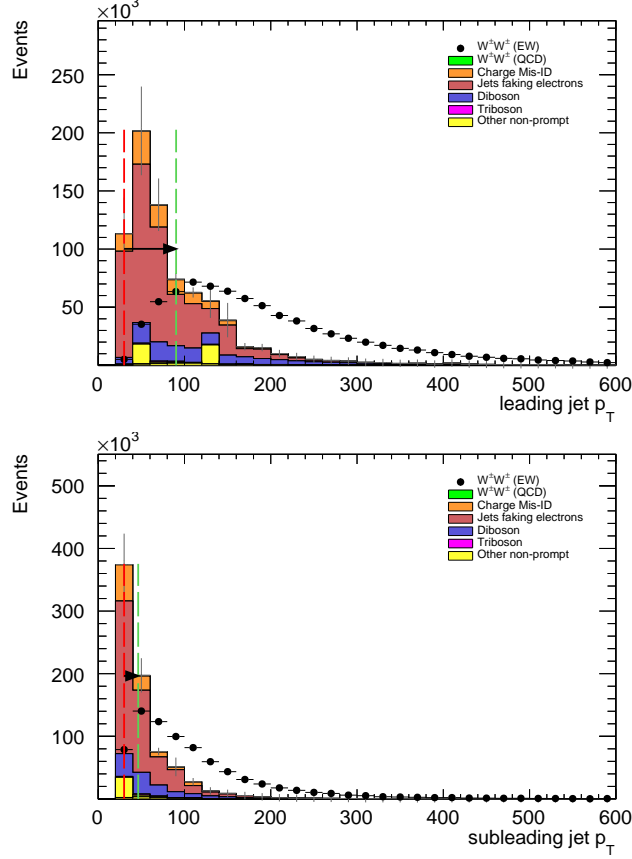


Figure 6.4: Leading (top) and subleading (bottom) jet  $p_T$  distributions. The default and optimized cuts are represented by the red and green dashed lines, respectively. The  $W^{\pm}W^{\pm} jj$  EWK signal (black points) is normalized to the same area as the sum of the backgrounds (colored histogram).

## 6.6 Results

### 6.6.1 Event yields

After applying the full event selection, the analysis is broken down into four channels based off of the flavor of the signal leptons:  $\mu\mu$ ,  $ee$ ,  $\mu e$ , and  $e\mu$ . The full signal and background event yields are shown in Table 6.5 for each channel separately and combined using the default event selection. 3489 EWK  $W^{\pm}W^{\pm} jj$  events are expected compared to 9900 background events. The dominant sources of background are jets faking electrons followed by charge misidentification and diboson processes. Triboson events, QCD  $W^{\pm}W^{\pm} jj$ , and other non-prompt sources make up approximately 5% of the total background combined.

The event yields for the optimized selection detailed in Section 6.5.3 are listed in Table 6.6. After

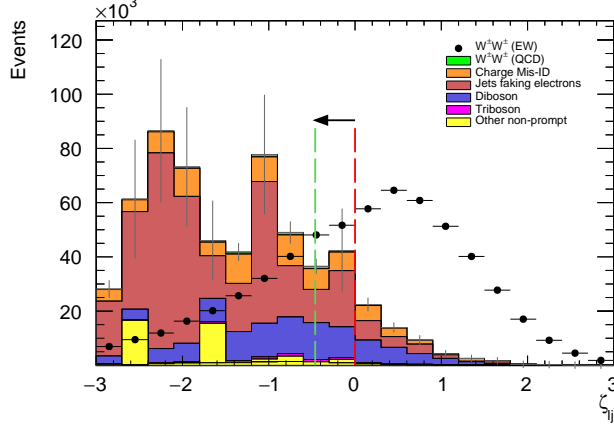


Figure 6.5: Lepton-jet centrality distribution. The default and optimized cuts are represented by the red and green dashed lines, respectively. The  $W^\pm W^\pm jj$  EWK signal (black points) is normalized to the same area as the sum of the backgrounds (colored histogram).

	All channels	$\mu\mu$	$ee$	$\mu e$	$e\mu$
$W^\pm W^\pm jj$ (QCD)	206.4	91.1	22.8	38.4	54.1
Charge Misidentification	2300	0.0	2100	90	160
Jets faking electrons	5000	0.0	3400	1200	340
$WZ + ZZ$	2040	500	438	423	680
Tribosons	115	47	15.4	21.6	31.2
Other non-prompt	210	110	20	60	27
Total Background	9900	750	6000	1900	1290
Signal $W^\pm W^\pm jj$ (EWK)	3489	1435	432	679	944

Table 6.5: Signal and background event yields using the default event selection for an integrated luminosity of  $\mathcal{L} = 3000 \text{ fb}^{-1}$ . Events containing a fake or charge-flipped electron are removed from their respective sources and combined into a single entry each.

optimization, 2958 signal events and just 2310 background events are expected. Diboson events are now the primary source of background, as the optimization greatly reduces the fake and charge misidentification backgrounds. As discussed earlier, the increase in the leading and subleading jet  $p_T$  cuts as well as the loosening of the centrality cut are most responsible for the changes in the signal and background yields; distributions of these quantities using the default and the optimized event selections can be found in Figures 6.6, 6.7, and 6.8, respectively.

It is important to note, however, that the MC sample used to estimate  $Z+jets$  events suffers from poor statistics which results in large per-event weights once scaled to  $\mathcal{L} = 3000 \text{ fb}^{-1}$ . This sample contributes heavily to the fake and charge misidentification backgrounds, and a handful of these events being cut out by the optimization contributes has a large effect on the dramatic reduction

	All channels	$\mu\mu$	$ee$	$\mu e$	$e\mu$
$W^\pm W^\pm jj$ (QCD)	168.7	74.6	19.7	32.2	42.2
Charge Misidentification	200	0.0	11	30	160
Jets faking electrons	460	0.0	130	260	70
$WZ + ZZ$	1286	322	289	271	404
Tribosons	76	30.1	9.6	15.1	21.6
Other non-prompt	120	29	16.6	50	19
Total Background	2310	455	480	660	710
Signal $W^\pm W^\pm jj$ (EWK)	2958	1228	380	589	761

Table 6.6: Signal and background event yields using the optimized event selection for an integrated luminosity of  $\mathcal{L} = 3000 \text{ fb}^{-1}$ . Events containing a fake or charge-flipped electron are removed from their respective sources and combined into a single entry each.

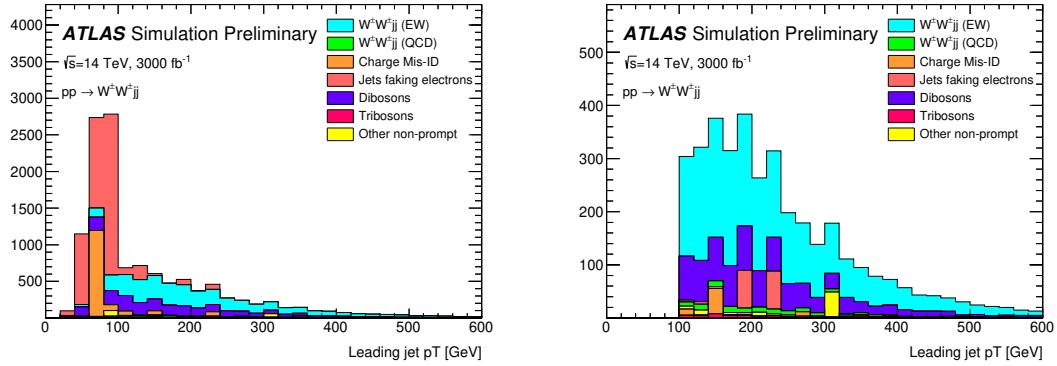


Figure 6.6:  $p_T$  distributions for the leading jet using the default (left) and optimized (right) event selections for all channels combined.

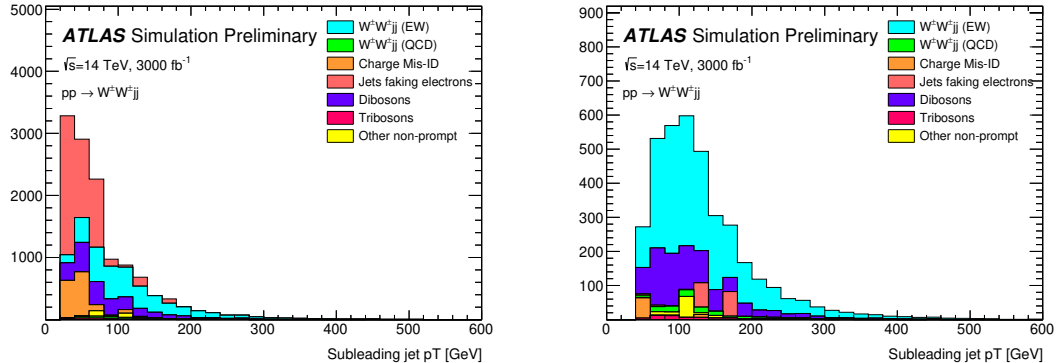


Figure 6.7:  $p_T$  distributions for the subleading jet using the default (left) and optimized (right) event selections for all channels combined.

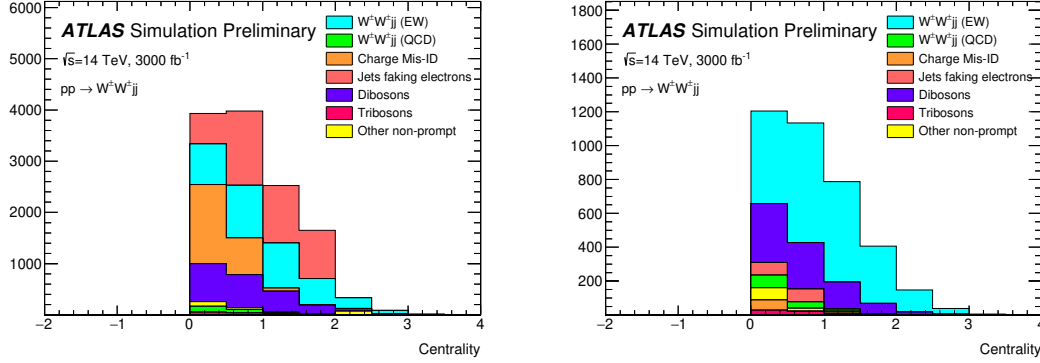


Figure 6.8:  $p_T$  distributions for lepton-jet centrality  $\zeta$  using the default (left) and optimized (right) event selections for all channels combined.

of these backgrounds. As a result, these particular optimized results are likely overly optimistic. However, given proper MC statistics, it is still expected that the optimization will outperform the default selection.

### 6.6.2 Uncertainties

**TODO:** Ask for details on how some of these uncertainties were calculated – specifically the fakes and charge mis-ID The uncertainties considered for the analysis are summarized in Table 6.7. Values for experimental systematics on the trigger efficiency, lepton and jet reconstruction, and flavor tagging are taken directly from the 13 TeV analysis [45]. The rate uncertainties for the background processes are halved from the 13 TeV values.

Source	Uncertainty (%)
$W^\pm W^\pm jj$ (EWK)	3
Luminosity	1
Trigger efficiency	0.5
Lepton reconstruction and identification	1.8
Jets	2.3
Flavor tagging	1.8
Jets faking electrons	20
Charge misidentification	25
$W^\pm W^\pm jj$ (QCD)	20
Top	15
Diboson	10
Triboson	15

Table 6.7: Summary of estimated experimental and rate uncertainties.

2034 **6.6.3 Cross section measurement**

2035 The cross section is calculated using the same method as in the 13 TeV analysis, detailed in Sec-  
 2036 tion 5.4. Unlike the previous analysis, however, eight lepton channels are used here instead of six.  
 2037 The  $\mu e$  and  $e\mu$  channels remain separated in addition to the  $\mu\mu$  and  $ee$  channels, and each lepton  
 2038 flavor channel is further split by charge (i.e.  $\mu\mu \rightarrow \mu^+\mu^+ + \mu^-\mu^-$ ), as this increases the sensitivity  
 2039 of the analysis. Each channel's  $m_{jj}$  distribution is combined in a profile likelihood fit to extract the  
 2040 EWK  $W^\pm W^\pm jj$  production cross section. The expected cross section calculated using the default  
 2041 event selection is:

$$\sigma_{W^\pm W^\pm jj}^{\text{expected}} = 16.89 \pm 0.36 \text{ (stat)} \pm 0.53 \text{ (theory)} \pm 0.84 \text{ (syst)} \text{ fb} \quad (6.5)$$

2042 The expected cross section calculated using the optimized event selection is:

$$\sigma_{W^\pm W^\pm jj}^{\text{expected}} = 16.94 \pm 0.36 \text{ (stat)} \pm 0.53 \text{ (theory)} \pm 0.78 \text{ (syst)} \text{ fb} \quad (6.6)$$

2043 The optimized selection should not change the measured value of the cross section, and indeed both  
 2044 are consistent with within uncertainties. The systematic uncertainty is reduced by approximately 7%  
 2045 with the optimized selection. Projections of the total uncertainty on the cross section as a function  
 2046 of integrated luminosity made by **TODO: how was this made?** is shown in Figure 6.9. As the  
 2047 integrated luminosity increases past  $\mathcal{L} > 3000 \text{ fb}^{-1}$ , the statistical uncertainty reduces faster than  
 2048 the systematic uncertainties. However, the total uncertainty is expected to reduce by less than a  
 2049 percent with increased luminosity past the planned  $3000 \text{ fb}^{-1}$ .

2050 **6.6.4 Longitudinal scattering significance**

2051 The longitudinal scattering significance is extracted in much the same way as the cross section, this  
 2052 time using a binned likelihood fit on the  $|\Delta\phi_{jj}|$  distribution. In order to increase sensitivity, the  
 2053  $|\Delta\phi_{jj}|$  distribution is split into two bins in  $m_{jj}$ , and an additional cut on the pseudorapidity of the  
 2054 subleading lepton is applied ( $|\eta| < 2.5$ ) to reduce background from fake and charge misidentification.  
 2055 The  $|\Delta\phi_{jj}|$  distributions used in the fit are shown in Figure 6.10. Due to limited statistics, the four  
 2056 lepton flavor channels are not split by charge. The expected significance of the  $W_L^\pm W_L^\pm jj$  process  
 2057 is  $1.8\sigma$  with a precision of 47% on the measurement. Projections of the expected significance as a  
 2058 function of integrated luminosity is shown in Figure 6.11.

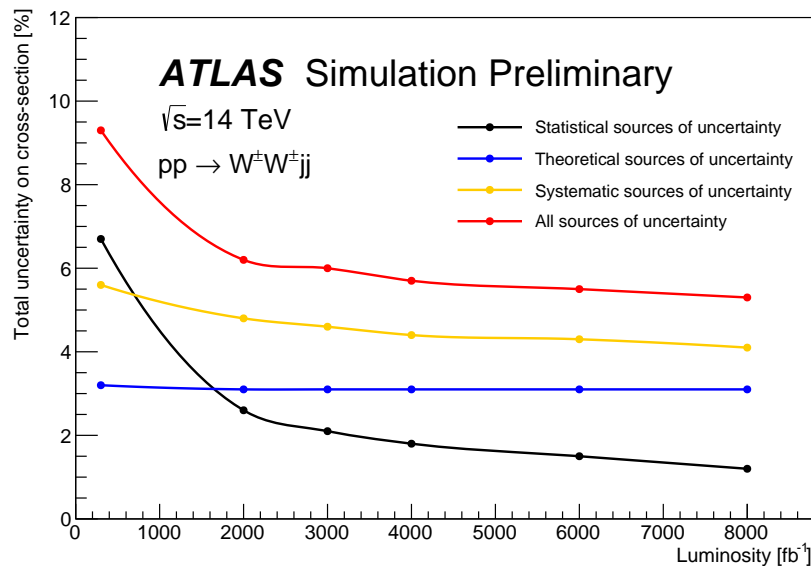


Figure 6.9: Projections of the statistical (black), theoretical (blue), systematic (yellow), and total (red) uncertainties on the measured cross section as a function of integrated luminosity using the optimized event selection.

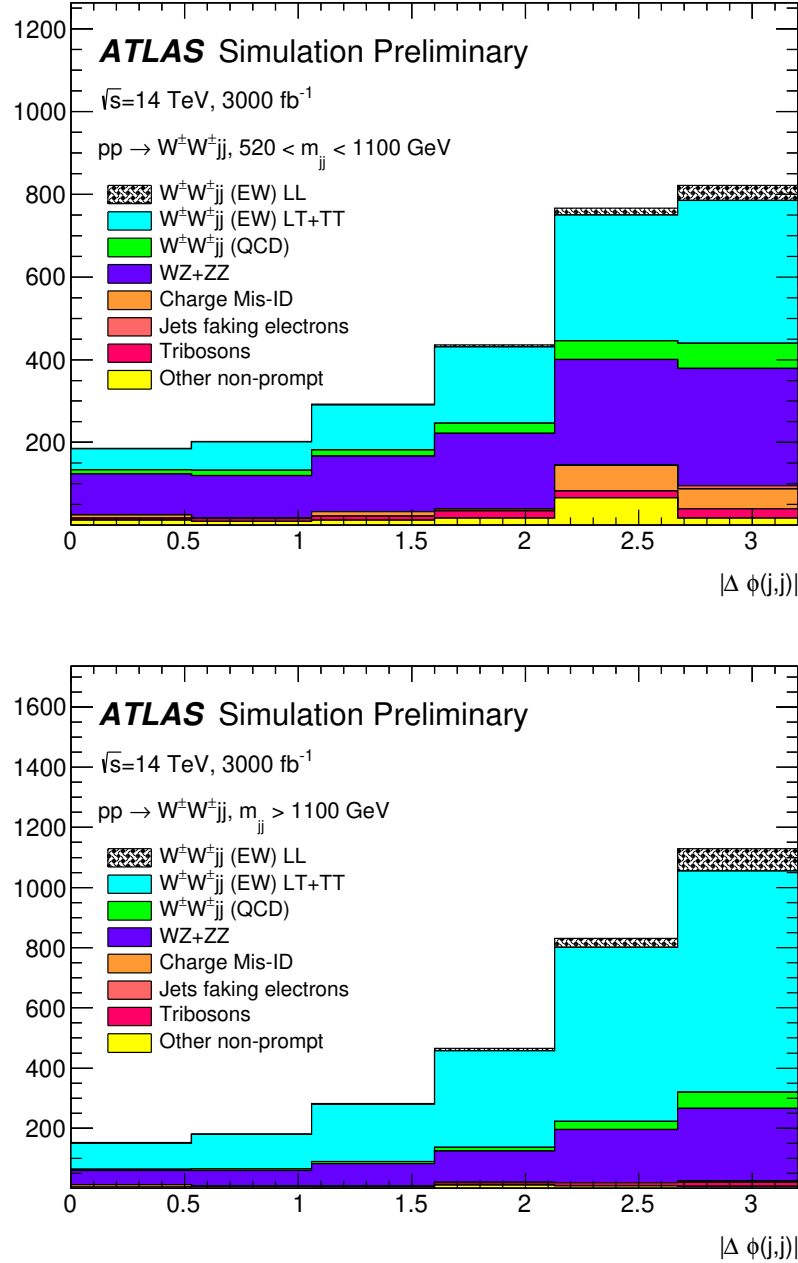


Figure 6.10: Dijet azimuthal separation ( $|\Delta\phi_{jj}|$ ) for the low  $m_{jj}$  region ( $520 < m_{jj} < 1100 \text{ GeV}$ , top) and the high  $m_{jj}$  region ( $m_{jj} > 1100 \text{ GeV}$ , bottom). The purely longitudinal (LL, gray) is plotted separately from the mixed and transverse (LT+TT, cyan) polarizations.

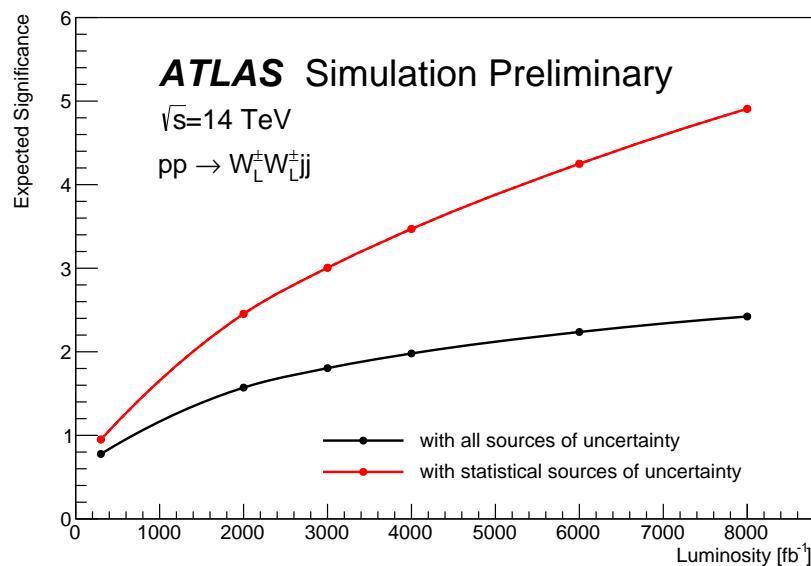


Figure 6.11: Projections of the expected longitudinal scattering significance as a function of integrated luminosity when considering all sources of uncertainties (black) or only statistical uncertainties (red).

2059

## CHAPTER 7

---

2060

## Conclusion

---

2061 Here's where you wrap it up.

2062 **Looking Ahead**

2063

2064 Here's an example of how to have an "informal subsection".

2065

## APPENDIX A

2066

2067

# Additional material on $W^\pm W^\pm jj$ prospects at the HL-LHC

2068

## A.1 Truth isolation

yields by type	all channels	$\mu\mu$	$ee$	$\mu e$	$e\mu$
signal	4011	1583.2	531.7	793.1	1103.1
ww qcd	252.6	105.8	30.4	48	68.4
charge flip	2528.4	0.0	2075.4	255.1	197.8
fakes	7135.4	0.0	4675.1	1904.3	555.9
diboson	2370.4	581.2	491.8	517.9	779.6
triboson	125.5	49.1	17.8	24.6	34.1
top	90150.5	26618	15301.6	25277.9	22953.1
z+jets	241.2	0.0	0.0	0.0	241.2
w+jets	31.4	3.9	7.6	13.2	6.7
total bkg	102803.9	27354	22592	28027.8	24830.1
signal	4011	1583.2	531.7	793.1	1103.1

Table A.1: Event yields prior to applying any form of truth-based isolation criteria.

2069

TODO: Add tables for tight vs loose working point, information on the necessity of TRUTH1++

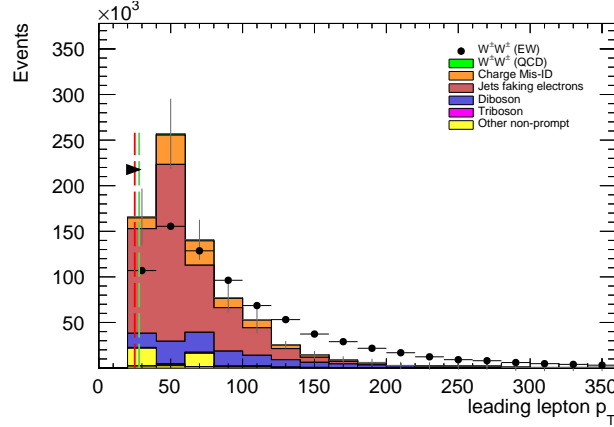
yields by type	all channels	$\mu\mu$	$ee$	$\mu e$	$e\mu$
signal	3470.5	1427.3	428.8	675.8	938.7
ww qcd	205.8	90.8	22.7	38.3	54
charge flip	2398.3	0.0	2104.6	95.8	197.9
fakes	4309.7	0.0	3390.6	750.8	168.3
diboson	1552.4	311.3	355.6	346.8	538.7
triboson	115	46.8	15.4	21.6	31.2
top	156.9	42.3	14.8	76.6	23.3
$z+jets$	0.0	0.0	0.0	0.0	0.0
$w+jets$	0.3	0.0	0.0	0.3	0.0
total bkg	8738.1	491.3	5903.7	1329.8	1013.4
signal	3470.5	1427.3	428.8	675.8	938.7

Table A.2: Event yields after applying a test version of the truth-based isolation.

2070 

## A.2 Plots of other optimization variables

2071 Plots of the remaining optimization variables not shown in Section 6.5.3 are presented here for  
 2072 reference. Figures A.1, A.2, and A.3 compare signal and background distributions for the default  
 2073 and optimized cuts. None of these cuts change by much in the optimized selection and their impacts  
 2074 on the overall event selection is minimal.

Figure A.1: Leading lepton  $p_T$  distribution. The default and optimized cuts are represented by the red and green dashed lines, respectively. The  $W^\pm W^\pm jj$  EWK signal (black points) is normalized to the same area as the sum of the backgrounds (colored histogram).

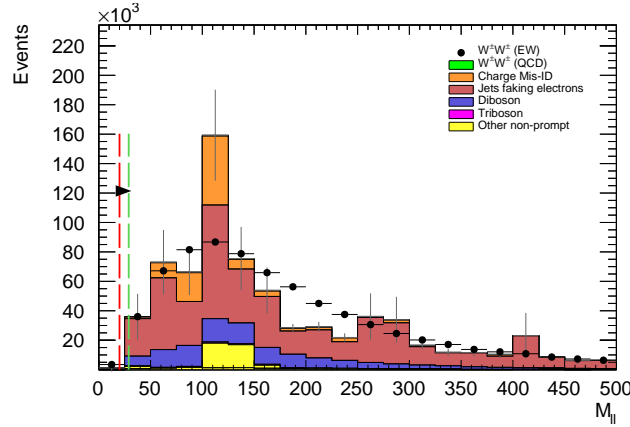


Figure A.2: Dilepton invariant mass distribution. The default and optimized cuts are represented by the red and green dashed lines, respectively. The  $W^\pm W^\pm jj$  EWK signal (black points) is normalized to the same area as the sum of the backgrounds (colored histogram).

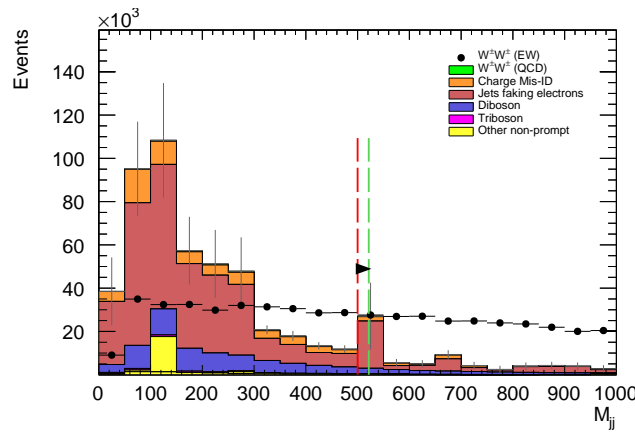


Figure A.3: Dijet invariant mass distribution. The default and optimized cuts are represented by the red and green dashed lines, respectively. The  $W^\pm W^\pm jj$  EWK signal (black points) is normalized to the same area as the sum of the backgrounds (colored histogram).

2075

## APPENDIX B

2076

2077

---

# Additional material on $W^\pm W^\pm jj$ measurement at $\sqrt{s} = 13$ TeV

---

2078 

## B.1 Impact of experimental uncertainty on MC background estimations

2079 Tables B.1-B.6 contain the impact of experimental systematic uncertainties for the remaining back-  
 2080 grounds estimated from MC simulation. The  $W^\pm W^\pm jj$  EWK signal and  $WZ$  background sys-  
 2081 tematics are listed in the main body of the document, in Tables 5.21 and 5.22, respectively. While the  
 2082 percentage of the contributions for some systematics appear large, the size of these backgrounds are  
 2083 quite small compared to the total background.

$W^\pm W^\pm jj$ QCD	$ee$ % Yield	$e\mu$ % Yield	$\mu\mu$ % Yield
Jet-related Uncertainties	3.41	3.04	2.85
b-tagging efficiency	2.56	2.48	2.48
Pile-up	4.99	0.45	0.33
Trigger efficiency	0.02	0.08	0.41
Lepton reconstruction/ID	1.62	1.19	1.89
MET reconstruction	0.41	0.22	0.34

Table B.1: Impact of experimental uncertainties for the  $W^\pm W^\pm jj$  QCD processes in all channels.

Triboson	$ee$ % Yield	$e\mu$ % Yield	$\mu\mu$ % Yield
Jet-related Uncertainties	13.09	13.39	16.85
b-tagging efficiency	2.96	3.77	4.95
Pile-up	19.37	24.66	6.87
Trigger efficiency	0.02	0.07	0.47
Lepton reconstruction/ID	1.66	1.27	2.48
MET reconstruction	0.00	0.46	0.00

Table B.2: Impact of experimental uncertainties for triboson process in all channels.

$t\bar{t}V$	$ee$ % Yield	$e\mu$ % Yield	$\mu\mu$ % Yield
Jet-related Uncertainties	17.65	11.97	14.27
b-tagging efficiency	15.02	9.04	13.83
Pile-up	8.73	10.69	4.18
Trigger efficiency	0.03	0.08	0.39
Lepton reconstruction/ID	2.57	3.27	2.66
MET reconstruction	1.75	4.16	1.62

Table B.3: Impact of experimental uncertainties for  $t\bar{t}V$  processes in all channels.

$W\gamma$	$ee$ % Yield	$e\mu$ % Yield	$\mu\mu$ % Yield
Jet-related Uncertainties	7.05	33.36	—
b-tagging efficiency	1.97	2.94	—
Pile-up	4.11	14.17	—
Trigger efficiency	0.01	0.14	—
Lepton reconstruction/ID	1.40	1.13	—
MET reconstruction	0.00	0.00	—

Table B.4: Impact of experimental uncertainties for the  $W\gamma$  process in all channels.

$Z\gamma$	$ee$ % Yield	$e\mu$ % Yield	$\mu\mu$ % Yield
Jet-related Uncertainties	16.22	370.44	—
b-tagging efficiency	1.08	3.10	—
Pile-up	12.57	11.51	—
Trigger efficiency	0.02	0.07	—
Lepton reconstruction/ID	1.26	22.01	—
MET reconstruction	0.00	0.00	—

Table B.5: Impact of experimental uncertainties for the  $Z\gamma$  process in all channels.

$ZZ$	$ee$ % Yield	$e\mu$ % Yield	$\mu\mu$ % Yield
Jet-related Uncertainties	15.71	15.76	35.18
b-tagging efficiency	2.23	2.35	2.89
Pile-up	1.22	3.20	4.58
Trigger efficiency	0.03	0.10	0.36
Lepton reconstruction/ID	3.59	3.10	5.70
MET reconstruction	4.84	3.26	3.24

Table B.6: Impact of experimental uncertainties for the  $ZZ$  process in all channels.

2084 **B.2 Additional signal region plots**

---

## Bibliography

---

- 2086 [1] ATLAS Collaboration, M. Aaboud et al., *Measurement of the  $W^\pm Z$  boson pair-production*  
 2087 *cross section in  $pp$  collisions at  $\sqrt{s} = 13$  TeV with the ATLAS Detector*, *Phys. Lett.* **B762**  
 2088 (2016) 1–22, [arXiv:1606.04017 \[hep-ex\]](#). (document)
- 2089 [2] S. Weinberg, *The Quantum Theory of Fields, Volume 1: Foundations*. Cambridge University  
 2090 Press, 1995. [2.1](#)
- 2091 [3] M. E. Peskin and D. V. Schroeder, *An Introduction to Quantum Field Theory*.  
 2092 Addison-Wesley, 1995. [2.1](#)
- 2093 [4] R. P. Feynman, *Mathematical formulation of the quantum theory of electromagnetic*  
 2094 *interaction*, *Phys. Rev.* **80** (1950) 440–457. [2.1](#)
- 2095 [5] M. Y. Han and Y. Nambu, *Three-triplet model with double SU(3) symmetry*, *Phys. Rev.* **139**  
 2096 (1965) B1006–B1010. [2.1](#)
- 2097 [6] D. J. Gross and F. Wilczek, *Asymptotically Free Gauge Theories - I*, *Phys. Rev.* **D8** (1973)  
 2098 3633–3652. [2.1](#)
- 2099 [7] D. J. Gross and F. Wilczek, *ASYMPTOTICALLY FREE GAUGE THEORIES. 2.*, *Phys.*  
 2100 *Rev.* **D9** (1974) 980–993. [2.1](#)
- 2101 [8] H. D. Politzer, *Reliable Perturbative Results for Strong Interactions?*, *Phys. Rev. Lett.* **30**  
 2102 (1973) 1346–1349. [,274(1973)]. [2.1](#)
- 2103 [9] A. Salam and J. C. Ward, *Weak and Electromagnetic Interactions*, *Nuovo Cimento* **11** (1959)  
 2104 568–577. [2.1](#)
- 2105 [10] S. L. Glashow, *The Renormalizability of Vector Meson Interactions*, *Nucl. Phys.* **10** (1959)  
 2106 107–117. [2.1](#)
- 2107 [11] ALEPH, DELPHI, L3, OPAL, SLD, LEP Electroweak Working Group, SLD Electroweak  
 2108 Group, SLD Heavy Flavour Group Collaboration, S. Schael et al., *Precision electroweak*  
 2109 *measurements on the  $Z$  resonance*, *Phys. Rept.* **427** (2006) 257–454, [arXiv:hep-ex/0509008](#)  
 2110 [hep-ex]. [2.1](#)
- 2111 [12] F. Englert and R. Brout, *Broken symmetry and the mass of gauge vector mesons*, *Phys. Rev.*  
 2112 *Lett.* **13** (1964) 321–323. [2.1](#)

- 2113 [13] P. W. Higgs, *Broken symmetries, massless particles and gauge fields*, *Physics Letters* **12**  
 2114 (1964) 132–133. 2.1
- 2115 [14] P. W. Higgs, *Broken symmetries and the masses of gauge bosons*, *Phys. Rev. Lett.* **13** (1964)  
 2116 508–509. 2.1
- 2117 [15] ATLAS Collaboration, *Observation of a new particle in the search for the Standard Model*  
 2118 *Higgs boson with the ATLAS detector at the LHC*, *Phys. Lett. B* **716** (2012) 1,  
 2119 [arXiv:1207.7214 \[hep-ex\]](https://arxiv.org/abs/1207.7214). 2.1, 5.0.2
- 2120 [16] CMS Collaboration, *Observation of a new boson at a mass of 125 GeV with the CMS*  
 2121 *experiment at the LHC*, *Phys. Lett. B* **716** (2012) 30, [arXiv:1207.7235 \[hep-ex\]](https://arxiv.org/abs/1207.7235). 2.1, 5.0.2
- 2122 [17] UA1 Collaboration, G. Arnison et al., *Experimental Observation of Isolated Large Transverse*  
 2123 *Energy Electrons with Associated Missing Energy at  $s^{**}(1/2) = 540\text{-GeV}$* , *Phys. Lett. B* **122**  
 2124 (1983) 103–116. [,611(1983)]. 2.2
- 2125 [18] UA1 Collaboration, G. Arnison et al., *Experimental Observation of Lepton Pairs of Invariant*  
 2126 *Mass Around  $95\text{-GeV}/c^{**2}$  at the CERN SPS Collider*, *Phys. Lett. B* **126** (1983) 398–410.  
 2127 [,7.55(1983)]. 2.2
- 2128 [19] Particle Data Group Collaboration, K. A. Olive et al., *Review of Particle Physics*, *Chin.*  
 2129 *Phys. C* **38** (2014) 090001. 2.2, 2.2
- 2130 [20] ATLAS Collaboration, G. Aad et al., *Evidence of  $W\gamma\gamma$  Production in  $pp$  Collisions at*  
 2131  *$\sqrt{s} = 8\text{ TeV}$  and Limits on Anomalous Quartic Gauge Couplings with the ATLAS Detector*,  
 2132 *Phys. Rev. Lett.* **115** (2015) no. 3, 031802, [arXiv:1503.03243 \[hep-ex\]](https://arxiv.org/abs/1503.03243). 2.3
- 2133 [21] ATLAS Collaboration, ATLAS Collaboration, *Evidence for Electroweak Production*  
 2134 *of  $W^\pm W^\pm jj$  in  $pp$  Collisions at  $\sqrt{s} = 8\text{ TeV}$  with the ATLAS Detector*, *Phys. Rev. Lett.* **113**  
 2135 (2014) no. 14, 141803, [arXiv:1405.6241 \[hep-ex\]](https://arxiv.org/abs/1405.6241). 2.3, 5
- 2136 [22] A. Falkowski, M. Gonzalez-Alonso, A. Greljo, D. Marzocca, and M. Son, *Anomalous Triple*  
 2137 *Gauge Couplings in the Effective Field Theory Approach at the LHC*, *JHEP* **02** (2017) 115,  
 2138 [arXiv:1609.06312 \[hep-ph\]](https://arxiv.org/abs/1609.06312). 2.3
- 2139 [23] B. W. Lee, C. Quigg, and H. B. Thacker, *Weak Interactions at Very High-Energies: The Role*  
 2140 *of the Higgs Boson Mass*, *Phys. Rev. D* **16** (1977) 1519. 2.3
- 2141 [24] D. R. Green, P. Meade, and M.-A. Pleier, *Multiboson interactions at the LHC*, *Rev. Mod.*  
 2142 *Phys.* **89** (2017) no. 3, 035008, [arXiv:1610.07572 \[hep-ex\]](https://arxiv.org/abs/1610.07572). 2.3
- 2143 [25] L. R. Evans and P. Bryant, *LHC Machine*, *JINST* **3** (2008) S08001.  
 2144 <https://cds.cern.ch/record/1129806>. This report is an abridged version of the LHC  
 2145 Design Report (CERN-2004-003). 3.1
- 2146 [26] ATLAS Collaboration, *The ATLAS Experiment at the CERN Large Hadron Collider*, *JINST*  
 2147 **3** (2008) S08003. 3.1
- 2148 [27] ATLAS Collaboration, *ATLAS inner detector: Technical Design Report, Vol. 1*. CERN,  
 2149 Geneva, 1997. <https://cds.cern.ch/record/331063>. 4

- 2150 [28] P. F. Åkesson, T. Atkinson, M. J. Costa, M. Elsing, S. Fleischmann, A. N. Gaponenko,  
2151 W. Liebig, E. Moyse, A. Salzburger, and M. Siebel, *ATLAS Tracking Event Data Model*,  
2152 Tech. Rep. ATL-SOFT-PUB-2006-004. ATL-COM-SOFT-2006-005.  
2153 CERN-ATL-COM-SOFT-2006-005, CERN, Geneva, Jul, 2006.  
2154 <https://cds.cern.ch/record/973401>. 4.1
- 2155 [29] P. Brückman, A. Hicheur, and S. J. Haywood, *Global chi2 approach to the Alignment of the*  
2156 *ATLAS Silicon Tracking Detectors*, Tech. Rep. ATL-INDET-PUB-2005-002.  
2157 ATL-COM-INDET-2005-004. CERN-ATL-INDET-PUB-2005-002, CERN, Geneva, 2005.  
2158 <https://cds.cern.ch/record/835270>. 4.1, 4.1
- 2159 [30] ATLAS Collaboration Collaboration, *Alignment of the ATLAS Inner Detector Tracking*  
2160 *System with 2010 LHC proton-proton collisions at  $\sqrt{s} = 7 \text{ TeV}$* , Tech. Rep.  
2161 ATLAS-CONF-2011-012, CERN, Geneva, Mar, 2011.  
2162 <https://cds.cern.ch/record/1334582>. 4.1, 4.2.3, 4.14
- 2163 [31] R. Härtel and S. Bethke, *Iterative local Chi2 alignment approach for the ATLAS SCT*  
2164 *detector*, Nov, 2005. <http://cds.cern.ch/record/1511044>. Presented 28 Nov 2005. 4.1
- 2165 [32] ATLAS Collaboration Collaboration, P. Brückman de Renstrom, *Alignment strategy for the*  
2166 *Inner Detector of ATLAS*, . <https://cds.cern.ch/record/1047114>. 4.1
- 2167 [33] *Alignment of the ATLAS Inner Detector and its Performance in 2012*, Tech. Rep.  
2168 ATLAS-CONF-2014-047, CERN, Geneva, Jul, 2014.  
2169 <https://cds.cern.ch/record/1741021>. 4.1, 4.2.1, 4.4
- 2170 [34] J. J. Peña, *Alignment of the ATLAS Inner Detector Upgraded for the LHC Run II*, *J. Phys.*  
2171 *Conf. Ser.* **664** (2015) no. 7, 072025. 4.1
- 2172 [35] J. Alison and I. J. Kroll, *The Road to Discovery: Detector Alignment, Electron Identification,*  
2173 *Particle Misidentification, WW Physics, and the Discovery of the Higgs Boson*, Dec, 2015.  
2174 <https://cds.cern.ch/record/1536507>. Presented 08 Nov 2012. 6
- 2175 [36] *ATLAS Inner Detector Alignment Performance with February 2015 Cosmic Rays Data*, Tech.  
2176 Rep. ATL-PHYS-PUB-2015-009, CERN, Geneva, Apr, 2015.  
2177 <https://cds.cern.ch/record/2008724>. 4.3, 4.2
- 2178 [37] ATLAS Collaboration Collaboration, M. Capeans, G. Darbo, K. Einsweiller, M. Elsing,  
2179 T. Flick, M. Garcia-Sciveres, C. Gemme, H. Pernegger, O. Rohne, and R. Vuillermet, *ATLAS*  
2180 *Insertable B-Layer Technical Design Report*, Tech. Rep. CERN-LHCC-2010-013.  
2181 ATLAS-TDR-19, Sep, 2010. <https://cds.cern.ch/record/1291633>. 4.2
- 2182 [38] *Alignment of the ATLAS Inner Detector with the initial LHC data at  $\sqrt{s} = 13 \text{ TeV}$* , Tech.  
2183 Rep. ATL-PHYS-PUB-2015-031, CERN, Geneva, Jul, 2015.  
2184 <https://cds.cern.ch/record/2038139>. 4.2
- 2185 [39] *Study of the mechanical stability of the ATLAS Insertable B-Layer*, Tech. Rep.  
2186 ATL-INDET-PUB-2015-001, CERN, Geneva, Jun, 2015.  
2187 <https://cds.cern.ch/record/2022587>. 4.2.1
- 2188 [40] *Common Framework Implementation for the Track-Based Alignment of the ATLAS Detector*,  
2189 Tech. Rep. ATL-SOFT-PUB-2014-003, CERN, Geneva, Mar, 2014.  
2190 <https://cds.cern.ch/record/1670354>. 4.2.1

- 2191 [41] ATLAS Collaboration Collaboration, *Study of alignment-related systematic effects on the*  
 2192 *ATLAS Inner Detector track reconstruction*, Tech. Rep. ATLAS-CONF-2012-141, CERN,  
 2193 Geneva, Oct, 2012. <https://cds.cern.ch/record/1483518>. 4.4, 4.4, 4.4.1.1, 4.4.1.2
- 2194 [42] S. Marti-Garcia, S. Camarda, T. Golling, M. Danninger, N. A. Styles, J. Wollrath, W. K.  
 2195 Di Clemente, S. Henkelmann, J. Jimenez Peña, O. Estrada Pastor, A. K. Morley, H. Oide,  
 2196 A. T. Vermeulen, P. Butti, E. Ricci, F. M. Follega, and R. Iuppa, *Studies of radial distortions*  
 2197 *of the ATLAS Inner Detector*, Tech. Rep. ATL-COM-INDET-2018-010, CERN, Geneva, Mar,  
 2198 2018. <https://cds.cern.ch/record/2306724>. 4.4
- 2199 [43] ATLAS Collaboration Collaboration, *Electron and photon energy calibration with the ATLAS*  
 2200 *detector using data collected in 2015 at  $\sqrt{s} = 13$  TeV*, Tech. Rep. ATL-PHYS-PUB-2016-015,  
 2201 CERN, Geneva, Aug, 2016. <https://cds.cern.ch/record/2203514>. 4.4.1
- 2202 [44] CMS Collaboration, V. Khachatryan et al., *Study of vector boson scattering and search for*  
 2203 *new physics in events with two same-sign leptons and two jets*, *Phys. Rev. Lett.* **114** (2015)  
 2204 no. 5, 051801, [arXiv:1410.6315 \[hep-ex\]](https://arxiv.org/abs/1410.6315). 5
- 2205 [45] ATLAS Collaboration Collaboration, *Observation of electroweak production of a same-sign W*  
 2206 *boson pair in association with two jets in pp collisions at  $\sqrt{s} = 13$  TeV with the ATLAS*  
 2207 *detector*, Tech. Rep. ATLAS-CONF-2018-030, CERN, Geneva, Jul, 2018.  
 2208 <https://cds.cern.ch/record/2629411>. 5, 5.8, 6.6.2
- 2209 [46] CMS Collaboration, CMS Collaboration, *Observation of electroweak production of same-sign*  
 2210 *W boson pairs in the two jet and two same-sign lepton final state in proton-proton collisions*  
 2211 *at  $\sqrt{s} = 13$  TeV*, [arXiv:1709.05822 \[hep-ex\]](https://arxiv.org/abs/1709.05822). 5
- 2212 [47] C. Bittrich, W. K. Di Clemente, et al., *Support note for measurement of electroweak*  
 2213  *$W^\pm W^\pm jj$  production at  $\sqrt{s} = 13$  TeV*, Tech. Rep. ATL-COM-PHYS-2018-252, CERN,  
 2214 Geneva, Mar, 2018. <https://cds.cern.ch/record/2309552>. 5, 5.3.3, 2, 4, 5.4.3
- 2215 [48] B. W. Lee, C. Quigg, and H. B. Thacker, *The Strength of Weak Interactions at Very*  
 2216 *High-Energies and the Higgs Boson Mass*, *Phys. Rev. Lett.* **38** (1977) 883–885. 5.0.2
- 2217 [49] S. D. Rindani, *Strong gauge boson scattering at the LHC*, in *Physics at the Large Hadron*  
 2218 *Collider*, A. Datta, B. Mukhopadhyaya, A. Raychaudhuri, A. K. Gupta, C. L. Khetrapal,  
 2219 T. Padmanabhan, and M. Vijayan, eds., pp. 145–155. 2009. [arXiv:0910.5068 \[hep-ph\]](https://arxiv.org/abs/0910.5068). 5.0.2
- 2220 [50] A. Alboteanu, W. Kilian, and J. Reuter, *Resonances and Unitarity in Weak Boson Scattering*  
 2221 *at the LHC*, *JHEP* **11** (2008) 010, [arXiv:0806.4145 \[hep-ph\]](https://arxiv.org/abs/0806.4145). 5.0.2, 5.1
- 2222 [51] J. M. Campbell and R. K. Ellis, *Higgs Constraints from Vector Boson Fusion and Scattering*,  
 2223 *JHEP* **04** (2015) 030, [arXiv:1502.02990 \[hep-ph\]](https://arxiv.org/abs/1502.02990). 5.0.2, 5.0.3
- 2224 [52] M. Szleper, *The Higgs boson and the physics of WW scattering before and after Higgs*  
 2225 *discovery*, [arXiv:1412.8367 \[hep-ph\]](https://arxiv.org/abs/1412.8367). 5.0.2
- 2226 [53] E. Accomando, A. Ballestrero, A. Belhouari, and E. Maina, *Isolating Vector Boson Scattering*  
 2227 *at the LHC: Gauge cancellations and the Equivalent Vector Boson Approximation vs complete*  
 2228 *calculations*, *Phys. Rev.* **D74** (2006) 073010, [arXiv:hep-ph/0608019 \[hep-ph\]](https://arxiv.org/abs/hep-ph/0608019). 5.0.2

- 2229 [54] P. Anger, B. Axen, et al., *Same Sign  $W^\pm W^\pm$  Production and Limits on Anomalous Quartic*  
 2230 *Gauge Couplings*, Tech. Rep. ATL-COM-PHYS-2013-990, CERN, Geneva, Jul, 2013.  
 2231 <https://cds.cern.ch/record/1561731>. Internal note for approved paper **STDM-2013-06**.  
 2232 **5.0.3, 5.1, 5.7**
- 2233 [55] J. Almond, L. Bianchini, et al., *Search for heavy neutrino,  $W_R$  and  $Z_R$  gauge bosons in events*  
 2234 *with two high- $P_T$  leptons and jets with the ATLAS detector in pp collisions at  $\sqrt{s} = 8$  TeV*,  
 2235 Tech. Rep. ATL-COM-PHYS-2013-810, CERN, Geneva, Jun, 2013.  
 2236 <https://cds.cern.ch/record/1555805>. Supporting note for EXOT-2012-24, published as  
 2237 JHEP07 (2015) 162. **5.0.4**
- 2238 [56] ATLAS Collaboration, M. Aaboud et al., *Luminosity determination in pp collisions at  $\sqrt{s} = 8$  TeV using the ATLAS detector at the LHC*, Eur. Phys. J. **C76** (2016) no. 12, 653,  
 2239 [arXiv:1608.03953 \[hep-ex\]](https://arxiv.org/abs/1608.03953). **5.1**
- 2241 [57] G. Avoni et al., *The new LUCID-2 detector for luminosity measurement and monitoring in*  
 2242 *ATLAS*, JINST **13** (2018) no. 07, P07017. **5.1**
- 2243 [58] ATLAS Collaboration, G. Aad et al., *The ATLAS Simulation Infrastructure*, Eur. Phys. J.  
 2244 **C70** (2010) 823–874, [arXiv:1005.4568 \[physics.ins-det\]](https://arxiv.org/abs/1005.4568). **5.1.1**
- 2245 [59] S. Agostinelli et al., *GEANT4 - a simulation toolkit*, Nucl. Instrum. Meth. **A506** (2003)  
 2246 **250–303**. **5.1.1**
- 2247 [60] T. Sjostrand, S. Mrenna, and P. Skands, *A Brief Introduction to PYTHIA 8.1*, Comput.  
 2248 Phys. Commun. **178** (2008) 852–867, [arXiv:0710.3820 \[hep-ph\]](https://arxiv.org/abs/0710.3820). **5.1.1**
- 2249 [61] T. Gleisberg et al., *Event generation with SHERPA 1.1*, JHEP **02** (2009) 007,  
 2250 [arXiv:0811.4622 \[hep-ph\]](https://arxiv.org/abs/0811.4622). **5.1.1**
- 2251 [62] S. Schumann and F. Krauss, *A parton shower algorithm based on Catani-Seymour dipole*  
 2252 *factorization*, JHEP **03** (2008) 038, [arXiv:0709.1027 \[hep-ph\]](https://arxiv.org/abs/0709.1027). **5.1.1**
- 2253 [63] S. Höche, F. Krauss, S. Schumann, and F. Siegert, *QCD matrix elements and truncated*  
 2254 *showers*, JHEP **05** (2009) 053, [arXiv:0903.1219 \[hep-ph\]](https://arxiv.org/abs/0903.1219). **5.1.1**
- 2255 [64] R. D. Ball et al., *Parton distributions for the LHC Run II*, JHEP **04** (2015) 040,  
 2256 [arXiv:1410.8849 \[hep-ph\]](https://arxiv.org/abs/1410.8849). **5.1.1**
- 2257 [65] S. Alioli, P. Nason, C. Oleari, and E. Re, *A general framework for implementing NLO*  
 2258 *calculations in shower Monte Carlo programs: the POWHEG BOX*, JHEP **06** (2010) 043,  
 2259 [arXiv:1002.2581 \[hep-ph\]](https://arxiv.org/abs/1002.2581). **5.1.1**
- 2260 [66] A. Ballestrero et al., *Precise predictions for same-sign  $W$ -boson scattering at the LHC*, Eur.  
 2261 Phys. J. **C78** (2018) no. 8, 671, [arXiv:1803.07943 \[hep-ph\]](https://arxiv.org/abs/1803.07943). **5.1.1**
- 2262 [67] J. Alwall, R. Frederix, S. Frixione, V. Hirschi, F. Maltoni, O. Mattelaer, H. S. Shao,  
 2263 T. Stelzer, P. Torrielli, and M. Zaro, *The automated computation of tree-level and*  
 2264 *next-to-leading order differential cross sections, and their matching to parton shower*  
 2265 *simulations*, JHEP **07** (2014) 079, [arXiv:1405.0301 \[hep-ph\]](https://arxiv.org/abs/1405.0301). **5.1.1**
- 2266 [68] H.-L. Lai, M. Guzzi, J. Huston, Z. Li, P. M. Nadolsky, J. Pumplin, and C. P. Yuan, *New*  
 2267 *parton distributions for collider physics*, Phys. Rev. D **82** (2010) 074024, [arXiv:1007.2241](https://arxiv.org/abs/1007.2241)  
 2268 [\[hep-ph\]](https://arxiv.org/abs/hep-ph). **5.1.1**

- 2269 [69] T. Sjostrand, S. Mrenna, and P. Skands, *PYTHIA 6.4 physics and manual*, JHEP **05** (2006)  
 2270 026, [arXiv:0603175 \[hep-ph\]](https://arxiv.org/abs/0603175). 5.1.1
- 2271 [70] ATLAS Collaboration, G. Aad et al., *Muon reconstruction performance of the ATLAS*  
 2272 *detector in protonproton collision data at  $\sqrt{s} = 13$  TeV*, Eur. Phys. J. **C76** (2016) no. 5, 292,  
 2273 [arXiv:1603.05598 \[hep-ex\]](https://arxiv.org/abs/1603.05598). 5.2.1.1, 12
- 2274 [71] ATLAS Collaboration Collaboration, *Electron efficiency measurements with the ATLAS*  
 2275 *detector using the 2015 LHC proton-proton collision data*, Tech. Rep.  
 2276 ATLAS-CONF-2016-024, CERN, Geneva, Jun, 2016.  
 2277 <https://cds.cern.ch/record/2157687>. 5.2.1.2
- 2278 [72] M. Cacciari, G. P. Salam, G. Soyez, *The anti- $k_t$  jet clustering algorithm*, JHEP **04** (2008) 063,  
 2279 [arXiv:0802.1189 \[hep-ph\]](https://arxiv.org/abs/0802.1189). 5.2.1.3, 6.4.1
- 2280 [73] ATLAS Collaboration, M. Aaboud et al., *Jet energy scale measurements and their systematic*  
 2281 *uncertainties in proton-proton collisions at  $\sqrt{s} = 13$  TeV with the ATLAS detector*, Phys.  
 2282 Rev. **D96** (2017) no. 7, 072002, [arXiv:1703.09665 \[hep-ex\]](https://arxiv.org/abs/1703.09665). 5.2.1.3
- 2283 [74] *Tagging and suppression of pileup jets with the ATLAS detector*, Tech. Rep.  
 2284 ATLAS-CONF-2014-018, CERN, Geneva, May, 2014.  
 2285 [http://cds.cern.ch/record/1700870](https://cds.cern.ch/record/1700870). 5.2.1.3
- 2286 [75] D. Adams, C. Anastopoulos, et al., *Recommendations of the Physics Objects and Analysis*  
 2287 *Harmonisation Study Groups 2014*, Tech. Rep. ATL-PHYS-INT-2014-018, CERN, Geneva,  
 2288 Jul, 2014. <https://cds.cern.ch/record/1743654>. 5.2.1.4
- 2289 [76] ATLAS Collaboration, M. Aaboud et al., *Measurement of the cross-section for producing a W*  
 2290 *boson in association with a single top quark in pp collisions at  $\sqrt{s} = 13$  TeV with ATLAS*,  
 2291 JHEP **01** (2018) 063, [arXiv:1612.07231 \[hep-ex\]](https://arxiv.org/abs/1612.07231). 5.2.1.4
- 2292 [77] ATLAS Collaboration, M. Aaboud et al., *Performance of missing transverse momentum*  
 2293 *reconstruction with the ATLAS detector using proton-proton collisions at  $\sqrt{s} = 13$  TeV*, Eur.  
 2294 Phys. J. **C78** (2018) no. 11, 903, [arXiv:1802.08168 \[hep-ex\]](https://arxiv.org/abs/1802.08168). 5.2.2
- 2295 [78] ATLAS Collaboration, M. Aaboud et al., *Measurements of b-jet tagging efficiency with the*  
 2296 *ATLAS detector using  $t\bar{t}$  events at  $\sqrt{s} = 13$  TeV*, JHEP **08** (2018) 089, [arXiv:1805.01845](https://arxiv.org/abs/1805.01845)  
 2297 [\[hep-ex\]](https://arxiv.org/abs/1805.01845). 5.2.2
- 2298 [79] J.-F. Arguin, J. Claude, G. Gonella, B. P. Kersevan, K. Koneke, K. Lohwasser, K. Mochizuki,  
 2299 M. Muskinja, C. Piaulet, and P. Sommer, *Support Note for Electron ID: charge*  
 2300 *mis-identification*, Tech. Rep. ATL-COM-PHYS-2017-1014, CERN, Geneva, Jul, 2017.  
 2301 <https://cds.cern.ch/record/2273365>. 5.3.3
- 2302 [80] C.-H. Kom and W. J. Stirling, *Charge asymmetry in W + jets production at the LHC*, Eur.  
 2303 Phys. J. **C69** (2010) 67–73, [arXiv:1004.3404 \[hep-ph\]](https://arxiv.org/abs/1004.3404). 5.4
- 2304 [81] R. Steerenberg, *LHC Report: Another run is over and LS2 has just begun...*,  
 2305 [https://home.cern/news/news/accelerators/](https://home.cern/news/news/accelerators/lhc-report-another-run-over-and-ls2-has-just-begun)  
 2306 [lhc-report-another-run-over-and-ls2-has-just-begun](https://home.cern/news/news/accelerators/lhc-report-another-run-over-and-ls2-has-just-begun), 2018. Accessed: 2018-12-14. 6
- 2307 [82] *Letter of Intent for the Phase-I Upgrade of the ATLAS Experiment*, Tech. Rep.  
 2308 CERN-LHCC-2011-012. LHCC-I-020, CERN, Geneva, Nov, 2011.  
 2309 [http://cds.cern.ch/record/1402470](https://cds.cern.ch/record/1402470). 6

- 2310 [83] G. Apollinari, I. Bjar Alonso, O. Brning, M. Lamont, and L. Rossi, *High-Luminosity Large*  
2311 *Hadron Collider (HL-LHC): Preliminary Design Report*. CERN Yellow Reports: Monographs.  
2312 CERN, Geneva, 2015. <https://cds.cern.ch/record/2116337>. 6
- 2313 [84] ATLAS Collaboration Collaboration, ATLAS Collaboration, *ATLAS Phase-II Upgrade*  
2314 *Scoping Document*, Cern-lhcc-2015-020, Geneva, Sep, 2015.  
2315 <http://cds.cern.ch/record/2055248>. 6
- 2316 [85] D. Espriu and B. Yencho, *Longitudinal WW scattering in light of the “Higgs boson”*  
2317 *discovery*, Phys. Rev. D **87** (2013) 055017, arXiv:1212.4158 [hep-ph]. 6, 6.1
- 2318 [86] ATLAS Collaboration Collaboration, *Prospects for the measurement of the  $W^\pm W^\pm$  scattering*  
2319 *cross section and extraction of the longitudinal scattering component in pp collisions at the*  
2320 *High-Luminosity LHC with the ATLAS experiment*, Tech. Rep. ATL-PHYS-PUB-2018-052,  
2321 CERN, Geneva, Dec, 2018. <http://cds.cern.ch/record/2652447>. 6
- 2322 [87] ATLAS Collaboration Collaboration, *Studies on the impact of an extended Inner Detector*  
2323 *tracker and a forward muon tagger on  $W^\pm W^\pm$  scattering in pp collisions at the*  
2324 *High-Luminosity LHC with the ATLAS experiment*, Tech. Rep. ATL-PHYS-PUB-2017-023,  
2325 CERN, Geneva, Dec, 2017. <https://cds.cern.ch/record/2298958>. 6
- 2326 [88] T. Sjöstrand, S. Ask, J. R. Christiansen, R. Corke, N. Desai, P. Ilten, S. Mrenna, S. Prestel,  
2327 C. O. Rasmussen, and P. Z. Skands, *An Introduction to PYTHIA 8.2*, Comput. Phys.  
2328 Commun. **191** (2015) 159–177, arXiv:1410.3012 [hep-ph]. 6.2
- 2329 [89] ATLAS Collaboration Collaboration, *Expected performance for an upgraded ATLAS detector*  
2330 *at High-Luminosity LHC*, Tech. Rep. ATL-PHYS-PUB-2016-026, CERN, Geneva, Oct, 2016.  
2331 <http://cds.cern.ch/record/2223839>. 6.3
- 2332 [90] P. C. Bhat, H. B. Prosper, S. Sekmen, and C. Stewart, *Optimizing Event Selection with the*  
2333 *Random Grid Search*, Comput. Phys. Commun. **228** (2018) 245–257, arXiv:1706.09907  
2334 [hep-ph]. 6.5.1
- 2335 [91] G. Cowan, K. Cranmer, E. Gross, and O. Vitells, *Asymptotic formulae for likelihood-based*  
2336 *tests of new physics*, Eur. Phys. J. **C71** (2011) 1554, arXiv:1007.1727 [physics.data-an].  
2337 [Erratum: Eur. Phys. J.C73,2501(2013)]. 6.5.1